Andreou, Eleni (2019) *LiBH4 as candidate solid state electrolyte in Li-ion batteries*. MRes thesis.

https://theses.gla.ac.uk/41088/

$LiBH_4$ as candidate solid state electrolyte in Li-ion batteries.

Eleni Andreou

Submitted in fulfilment of the requirements for the
Degree of Master of Science by Research

School of Chemistry
College of Science & Engineering
University of Glasgow

October 2018

Abstract

Electrical Energy Storage (EES) systems aspire to store the power network's energy and provide it back when necessary, eliminating the discrepancies between demand and supply.

During the last decade, lithium-ion batteries have been established as an important pillar in humanity's effort, not only to produce "cleaner power" but, also, to develop a safe, environmentally friendly and low-cost set of methods and technologies for storing the produced power. They are -by far- the most common medium for storing energy, at a small scale (e.g. portable electronics), as one of their numerous advantages is the fact that they can be used in conjunction with many different installations of the existing grid's infrastructure.

Focusing, mainly, on the mechanisms that apply in the solid-state, Li-ion conduction in Li-ion batteries takes place due to the defects existing in their crystalline solid components. Today, concerns that relate to safety, cost, charge/discharge rates, cycle life and energy density of Li-ion batteries have risen questions which need to be answered.

During the last two decades, high-end research has been conducted aiming to address the challenges and limitations of lithium metal batteries (LMBs) presented previously. The ongoing efforts focus on the suppression of lithium dendritic growth, either through the use of solid electrolytes that act as mechanical barriers, or through development of electrolytes which produce a suitable passivation layer, widely known as the "*solid-electrolyte interphase*" (SEI). Nowadays, safety concerns have led to the extensive use of lithium-ion batteries (LIBs), rather than LMBs, as no entirely successful strategy has been developed to suspend the growth of dendrites.

Complex hydrides are among the most promising candidate materials for use as solid-state electrolytes. As the demand for energy storage systems that are

compact, lightweight, and powerful continues to grow, mainly due to the worldwide proliferation of portable electronic devices.

Sodium, lithium and boron are the lightest elements that can form solid-state compounds with hydrogen, such as $LiBH_4$.

Researchers' interest into the properties of lithium borohydride ($LiBH_4$) first arose due to indications that it could function as a promising hydrogen storage material.

Following its extensive study as a hydrogen storage material, $LiBH_4$ has drawn interest as a potential electrolyte for solid-state batteries. This was proposed by the discovery that $LiBH_4$ undergoes a structural transition from its orthorhombic, low temperature (LT-) phase to a hexagonal, high temperature (HT-) phase at 380 *K*. Following the stabilisation of the HT-phase at room temperature (RT), attempts have been made to synthesise sodium-substituted lithium borohydride but, previous work has suggested that a direct reaction between $LiBH_4$ and $NaBH_4$ is not possible.

This project had been focused on the stabilisation of the high pressure (HP-) phase of $LiBH_4$ at RT. Our efforts have been successful in the investigation of the most simple and efficient way to synthesise, stabilise and characterise the ion conducting, HP-phase of $LiBH_4$.

Table of contents

List of Tables

List of Figures

Acknowledgement

I would like to thank my supervisor, Professor Duncan H. Gregory for giving me the chance to conduct my MRes project as a member of his research group at the University of Glasgow.

I would, also, like to thank Davide, Hal and Simon for all their support and help during the last year but, most importantly, for their friendship.

Many thanks to everyone in the Gregory Group for working with and by me when needed.

Abbreviations

AP	Ambient Pressure
EC	Ethylene Carbonate
ECP	Electro-Chemical Potential
EES	Electrical Energy Storage
EIS	Electrochemical Impedance Spectroscopy
EMF	Electro-Motive Force
ESW	Electrochemical Stability Window
EV	Electric Vehicles
GPE	Gel-Polymer Electrolyte
HEV	Hybrid Electric Vehicles
HOMO	Highest Occupied Molecular Orbital
HP	High Pressure (phase)
HT	High Temperature (phase)
LIB	Li-ion Battery
LISICON	Lithium (Li) Super Ionic Conductor
LMB	Lithium-Metal Batteries
LUMO	Lowest Unoccupied Molecular Orbital
LP	Low Pressure (phase)
LT	Low Temperature (phase)
MCP	Mechano-Chemical Processing
NASICON	Sodium (Na) Super Ionic Conductor
PXD	Powder X-ray Diffraction
PND	Powder Neutron Diffraction
PHEV	Plug-in Hybrid Electric Vehicles
RLB	Rechargeable Lithium Batteries
RT	Room Temperature
SDR	Self-Discharge Rate
SEI	Solid Electrolyte Interphase
SEM	Scanning Electron Microscopy

SOC	State-Of-Charge
SPE	Solid-Polymer Electrolyte
SSB	Solid-State Batteries
SSE	Solid-State Electrolyte

Declaration

The work presented in this thesis is the original work of the author except where specific reference is made to other sources. It has not been submitted, in whole or in part, for any other degree at this or any other institution.

Eleni Andreou
Date: October 2018

1. Context & Background

“The storage battery is, in my opinion, a catchpenny, a sensation, a mechanism for swindling the public by stock companies. The storage battery is one of those peculiar things which appeals to the imagination, and no more perfect thing could be desired by stock swindlers than that very self-same thing. ... Just as soon as a man gets working on the secondary battery it brings out his latent capacity for lying.” [1].

That is what Thomas Edison wrote in 1883 regarding the “storage battery”, following his unsuccessful try in 1879 to “…devise a system of placing storage batteries in houses connected to mains and charging them in the day time, to be discharged in the evening and night to run incandescent lamps” [1].

Almost one century later, in 1980, John Goodenough would shake down Edison’s thoughts by giving birth to the cobalt-oxide cathode. Only eleven years after this vital invention, Sony will massively produce the first lithium-ion battery and the world will enter the era of portable devices.

Nowadays, Electrical Energy Storage (EES) systems aspire to properly store the power network’s energy and provide it back when necessary, eliminating the discrepancies between demand and supply.

During the last decade, lithium-ion batteries have been established as an important pillar in humanity’s effort to, not only produce “cleaner power” but, also, develop a safe, environmentally friendly and low-cost set of methods and technologies for storing the produced power.

Lithium ion cells are competing with Ni-Cd and Ni-MH cells in terms of applications. The Li-ion cells are currently available in cylindrical, prismatic and flat plate formats [2].

Between 1991 and 2006, the manufacture and sales of Li-ion batteries were doubled. It is interesting to note that the cost of an equivalent size cell in 1995 ($8) sold for half the price ($4) in 2006 [2]. In the meantime, the energy density of the cell had doubled! It is reasonable to assume that the LIB market will grow significantly again in the very near future, as new technologies are discovered and improved.

Currently, the Li-ion battery (LIB) market is mostly driven by cellular telephones and notebook computer applications, with predictions for significant expansion in the near future as consumers ask for higher performance devices [2].

On the other hand, the Ni–Cd battery dominates the power tool market, while the lead-acid battery is the one indisputable dominant system when it comes to the market of constant power sources.

Tesla’s first commercial electric vehicle in 2007 set the scene for the transition from traditional ways of transport to electric propulsion [3]. The automobile and aerospace power markets are expected to absorb the majority of the future developments in LIB technologies.

Plug-in hybrid electric vehicles (PHEVs) are a new and upcoming technology in the transportation and power sector. These vehicles can run on fossil fuels, electricity or a combination of the two, presenting a variety of advantages such as, reduction of fossil fuel use, increase of fuel economy, increased power efficiency, lowered greenhouse gas (GHG) emissions and vehicle-to-grid (V2G) technology [4]-[6].

Various economic models, economic incentives, loading profiles, and charging profiles have been developed for these new vehicles, but knowledge is limited regarding the impact of PHEVs on the distribution grid. As promising PHEVs may be, the need of up-to-date and efficient infrastructure should not be ignored. Thus, it is important to study in depth the effects that will have on both electricity distribution and generation [7].

1.1 Electrical Energy Storage Systems

It is widely accepted that most current human activities -mostly related to production- and energy use add up to seriously threaten the environment, causing major problems in relation to greenhouse gases and climate change [8].

Considering that the total primary energy supply, in the world and in *Organisation for Economic Co-operation and Development* (OECD) nations (in megatons oil equivalent, Mtoe), was, respectively, 6043 and 3742 Mtoe in 1973, and 9491 and 5096 Mtoe in 1998, the conclusions presented below can be deduced [8]:

1) A total increase by 57% of the world's total energy supply has taken place in only 25 years,
2) Even though the production of oil follows increasing rates all around the world, oil's significantly smaller share of the total energy supply has, nowadays, resulted in a fairly modest expansion in industrial activity,
3) Coal is, primarily and almost solely, used for electricity generation (20.5 Mtoe *vs* 10.9 Mtoe for nuclear),
4) New fields have been discovered and opened up, due to the rising rates of natural gas production (20.6 Mtoe *vs*. 20.5 Mtoe for coal),
5) Renewable energy forms contribute modestly in energy generation processes.

In order to move towards a "greener" direction, many countries worldwide emphasise more -or even totally- sustainable ways of electrical production, therefore, energy storage and power management are increasingly gaining ground in the planning of countries' environmental policies. Due to the non-continuous energy supply, which emerges as one major problem of such generating technologies, only a serious turn to energy storage systems can overcome the obstacles in the way of releasing renewably generated electrical energy. Referring to both on- and off-grid applications, energy-storage technologies can easily play their role and lead to a future clean-energy landscape, by ensuring secure and continuous supply to the consumers, through distributed routes of energy supply [9].

Electrical energy has been considered for many decades now to be a ubiquitous, low-cost commodity. It makes up 12% of the world's total energy [10] and this number is expected to increase significantly the next few years to 34% by 2025. To delocalise electricity production and introduce alternative, renewable sources raises the difficulty of the power network's stabilisation, mainly due to demand and supply discrepancies. It is, therefore, necessary to generate the energy, transmit it, convert it and then store it according to demand. [11]

Electrical energy storage (EES) systems can be distinguished in terms of their function or form. Based on their function, systems can be separated into those which focus on energy management and those which play a significant role in the improvement of power quality and reliability. Low-power applications (feeding of transducers and emergency terminals) and medium-power applications (individual electrical systems, town supply) fall into the first category while, network connection applications with peak levelling and power-quality control systems fall into the second category [11]. A technical comparison of the different types of EES systems is given in Figure 1.1.

In terms of their function, on the other hand, four different types of energy storage systems are accepted: electrical, mechanical, chemical and thermal. The three most common energy storage systems are: *batteries*, which store energy within the electrode structure and are re-chargeable, *fuel cells*, which store and convert energy in the reactants and are not re-chargeable and, *super-capacitors*, which present the ability of storing energy through a different capacitive process at the electrode-electrolyte interface [12]. Electrochemical energy storage systems, a sub-category of chemical energy storage systems, have the ability to convert chemical energy directly into electrical energy through redox reactions.

1.2 Solid-State Batteries

Batteries are the most common medium for storing energy as one of their numerous advantages is the fact that they can be used in conjunction with many different installations of the existing grid's infrastructure.

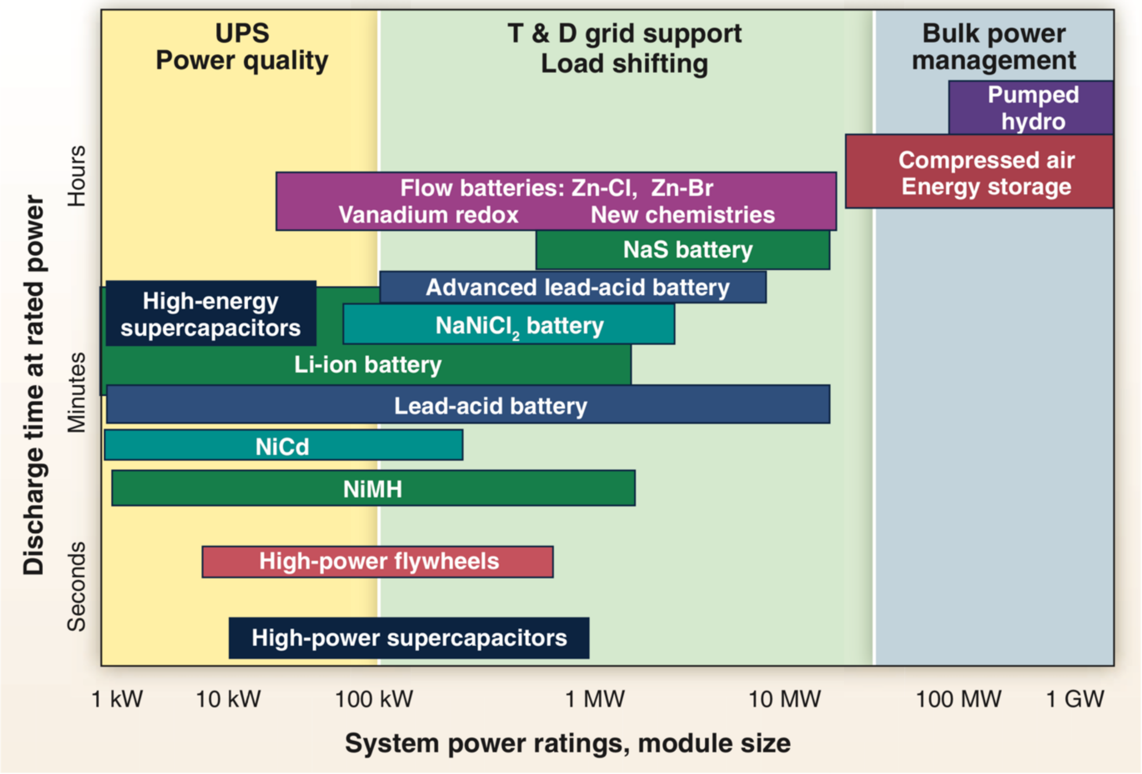

Figure 1. 1: Technical comparison of various EES systems [12].

Over the last decade, research has significantly focused on the effort to develop all-solid- state, rechargeable, Li-ion batteries. As for any type of battery, solid-state batteries consist of one or more galvanic cells, connected in series or parallel. Each cell is composed of an *anode*, containing lithium, a *cathode*, where the electrons migrate through battery's external electrical circuit on discharge (with the exact opposite behaviour during charging) and, the *electrolyte*, the means of ion flow between the two electrodes, while blocking any flow of electrons (*Figure 1.2*).

In principle, the Li-ion conduction mechanisms in solid-state Li-ion batteries take place due to the defects existing in their solid electrolytes. When these defects, which can be vacancies or interstitial ions, "move" around the extended structure of the solid they render it ionically conductive [13].

Concerns with the safety, cost, charge/discharge rates, cycle life and energy density of Li-ion batteries represent the main challenges in Li-ion development.

Additionally, if Li-ion batteries are to be employed in Hybrid Electrical Vehicles (HEVs) then gravimetric energy density, uniformity in performance of individual cells inside a complex, multicell battery and cost are the fields where more research is absolutely necessary [14].

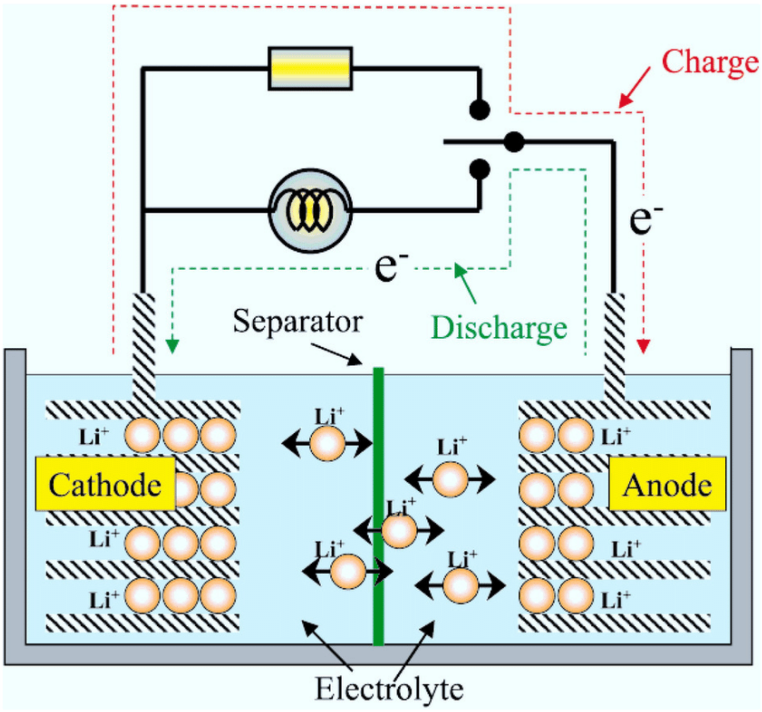

Figure 1. 2: Schematic of the operation of a common Li-ion battery.

1.2.1 Principles of a Battery

Setting the beginning of batteries' history at the invention of Alessandro Volta cell in 1800, the history of battery moves towards the commercialization of the first Li-ion battery in 1992 and continues until this day with a bright future just across the road. Referring to any known cell system, from the *Leclanché cell* [1] to lead-acid battery, nickel-cadmium accumulator and a variety of other systems, electrochemical cells can be classified into two general categories [15]:

---

[1] The *Leclanché cell* is a battery invented by the French scientist Georges Leclanché in 1866. The battery contained an ammonium chloride electrolyte, a carbon cathode, a manganese dioxide depolariser and a zinc anode.

- *Primary cells* irreversibly transform chemical to electrical energy, until the available supply of reactants is exhausted.
- *Secondary cells*, on the other hand, can reverse the chemical reactions taking place in them by supplying electrical energy to the cell and restoring their original composition.

Research is still being carried out regarding the maximum performance and reliability of the *Leclanché cell*. As presented in the "Rubik's cube" (*Figure 1.3*), a reliable battery classification can be completed by considering the nature (liquid, soft or solid) of the three main components of the device: the anode, the electrolyte, and the cathode **[16]**. The components' nature is crucial as it affects the formed interphases, some of which are difficult to handle. Usually batteries have a solid–liquid–solid configuration; the liquid– solid–liquid system corresponds to the Na-S battery using *β*-alumina as the electrolyte, which also permits relatively easy manufacture. Conversely, the all-solid system involves difficult interface problems **[17]**.

With regard to efficient battery operation, several important parameters have to be considered for a battery to function effectively, including: the gravimetric energy density ($Wh\cdot g^{-1}$), the volumetric capacity ($Ah\cdot cm^{-3}$), the rate capability, the life cycle and the self-discharge rates. These properties are fixed by the electrochemical characteristics of the active elements (positive and negative electrodes). Here it is important and useful to note that, in rechargeable batteries, the "cathode" and "anode" terms are not entirely appropriate -in terms of electrochemistry- as the positive electrode is the cathode on discharge but becomes the anode on charge, and so forth. The definitions apply to discharge in practice.

To conclude, the most essential condition in the process of selecting materials for use in batteries, is their ability to present redox properties, i.e., reduction-oxidation reactions **[17]**.

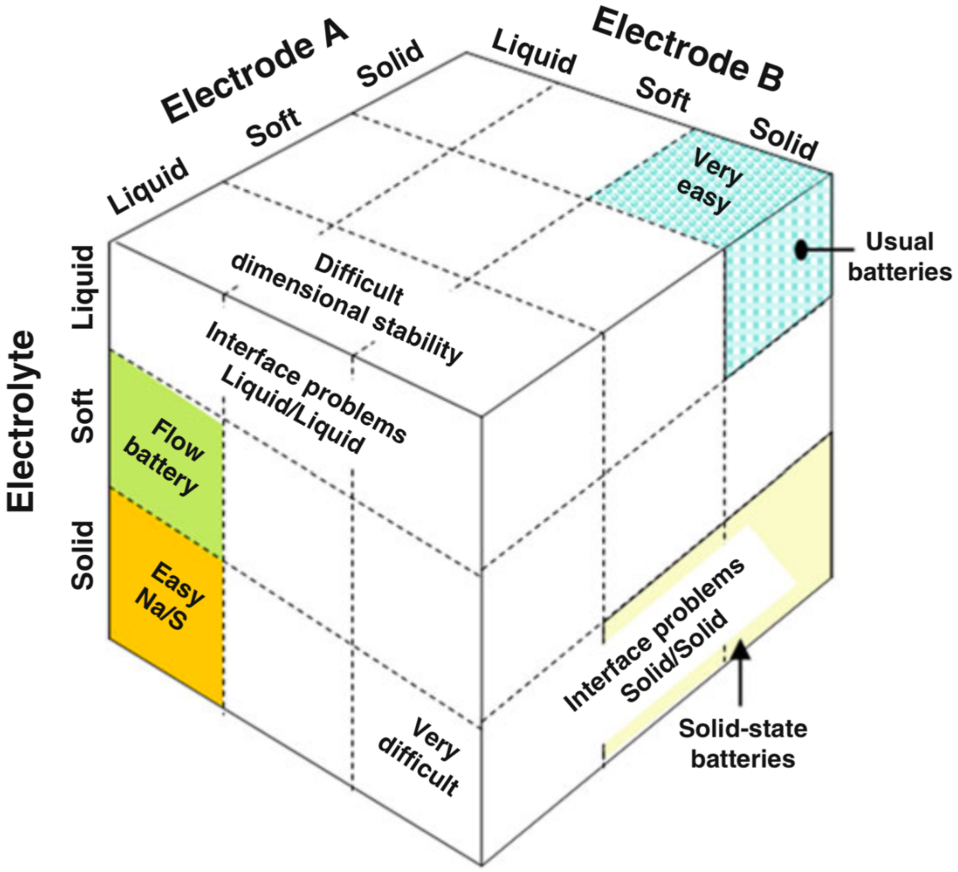

Figure 1. 3: Rubik's cube showing the association of the three components in the solid, soft and liquid state of electrochemical cells [16].

1.2.1.1 Principal Parameters for Efficient Battery Design

The electrochemical potential (ECP), is a thermodynamic measure that combines the concepts of energy stored in the form of chemical potential and electrostatics. In both solid-state physics and electrochemistry, it is usual to discuss the chemical and electrochemical potential of an electron. In an electrochemical cell, the chemical reactions that take place around electrodes are expressed by the equations [18]:

$$aA - ne \rightleftharpoons bB \qquad [1.1]$$

$$cC + ne \rightleftharpoons dD \qquad [1.2]$$

$$\boldsymbol{aA + cC \rightleftharpoons bB + dD} \qquad [1.3]$$

where, a molecules of A gives up n electrons e to form b molecules of B at one electrode, while C takes up n electrons e to form d molecules of D at the other. Equations 1.1 and 1.2 represent the reduction and oxidation reactions, respectively, while Equation 1.3 is the overall reaction in the cell, as the sum of the two "half-cell" reactions. The change in the standard free energy, ΔG^0, of this reaction is:

$$\boldsymbol{\Delta G^0 = -nFE^0} \qquad [1.4]$$

where, F is the Faraday constant ($F = eN_A = 96485\ C{\cdot}\mathrm{mol}^{-1}$) and E^0 is the standard electromotive force (EMF). When under conditions other than the standard state, the potential V_{cell} of the cell is given by the Nernst equation:

$$\boldsymbol{V_{cell} = E^0 - \frac{RT}{nF} ln \frac{\mu_B^i \mu_D^i}{\mu_A^i \mu_C^i}} \qquad [1.5]$$

where, μ_i is the activity of relevant species, R is the gas constant ($8.314\ JK^{-1}{\cdot}\mathrm{mol}^{-1}$), and T is the absolute temperature.

In the case of two electrodes with a semiconducting character, the operating voltage of a cell is limited by the open-circuit voltage, $\boldsymbol{V_{oc}}$, which is the potential difference across terminals of the battery when no current is being drawn:

$$\boldsymbol{V_{OC} = -\frac{1}{nF}(\mu_A^i - \mu_C^i)} \qquad [1.6]$$

where, $(\mu_A^i - \mu_C^i)$ is the difference in the chemical potential of the anode (A) and the cathode (C), and n is the number of electronic charges involved in the chemical reaction of the cell. The nominal voltage is determined by the energies involved in both electronic and ionic transfer. The energy for electron transfer is determined by the work function, while the energy for ion transfer by the crystallographic structure. Therefore, both the electronic band structure and the barrier height for ion motion should be considered. The magnitude of the open-circuit voltage is constrained, not only by the $(\mu_A^i - \mu_C^i)$ difference of the electrochemical potentials of the anode reductant and the cathode oxidant, but also by either the energy gap E_g between the HOMO (highest occupied molecular orbital) and the LUMO (lowest unoccupied molecular orbital) of a liquid electrolyte, or by the energy gap E_g between the top of the valence band and the bottom of the conduction band of a solid electrolyte [14].

The *energy density* is a common measure in evaluating battery systems. The specific energy stored (in *Wh·kg*$^{-1}$) in a battery is measured by discharging a battery at a specific current:

$$\boldsymbol{E_{cell} = V_{cell} Q_{dis}} \qquad [1.7]$$

where, V_{cell} is the operating potential in volts (*V*), obtained from the energy change for the cell reaction and Q_{dis} is the specific capacity (*Ah*·kg^{-1} or *mAhg*$^{-1}$). Its theoretical value is obtained from Faraday's law:

$$\boldsymbol{Q_{dis} = \frac{1000 \times nF}{3600 \times M_w} = \frac{26.8}{M_w} \times n} \qquad [1.8]$$

where, M_w is the molecular mass of the "limiting" electrode material and n is the number of electronic charges involved in the chemical reaction of the cell.

For example, if one considers lithium insertion into the vanadium oxide (V_6O_{13}) lattice (M_w = 542 g·mol^{-1}) that can reversibly accommodate 4 Li ions (Li^+) per formula unit, at an experimental potential of 2.4 *V* vs. Li^0/Li^+ at $C/_3$ rate (see below) according to the reaction [17]:

$$\boldsymbol{4Li^+ + 4e^- + V_6O_{13} \rightleftharpoons Li_4V_6O_{13}} \qquad [1.9]$$

Then by applying Equations 1.7 and 1.8, the theoretical specific capacity is 197.8 *mAhg*$^{-1}$ and the theoretical energy density 475 *Wh·kg*$^{-1}$.

The theoretical energy of the battery is calculated by Equation 1.10:

$$\boldsymbol{E_{batt} = \left(\frac{1}{Q^+} - \frac{1}{Q^-}\right)^{-1}} \qquad [1.10]$$

where, Q^+ and Q^- express the capacities of the active materials of the positive and negative electrode in the battery, respectively.

The C -rate is a measure of the rate at which a battery is discharged relative to its maximum capacity [17]. A charge at nC rate means a full charge in a time of $^1/_n$ hours [19].

The *power output* (P_{out} in *W*) of a battery is the product of the electric current (I_{dis} in *A*) delivered by the discharging battery and the voltage (V_{dis} in *V*) across the negative and positive external contacts:

$$\boldsymbol{P_{out} = I_{dis}V_{dis}} \tag{1.11}$$

The voltage ($\mathrm{V_{dis}}$) is reduced from its open-circuit value $\mathrm{V_{oc}}$ ($\mathrm{I_{dis}} = 0$) by the voltage drop ($\mathrm{I_{dis}R_b}$) due to the internal resistance $\mathrm{R_b}$ of the battery and the polarisation losses that occur at each electrode and result in a decreased cell potential during discharge ($\mathrm{V_{dis}}$) and an increased cell potential on charge ($\mathrm{V_{ch}}$) that are expressed by [17]:

$$\boldsymbol{V_{dis} = V_{oc} - I_{dis}R_b} \tag{1.12}$$

$$\boldsymbol{V_{ch} = V_{oc} + I_{ch}R_b} \tag{1.13}$$

which have the form of Ohm’s law. Additionally, the *Joule heating effect* of the I^2R_b losses in the internal resistance of the cell will raise the temperature. Thus, a low internal battery resistance, as well as the highest V_{oc} possible, are required in order for high values of maximum power (P_{max}) to be achieved:

$$\boldsymbol{P_{max} = I_{max}V_{max}} \tag{1.14}$$

$$\boldsymbol{R_b = R_{el} + R_{in}(A) + R_{in}(C) + R_c(A) + R_c(C)} \tag{1.15}$$

where $R_{in}(A)$, $R_{in}(C)$ are the transport resistances of the working ion across the electrolyte-electrode interface, while $R_c(A)$ and $R_c(C)$ represent the intrinsic resistance of electrodes. The electrolyte resistance R_{el} to the ionic current is proportional to the $^L/_A$ ratio of the effective thickness (*L*) and the geometrical area (A) of the inter-electrode space, filled with an electrolyte which presents an ionic conductivity (σ_i), expressed by Equation 1.16 below:

$$\boldsymbol{R_{el}} = \frac{\boldsymbol{L}}{\boldsymbol{A\sigma_i}} \qquad [1.16]$$

It is important to note that the active ion’s transport resistance across the electrolyte-electrode interfaces is proportional to the ratio of the geometrical and interfacial areas at each electrode:

$$\boldsymbol{R_{in}} \sim \boldsymbol{A/A_{in}} \qquad [1.17]$$

Since the chemical reaction of the cell involves ionic transport across an interface, achievement and retention of a large particle-electrolyte interface area over many discharge-charge cycles is important and vital for high electrode capacity, which is one of the biggest challenges the battery system design has to deal with. Failure to guarantee a reversible reaction can lead to the particles’ possible fracture or loss of contact with one another upon cycling, resulting in a non-continuous, electronic pathway towards the current collector.

When the battery discharge voltage (V_{dis}) is plotted against the discharge current ($\boldsymbol{I_{dis}}$), which is delivered across a load, it leads to a *polarisation curve*. The voltage drop ($V_{oc} - V$) -which equals to $\eta(I)$, *a voltage that exceeds the maximum value of operating voltage in an electric circuit-* (*Figure 1.4*) provides a measure of the battery resistance:

$$\boldsymbol{R_b(I) = \eta(I)/I} \qquad [1.18]$$

During discharge, $\eta(I_{dis}) = (V_{dis} - V_{oc})$ corresponds to *over-voltage*. The interfacial voltage drop saturates at the boundary of region *I* and region *II* of the polarisation curve (*Figure 1.4*); therefore, in region *II*, the curve’s slope is:

$$\boldsymbol{dV/dI \approx R_{el} + R_c(A) + R_c(C)} \qquad [1.19]$$

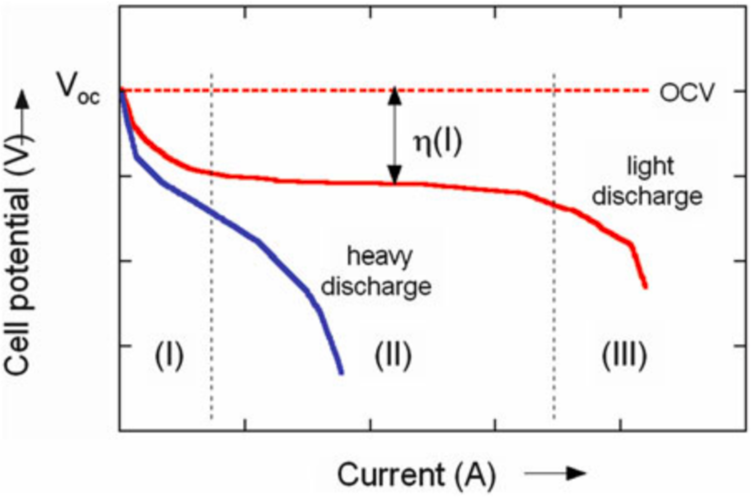

Figure 1. 4: Typical polarisation curve for a battery's voltage (V) against the current (I) delivered across a load [17].

The behaviour in region *III* depends on diffusion. Information regarding the ionic transport is provided by a *discharge curve*, which represents either the battery's voltage (*V*) against the state of charge (see below), or the time during which a constant current (*I*) has been delivered.

The state-of-charge (SOC) of the battery, (expressed in %) is the fraction of the available charge capacity over the total capacity of the battery (*Equation 1.20*):

$$\boldsymbol{SOC = 100\% \times \frac{Q_e}{Q_0}} \qquad [1.20]$$

where, Q_e is the battery's charge and Q_0 the nominal battery capacity (in *Ah*). The SOC value of a battery is an important parameter as it expresses the remaining available energy before the next charge, maybe the most important information for the battery's user. Determining the SOC of a battery is a very challenging job, that requires battery modelling and is not studied further in this work [20][21].

Last but not least, among the key parameters that govern an efficient battery system design, is the *self-discharge rate* (SDR). *SDR represents the percentage of capacity that a battery loses in open-circuit conditions* [17]. Most commonly, the SDR is derived from the ratio of the lost discharge capacity, after 2 days of storage and under normal conditions, to the maximum cell capacity as:

$$\boldsymbol{SDR}(\%) = \frac{Q_{max} - Q_{ret}}{Q_{max}} \times \mathbf{100\%} \qquad [1.21]$$

where, Q_{max} is the maximum discharge capacity at a discharge current density $C/_{n}$ and Q_{ret} the retained capacity at a discharge $C/_{n}$ rate.

1.2.2 Li-ion Solid-State Batteries

In the 1960s, a new generation of electrochemical devices able to store and generate energy was invented, just after the incorporation of a very pure lithium-metal foil as anode element into a lithium-salt, non-aqueous solution as electrolyte. The charge transport (Li^+) inside these novel electrochemical generators is created by the simple reaction below (*Equation 1.22*) at the anode:

$$\boldsymbol{Li} \longrightarrow \boldsymbol{Li}^{+} + \boldsymbol{e}^{-} \qquad [1.22]$$

This way, one electron is released through the external circuit and one ion is introduced through the electrolyte into the porous structure of the cathode. Lithium technology is a really attractive one because of the fact that Li is a particularly light metal (M_w = 6.941 g·mol^{-1} and ρ = 0.51 g·cm^{-3}), with an electronic configuration of $(He)2s^1$. Li metal has a theoretical capacity of 3860 m*Ah*·*g*$^{-1}$ and the couple Li^+ has the highest electroactivity with a standard redox potential equal to -3.04 *V* against H_2/H^+. As can be predicted, the voltage of lithium batteries is also significantly higher than that of the Pb-acid and Ni-metal hydride battery systems, as lithium presents high electropositivity. Primary and secondary lithium batteries using a non-aqueous electrolyte come with cell potential higher than 1.23 *V* (the thermodynamic limitation of water at 25 ^0C) and, thus, exhibit much higher energy densities than aqueous electrolyte-based batteries.

Due to its high reactivity with air, nitrogen and water, lithium does not exist as a pure metal in nature. It is extracted from ore or brine salt marsh (lithium chloride (LiCl), lithium hydroxide (LiOH), lithium carbonate (Li_2CO_3)). 0.8 *kg* of lithium metal is produced every second in the world and a total of 25000 tons a year is mainly used for the production of lithium-ion batteries for electric cars or cell phones. According to the US Geological survey, *"it would take 1.4 – 3.0 kg of lithium equivalent (7.5 – 16.0 kg of lithium carbonate) to support a 40-mile trip in an electric vehicle, before requiring recharge"* [22].

The use of materials that undergo insertion reactions as the electrochemically active component at the positive electrodes is an idea that was firstly applied in the 1970s, resulting in the development of the first rechargeable lithium batteries (RLBs). Two different approaches have been developed, so far, for the design of RLBs; in the first, the battery system utilises an insertion compound as the positive electrode and a lithium-metal foil as the negative electrode, forming the widely well-known *lithium-metal battery* (*Figure 1.5-a*).

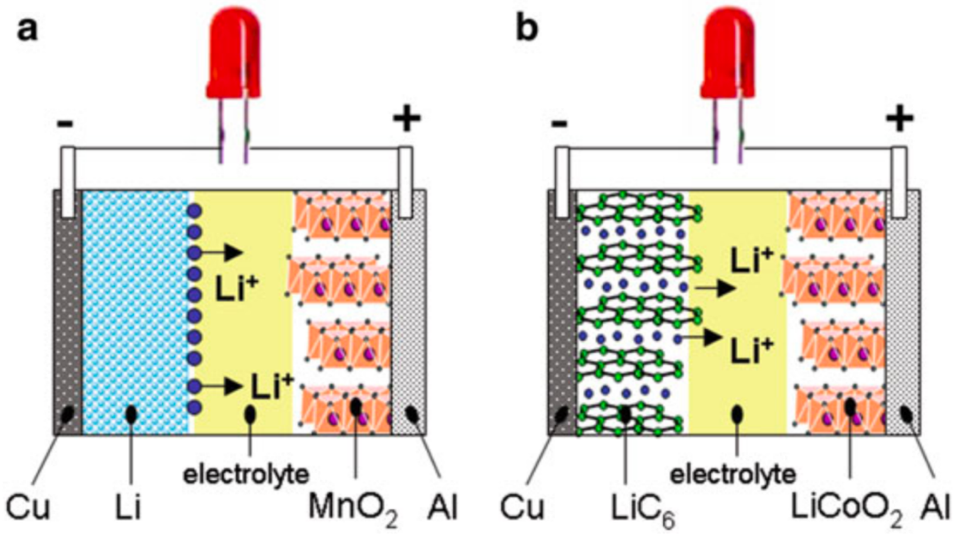

Figure 1. 5: Schematic presentation of two different rechargeable, lithium battery systems; (a) lithium-metal battery and (b) lithium-ion battery [11].

The second approach uses two open-structured materials as electrodes, in which the lithium ions can be shuttled from one intercalation compound, acting as lithium-ion source, to a second one which receives the lithium-ions during discharge. The exact same process is repeated reversibly during charge and this defines a *lithium-ion battery* (*Figure 1.5-b*). Lithium-ion batteries were initially known as “rocking chair”, “swing” or “shuttlecock” batteries, or occasionally “lithium metal-free, rechargeable batteries” [23].

Li or Li-ion batteries employing a solid electrolyte would exhibit high thermal stability, low rates of self- discharge (shelf life of 5–10 years or better), an ability to operate under a wide range of environmental conditions (temperature, pressure, and acceleration), and yield high energy densities of 0.3–0.7 $Wh \cdot cm^{-3}$ [17]. However, due to the high impedance of most lithium-ion conducting solids, their use as electrolytes is challenging. These issues are discussed further in Section 1.3.

1.2.2.1 Lithium-Metal Batteries

The first electrochemical application of intercalation compounds was as electrolytes in lithium-metal batteries (LMBs). This initially exploited the electron donor mechanism in transition-metal dichalcogenides MX_2 (X = S, Se). The prototype is the Li/Li_xTiS_2 system [24]. Batteries using MX_2 compounds can be considered as concentration cells with a lithium activity that varies with composition within a range of $0 \leq x \leq 1$.

As lithium is intercalated as ionic Li^+, the electro-neutrality of the host is maintained by ejection of an electron into the external circuit. This is generated by reduction of the transition-metal cation, the oxidation state of which varies during the process. The cell potential decreases with the Li^+ uptake into the host framework, which follows the simple Nernst equation:

$$\boldsymbol{V(x) = E^0 - \frac{RT}{F} \ln a(Li^+)} \qquad [1.23]$$

where, $a(Li^+)$ is the activity of Li^+ ions. It is important to note here that Li^+ ion activity increases with the decrease of the cell potential; a typical feature of Li-intercalation batteries. In the limits of the structural stability of the host, the electrochemical reaction is fully reversible.

Despite the significant developments that have occurred over the last decades, the use of LMBs remains inefficient because of several factors, including:

1. the unresolved control of the reactivity of lithium towards the electrolyte,
2. the SEI layer,
3. the formation of large lithium dendrites at the electrode-electrolyte interface causes internal short circuiting,
4. the increasing surface area upon cycling poses risks of overheating.

In fact, LMBs have a relatively low coulombic efficiency (~90 %) with organic carbonate solvents, and relatively short low cycle life due to the ceaseless growth of the passivation layer [25]. A study conducted by *Von Sacken et al.* [26] reports how thermal runaway is possible given the exothermic reactions between lithium metal and the electrolyte.

1.2.2.2 Lithium-Ion Batteries

As a principle, a lithium-ion battery (LiB) contain charge species (Li^+), while lithium has to present at some form for oxidation to occur at the anode (e.g. integrated in graphite, present as an alloy, etc.). These ions move between the two electrodes through an electrolyte, which must be a good ionic conductor and an electronic insulator. During charging, Li^+ is generated by the positive electrode (anode), flows across the electrolyte to the negative electrode (cathode), while electrons circulate through the external circuit. During the process, the positive electrode is oxidised (loss of electrons) and the negative electrode is reduced (gain of electrons). The procedure is followed reversibly during the discharge process. Ion transfer through the volume of a solid-state compound is a slow process, requiring optimisation [27]-[28].

Lithium ion batteries have a high energy density and they are more advantageous in terms of volume and weight, if compared to traditional lead-acid or Ni-MH batteries.

Maybe the most important disadvantage of Li-ion batteries is that a Battery Management System (BMS) is almost the only way to control and monitor the battery pack and compensate imbalances between cells. This way, a constant high capacity and a long life-span is ensured. The BMS must be able to constantly check each cell for thermal runaway and propagation phenomena related to other cells (e.g. battery explosions). One case where the use of a BMS is minimised, is the one of LiBs with iron phosphate and titanate electrodes, with studies showing that the lithium iron phosphate (LFP) / lithium-titanate (LTO) cell successfully passes safety tests for use in public transport [29].

1.2.3 Anode Challenges

The first, commercialised solid-state battery (Sony, 1991) consisted of $LiCoO_2$ and graphite as the active elements of the positive and negative electrodes, respectively. Since then, lithium-ion batteries (LiBs) have made considerable progress and are, currently, the primary energy storage devices in the transport and communications sectors, from laptop computers, to hybrid, electric vehicles. Much more recently, they have been integrated as back-up supply units and frequency regulators on smart grids [30]. Among others, these applications are expected to present high energy densities, high power, and safety. Considerable efforts have been made to develop novel electrodes which can meet these requirements [31-36].

The vital requirements for an anode are presented below [17]:

1. It must be light and accommodate as much Li as possible for the optimisation of the gravimetric capacity.
2. With respect to Li^0/Li^+, the redox potential must be as small as possible at any Li-concentration. As this potential is subtracted from the redox potential of the cathode material in order to give the overall cell voltage, smaller voltage ratio than anode potential.
3. It must present good electronic and ionic conductivity. The faster the transport of the lithium ions and electrons, the higher the power density of the cell.
4. It must not be soluble in the solvent component and must not react with the lithium salt of the electrolyte component.
5. It must meet safety requirements, including thermal stability, especially for use in transportation.

6. It must be cheap and environmentally friendly.

Graphite is considered as the standard material for anodes. The first work giving evidence of the insertion of lithium in graphite date back to 1955 [36] but it was confirmed by the synthesis of LiC_6 ten years later [37]. Another decade later, the reversible intercalation of lithium in graphite was discovered, enabling its use as an anode [38][39]. Increasing the Li content in LiC_6 is possible [37], but no reversible cycling beyond LiC_6 has been obtained. The theoretical capacity for the cycles between C and LiC_6 is ca. 372 $mAh{\cdot}g^{-1}$.

One of the main goals of the anode material research is the increase of this capacity value. However, in practice the capacity is more limited by the cathode, rather than the anode (the former typically within the range 140-200 $mAh{\cdot}g^{-1}$). Thus, cathode imposes a limit on the highest value of the capacity of the cell [40].

Graphite satisfies criteria (2) and (3) above well, since its potential versus Li metal is only 0.15-0.25 V and graphite is a semi-metal, with an electronic conductivity that exceeds 10^{-3} $S{\cdot}cm^{-1}$, at RT. LiC_6 is metallic with high Li-ion mobility varying within between 10^{-8} and 10^{-10} $cm^2{\cdot}s^{-1}$. To meet requirement (4), ethylene carbonate (EC) is used as a solvent when graphite is used as an anode. In the presence of an EC-based solvent, a solid-electrolyte interface (SEI) is formed at the surface of graphite particles during the initial cycles, preventing excessive solvent intercalation and acting as a good Li-ion conductor [41-45]. The use of more conductive solvents -such as propylene carbonate (PC)- is restricted because of side reactions with graphite, which affect the flow of Li^+. The amount of the ions should, always, be kept small enough to give them the time to enter graphite's "body". Otherwise, the lithium deposition could lead to safety issues [46][47]. Last but not least, regarding requirement (6), it should be noted that graphite is generally not expensive (except microcrystalline graphite, for example, which follows expensive manufacturing processes. It has been difficult to find a superior anode material to graphite. The only alternative, commercial anode material of note is the composite Sn/Co/C, developed by Sony in 2005 [48].

A lot of research has been conducted in recent years on the development of alternative anode materials [49-54]. Some of these include metal-containing anodes in the form of alloys or intermetallics [55], oxides, including TiO_2-based nanostructures [56-60] and graphene-based nanocomposites [61] and reviews have focused on the significant work on promising anode materials based on new nanotechnologies [62-71]. Some of the proposed materials can present a number of advantages [72-77], for example:

1. Resistance to expansion/contraction upon Li insertion/extraction by use of nanosized particles,
2. Larger surface to volume ratio implies a larger specific capacity, and a larger contact area with the electrolyte leading to high lithium-ion flux across the electrode/electrolyte interface,
3. Lithium diffusion and electronic conductivity are improved due to the reduction of the electron and Li path length, leading to batteries with enhanced power capability.

1.2.4 Cathode Challenges

Given the relatively low capacity, the cathode is very important in a battery system in terms of the energy density and the power density, but also the cost. The current most widely used cathode material is $LiCoO_2$. However, it is expensive, possesses limited practical capacity (< 140 $mAh \cdot g^{-1}$), and has stability problems at high temperatures in common electrolyte solutions, e.g., $LiPF_6$ salt in a mixture of alkyl carbonate solvents. Researchers mostly focus on cathode materials like $LiMn_2O_4$ spinel [78], $LiFePO_4$ [79], $LiNi_{1-x}MO_2$ (M = Co, Al) [80] and $Li_xM_yVO_z$ (M = metal such as Ca or Cu) [81] alternatives to $LiCoO_2$. The attention is focused on the development of reliable synthetic routes for these materials, their structural characterisation and electrochemical behaviour. Very high precision in structural analysis is needed to understand these solids, and synchrotron X-ray radiation (for *in situ* XRD [82], XANES [83], EXAFS [84]), high resolution electron microscopy/electron diffraction [85], and solid-state NMR [86], are among essential tools for this purpose.

The majority of cathode materials under investigation react in contact with commonly-used electrolyte solutions and, therefore, develop a rich surface chemistry [87]. Most of the lithiated transition metal-oxides above develop surface films due to spontaneous reactions with solution components [88]. As a result, researchers strongly believe that the electrochemical behaviour of most cathode materials depends strongly on their surface chemistry. Just like the case of Li and Li-C anodes, many types of cathodes for Li-ion batteries can be considered as SEI [89] electrodes.

Despite the high precision that can be achieved in the analysis of bulk, the detailed analysis of cathode surfaces is much more challenging. This difficulty can arise from the extremely thin surface films that are formed, whose composition and structure can be deeply affected by contaminants in the solution phase (even at ppm levels).

1.2.5 Solid – Electrolyte Interphase (SEI)

The solid-electrolyte interphase (SEI) is a protecting layer formed on the negative electrode of Li-ion batteries as a result of electrolyte decomposition. Battery performance, irreversible charge "loss", rate capability, cyclability, exfoliation of graphite and safety are highly dependent on the quality of the SEI. Therefore, if the chemistry of the SEI formation and the manner in which each component affects battery performance are understood, SEI could be tuned to improve battery performance.

Closely related to the nature of the electrolyte used, the SEI usually reaches a thickness of 25–100 *Å*, with electrons not showing any significant tunnelling through a film of such thickness. Ideally, *"the electrolyte chosen should give rise to a SEI in which the cation transport number for the migration of lithium ions approaches unity"* [17].

As proposed by Xu *et al.* [142], two main aspects affect and determine the SEI's behaviour:

1. the static stability of the SEI, that relates to the standing storage of the battery,
2. the dynamic stability, that relates to reversibility of the SEI layer.

Although the formation of the SEI gives lithium electrodes static stability, when functioning in non-aqueous solvents, it, also, gives rise to a varying surface morphology. As a result, the current density across the electrodes' surface is unevenly distributed during lithium deposition, leading to the direct growth of dendrites. However, it is important to note that, fortunately, dendrite formation only arises under extreme conditions such as, under extremely low temperatures which allow lithium deposition on the carbon anode.

To summarise, an "ideal" SEI for lithium ion batteries, should meet the following requirements [17]:

(1) electron transference number, $t_e = 0$,
(2) high ionic conductivity,
(3) uniform morphology and chemical composition,
(4) good adhesion to the anode surfaces,
(5) satisfactory mechanical strength and flexibility,
(6) low solubility.

It would be interesting to note here that SEIs are important not only to the negative electrodes, but also exist and affect the positive electrodes significantly in lithium-ion batteries.

The SEI is formed in two stages: at the first stage the SEI is richer in inorganic components compared to the SEI during the second stage, at higher voltages. Also, the first stage produces more gaseous products. The main route towards control of SEI formation involves chemical coating of the cathode surface via an electrochemical reduction of various additives. These additives reduce gas generation while, at the same time, increase the SEI's stability [17].

1.3 Solid-State Electrolytes

One of the ongoing efforts in LIB/LMB research focuses on the suppression of dendritic growth, either through the use of solid electrolytes that act as mechanical barriers, or through development of electrolytes which produce a suitable passivation layer, widely known as the "*solid-electrolyte interphase*" (SEI). Safety concerns have led to the extensive use of LIBs, rather than LMBs, as no entirely successful strategy has been developed to suspend the growth of dendrites.

Lithium-ion batteries are currently used in a wide range of commercial applications; from electronic devices to transport and aerospace technologies. The common commercial Li-ion batteries use aprotic, organic liquids as components in their electrolytes which present high dielectric constant and can be used as solvents for salts, while also satisfy the window of electrochemical stability. However, concerns regarding their high vapor pressure have risen in the face of fire and explosion hazards. This fact, together with the low-stability cathodes that are currently used (e.g. oxides), create an explosive combination. The bigger the scale in which, lithium-ion batteries will be used (electric cars), the bigger the danger, especially, when charge-discharge processes are carried out at high rates. Therefore, it can be easily understood why the need of safer electrolytes and electrolyte systems are today more than vital when it comes to LMB and LIB manufacturing, especially for large scale applications.

1.3.1 An Ideal Electrolyte

A lithium battery consists of two electrodes (anode and cathode) and an electrolyte. The right choice of electrolyte depends on the electrode materials in use and the chemistry of the electrode-electrolyte interfaces. The "ideal" solid-state electrolyte should demonstrate [17]:

1. a large window of phase stability (no vaporisation or crystallisation),
2. non-flammability,
3. a wide electrochemical window,

4. non-toxicity,
5. abundant availability,
6. resistance to corrosion against other battery components,
7. an environmentally friendly nature,
8. robustness against electrical, mechanical, and thermal stress,
9. good wetting properties at the electrolyte-electrode interface.

Considering the wide range of published work, it is safe to say that a truly "ideal" electrolyte does not yet exist.

1.3.1.1 Li-ion Conduction Theory in Solid-State Electrolytes

Lithium conduction in solid-state electrolytes is a result of the existence of crystal defects, existing in real crystals. According to Gellings *et al.* [90], "*point defects are atomic defects whose effects are limited only to their immediate surroundings*". These are either ionic vacancies or interstitial atoms/ions and ionic conduction is a result of the motion of defects.

Frenkel and Schottky defects are the most common. The former is "*intrinsic and stoichiometric defects, accompanied by an interstitial ion*", while Schottky defects "*are anion vacancies accompanied by a cation vacancy*" [91].

The formation of intrinsic defects is driven by thermal energy and the number of defects obeys an Arrhenius-type equation [91]:

$$\boldsymbol{N_D = N exp\left[-\frac{E_F}{2kT}\right]} \qquad [1.24]$$

where, N_D is the number of defects, N the number of ion pairs, E_F the energy of formation, k the Boltzmann constant and T the temperature.

The conductivity of a material with multiple conducting species is expressed by Equation 1.25:

$$\boldsymbol{\sigma = \sum n_j q_j \mu_j} \qquad [1.25]$$

where, σ is the total conductivity, n_j the density, q_j the charge and μ_j the mobility of each conducting species.

The total conductivity of a mixed conducting material is calculated as the sum of the ionic and electric conductivities:

$$\boldsymbol{\sigma = \sigma_i + \sigma_e} \tag{1.26}$$

Transference numbers are the fraction of the total electrical current carried in an electrolyte by a given ionic species. These parameters are, also, defined to characterise the ionic and electronic contributions to the total conductivity:

$$\boldsymbol{t_i = \frac{\sigma_i}{\sigma}} \tag{1.27-a}$$

$$\boldsymbol{t_e = \frac{\sigma_e}{\sigma}} \tag{1.27-b}$$

where, t_i and t_e are ionic and electronic transference numbers, respectively. The sum of t_i and t_e is unity [90].

Ionic conduction is, also, dependent on Arrhenius temperature:

$$\boldsymbol{\sigma_i = \frac{A}{T} exp\left[-\frac{E_a}{kT}\right]} \tag{1.28}$$

where A, according to collision theory, is the frequency of collisions in the correct orientation and E_a the activation energy.

The mobility of charge is calculated as follows:

$$\boldsymbol{\mu = \frac{qD}{kT}} \tag{1.29}$$

where, D is the diffusion coefficient.

The motion of a single particle, moving from an occupied site to an energetically equivalent unoccupied one can be described by a "*random-walk theory*" [92], with the diffusion coefficient expressed by Equation 1.30:

$$\boldsymbol{D} = \left[\frac{z}{2d}\right] \boldsymbol{l}^2(\mathbf{1} - \boldsymbol{c})\boldsymbol{v_h} \qquad [1.30]$$

where, $d = 1, 2, 3$ (for one-, two-, or three-dimensional motion), l the jumping distance, c the concentration of mobile ions and z the number of the similar nearest neighbours. The jump frequency (v_h) is expressed by Equation 1.31:

$$\boldsymbol{v_h} = \boldsymbol{v_0 exp}\left[\frac{-\Delta G_m}{kT}\right] \qquad [1.31]$$

where, v_0 is the attempt frequency and (ΔG_m) the migration free energy, expressed by Equation 1.32:

$$\boldsymbol{\Delta G_m} = \boldsymbol{\Delta H_m} - \boldsymbol{T\Delta S_m} \qquad [1.32]$$

where, ΔH_m is the migration enthalpy and ΔS_m is the migration entropy. By combining Equations 1.25 and 1.29 are combined, the Nernst-Einstein equation is derived (*Equation 1.33*):

$$\boldsymbol{\sigma_i} = \frac{N_c q^2 D}{kT} \qquad [1.33]$$

where, N_c is the number of mobile ions or defects. It is observed that the ionic conductivity is proportional to N_c and D parameters.

1.3.1.2 Structural Properties and Chemistry of an Ideal Solid-State Electrolyte

Crystalline materials constitute one type of candidate solid-state electrolyte, offering an alternative to amorphous materials [93]. The two most important parameters which affect and determine significantly the ionic conductivity of a crystalline solid are the ion valency and the ion size. Ion valency influences the ionic conductivity and diffusivity inversely; as valency increases, the other two decrease. This is a result of the electrostatic interactions between the ions within the crystal structure. Accompanied by an important increase of the activation energies, for example, during the transition from monovalent to trivalent ions-the diffusion coefficient can present a decrease around three orders of magnitude in lithium sulphates [94-95].

Ionic radius also plays an important role in influencing ionic conductivity. The highest diffusivities can be achieved by ions of an intermediate size [96]. In general, ions that are "too small" occupy sites with a large *electrostatic well* [2], leading to high activation energies and slow diffusion. In contrast, ions that are "too large" experience larger forces when diffusing between the bottlenecks of the skeleton structure, producing reduced diffusivities and large activation energies. Grain boundaries should also be taken into consideration [97-102]. Grain boundaries exhibit resistances that are higher than that of the respective bulk solid, resulting in decreased values of ionic conductivity [103-105].

The available volume for lithium ions to move inside a crystal structure is, actually, the most important parameter affecting lithium ionic conductivity in lithium-ion batteries and applies to all the different structural families. Adam and Swenson [106] have proposed a novel method to determine the diffusion pathway, based on the *bond valence method.* The main concept in this method is the notion of the "valence" of a chemical bond between the atoms i and j, s_{i-j}, which is calculated by Equation 1.34:

$$\boldsymbol{s_{i-j} = exp\left[\frac{R_0 - R}{b}\right]} \qquad [1.34]$$

where, $\boldsymbol{R}$ is the bond length and $\boldsymbol{R_0}$ and $\boldsymbol{b}$ are constants empirically determined for each bond type. For many bond types (but not all), b is found to be close to 0.37 Å. A list of bond valence parameters for different bond types can be found at the web site of the International Union of Crystallography [3]. As explained by Bachmann et al. [107];

"To determine the diffusion pathway, the unit cell is divided into a fine 3D grid. At each node of this grid, the bond valence sum of the diffusing species is

---

[2] An *electrostatic well* is the region surrounding a local minimum of potential energy. Energy captured in a potential well is unable to convert to another type of energy because it is captured in the local minimum of a potential well.

[3] https://www.iucr.org/resources/data/data-sets/bond-valence-parameters

calculated. The diffusion pathway in crystalline and amorphous solids corresponds to a percolating region, where the bond valence mismatch of the mobile species, defined as the difference between the bond valence sum and the formal charge, is below a certain threshold."

In case this threshold is too small, there will be no percolating diffusion pathway but only disconnected regions. In the case that the threshold is too large, the entire unit cell will become part of the diffusion pathway, which is something not normally expected to be observed.

1.3.1.3 State-of-the-art Solid-State Electrolytes

The skeleton of a crystal structure consists of mobile, metal and non-metal ions which present the ability to form polyhedra with active ligands. Some of the ions proved to be mobile in solids include H^+, Li^+, Na^+, K^+, F^-, Cl^-, Cu^+, Ag^+, Mg^{2+} & O^{2-}.

To give an example, AgI was one of the first solid-state, ionic compounds to show high ionic conductivity (10^{-6} – $4.5x10^{-4}$ $S{\cdot}cm^{-1}$, at 325 K – 420 K) **[108]**. Sodium-ion-conducting ß-alumina (10^{-2} $S{\cdot}cm^{-1}$, at 400 K) **[109]** and Sodium (**Na**) **S**uper **I**onic **CON**ductor (NASICON) (order of 10^{-4} – 10^{-2} $S{\cdot}cm^{-1}$, at 300 K – 500 K) **[110-113]** followed, with various, fast lithium-ion conductors also being discovered over the last two decades.

Several important structural families have been shown to achieve high ionic conductivities, with values ranging from 10^{-2} to 10^{-3} $S{\cdot}cm^{-1}$, at RT. Some of these are described in more detail below:

A. LISICON(-like) Family

The Lithium (**Li**) **S**uper **I**onic **CON**ductor (LISICON) and thio-LISICON structures crystallise with structures similar to $\gamma - Li_3PO_4$ (orthorhombic, space group $Pnma$) in which the cations are tetrahedrally coordinated **[114]**. The structure can be described by distorted close packed oxygen atoms, whose packing planes are perpendicular to the c-axis, and in which cations (e.g. lithium and/or phosphorous) are distributed in two crystallographically distinct tetrahedral interstices, forming parallel, one-dimensional chains along the a-axis (*Figure 1.6*).

In these structures, the lithium ions located in LiO_4 tetrahedra [116]. Compositions like $Li_{3+x}(P_{1-x}Si_x)O_4$ [117-119] are possible, giving rise to fast, lithium-ion conduction and the *"LISICON-like"* family. The excess lithium ions created in these cases cannot be accommodated in the tetrahedral sites of the structure and, therefore, occupy interstitial sites, making the adjacent lithium–lithium ion distance unusually short and resulting in high conductivity, with an indicative value of $3{\cdot}10^{-3}$ $S{\cdot}cm^{-1}$ [107].

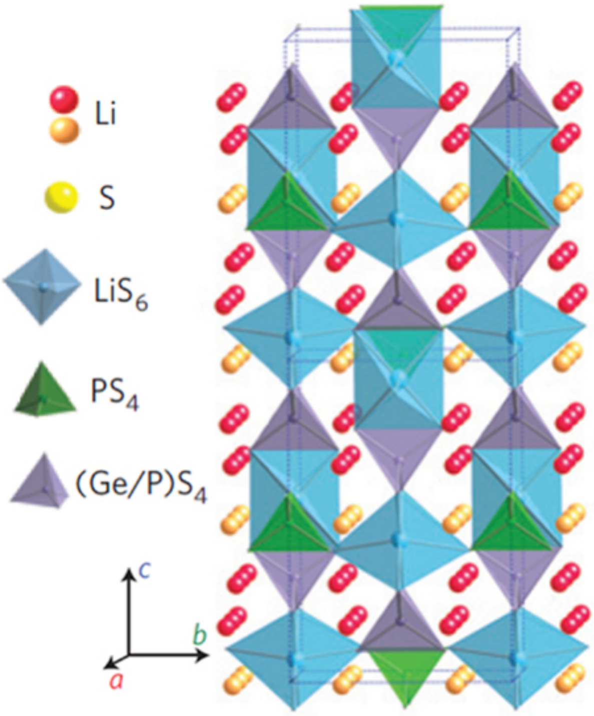

Figure 1. 6: Representative LISICON structure, the crystal structure of $Li_{10}GeP_2S_{12}$.The framework structure and lithium ions that participate in ionic conduction [115].

B. Lithium Argyrodite Family

Lithium argyrodites, Li_6PS_5X (X = Cl, Br, I), have been recently discovered and studied because of their fast, lithium-ion conductive properties ($\sigma \geq 7 \cdot 10^{-3}$ S/cm^{-1}) [120]. They crystallise into a structure presenting a close packing of tetrahedral anions and built up a cubic structure (space group $F43\bar{m}$) [120], [121], [122-124] (*Figure 1.7*).

Phosphorus atoms fill tetrahedral interstices, forming a network of isolated PS_4 tetrahedra, while lithium ions are randomly distributed in the remaining tetrahedral interstices.

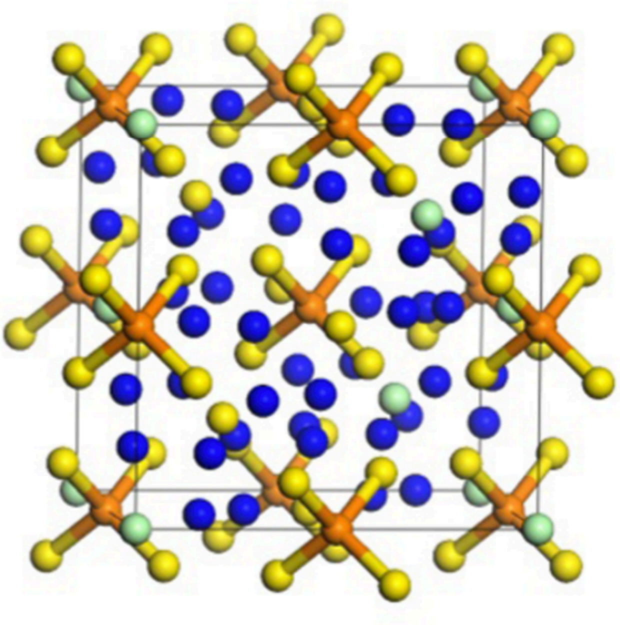

Figure 1. 7: Representative lithium argyrodite structure. Unit cell of argyrodite Li_6PS_5Cl. Blue spheres represent Li atoms, orange represents phosphorous, yellow represents sulphur and green represents chloride atoms. [125].

Among Li_6PS_5I, Li_6PS_5Cl and Li_6PS_5Br, the first presents significantly lower conductivity due to the difference in the connectivity of the hexagonal cages and the distribution of lithium among the different sites, together with the disorder on the S^{-2}/X^{-} sublattice. This is one indicative example of the importance of structure disorder in promoting high ionic conductivity [126].

C. NASICON(-like) Family

NASICON compounds have a general formula of $AM_2(BO_4)_3$, where the A site is occupied by Na^+ and the M site is occupied by tetra-valence ions (Ge^{+4}, Ti^{+4}, Zr^{+4}).

The NASICON structure is usually rhombohedral (space group $R\bar{3}c$) (*Figure 1.8*). Distorted monoclinic and orthorhombic phases have also been reported [127].

In these structures, lithium occupies two different sites: the M1, 6-fold coordinated sites (octahedral symmetry) between two MO_6 octahedra, and the M2, 8-fold coordinated sites between two columns of MO_6 octahedra, where M = M_1 or M_2. The structures' conductivity present conductivities of the order of 10^{-4} $S{\cdot}cm^{-1}$ [128].

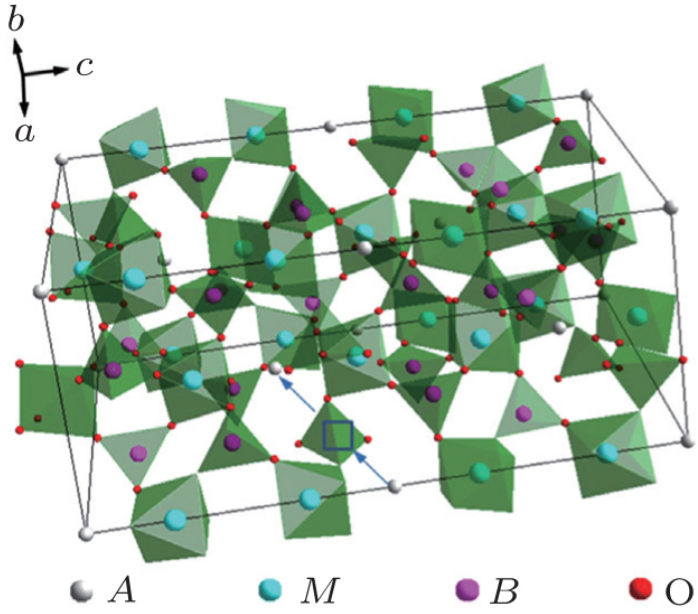

Figure 1. 8: Representative NASICON structure. NASICON compounds have a general formula of $AM_2(BO_4)_3$, where the *A* site is occupied by alkali atoms (Li^+, Na^+, K^+), and the *M* site is occupied by tetra-valence ions (Ge^{+4}, Ti^{+4}, Zr^{+4}) [129].

Lithium ion migration occurs via hopping between these two sites. The partial occupancy of lithium ions on these sites are vital for fast lithium-ion conduction, as vacancies are required at the intersection of the conduction pathways to give access to three-dimensional diffusion within the structure [130-132]. As an additional advantage, most NASICON-like structures are stable in air, water at high potentials [128], with existing exceptions [133-135].

D. Garnet Family

The ideal garnets exhibit a general chemical formula of $A_3B_2(XO_4)_3$ (A = Mg, Ca, La, Y, rare earth; B = Fe, Ge, Ga, Al, Mn, V, Ni; X = Al, Ge, Si) where A, B and X are eight, six and four oxygen coordinated cation sites, which crystallise in a face centred cubic structure with the space group $Ia\bar{3}d$ (*Figure 1.9*) [136].

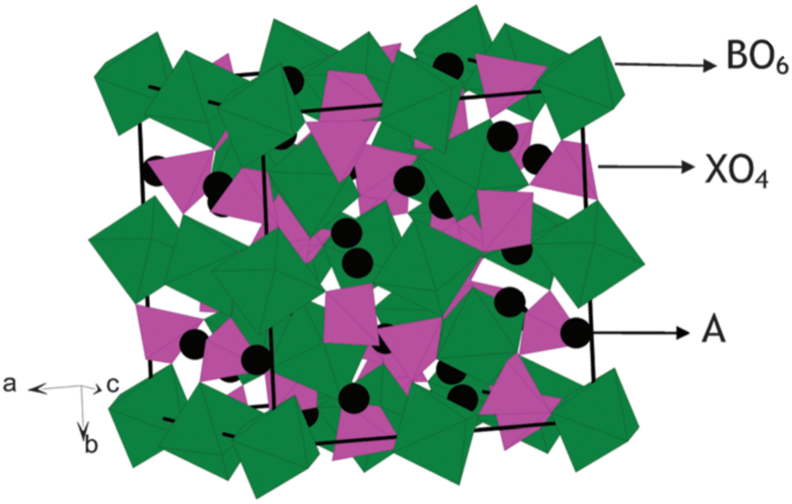

Figure 1. 9: Representative garnet structure with the general chemical formula of $A_3B_2(XO_4)_3$ (A = Mg, Ca, La, Y, rare earth; B = Fe, Ge, Ga, Al, Mn, V, Ni; X = Al, Ge, Si) [136]

For enhanced ionic conductivity at RT (~ 10^{-3} $S{\cdot}cm^{-1}$), more lithium can be added into the structure by adjusting the valence of the A and B cations, leading to several stoichiometries of lithium-conducting garnets; $Li_3Ln_3Te_2O_{12}$ (Ln = Y, Pr, Nd, Sm−Lu), $Li_5La_3M_2O_{12}$ (M = Nb, Ta, Sb), $Li_6ALa_2M_2O_{12}$, (A = Mg, Ca, Sr, Ba; M = Nb, Ta) and $Li_7La_3M_2O_{12}$ (M = Zr, Sn) [137]. These garnet lithium electrolytes have, also, been found to have high thermal stabilities (up to 900 ^0C) and exhibit high stability against lithium electrodes [138].

E. Perovskite Family

Perovskite structures have the general formula ABO_3, and are ideally cubic (space group $Pm\bar{3}m$). They consist of A-site ions (typically alkaline-earth or rare- earth elements) at the corners of a cube, B ions (typically 3*d* transition metal ions) at the cell body centre and oxygen atoms at the face-centre positions. A sites are of 12-fold coordination and B sites of 6-fold coordination, with BO_6 octahedra sharing corners (*Figure 1.10*). In 1993, the first series of the perovskite family presenting high ionic conductivity (10^{-3} *S·cm*$^{-1}$) was synthesised at RT. The structure's formula was $Li_{3x}La_{\frac{2}{3}-x}TiO_3$, with Li and La occupying the A sites. [129]

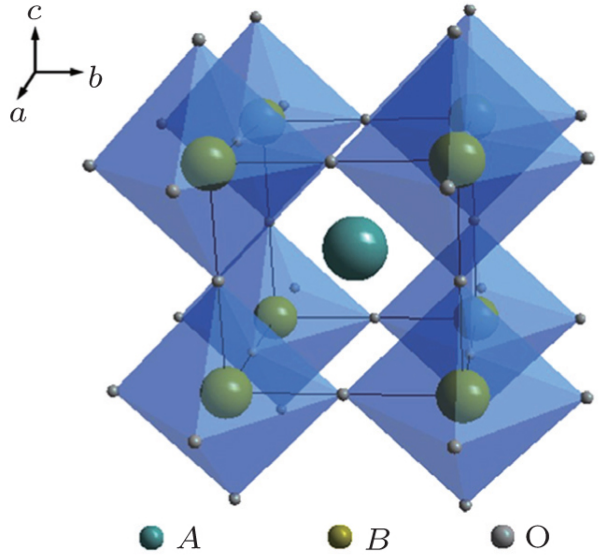

Figure 1. 10: Representative perovskite structure consisted of A-site ions (typically alkaline-earth or rare- earth elements) at the corners of a cube, B ions (typically 3d transition metal ions) at the cell body centre and oxygen atoms at the face-centre positions [129].

Lithium can be introduced in perovskites at their A sites, through aliovalent doping. Lithium introduction produces vacancies and thus can significantly influence the ionic conductivity. Diffusion of lithium ions occurs by jumping in the *ab* plane, to an adjacent vacancy, through a square-planar bottleneck, formed octahedra with oxygens at their corners, at RT [139-140]. Ionic conductivity can be increased even more, following an increase of the bottleneck's size.

1.3.2 Challenges

1.3.2.1 Passivation Phenomena at Electrode-Electrolyte Interfaces

During the very first cycles in the operation of a lithium-ion battery's operation, the electrolyte reacts with both the anode and the cathode and these reactions lead to the formation of passivating layers (SEI), proven to be protective for the electrodes, as well. These layers prevent the vigorously destructive corrosion of the electrodes and deactivation of the electrolyte. They also control the reaction rates of the battery and allow ionic conduction through the films. Aurbach *et al.* have studied the surface chemistry of this phenomenon extensively [141].

1.3.2.2 Irreversible Capacity Loss

Due to the SEI's formation on both electrodes of the battery, a certain amount of electrolyte is constantly consumed and as an irreversible phenomenon, the SEI formation immobilises a certain amount of Li^+. Hence, the consumption of the lithium-ion source -especially, during the initial cycles- leads the cell to permanent capacity loss. Therefore, the right material choices for the anode-electrolyte-cathode system are more than vital for an efficiently functioning battery.

1.3.2.3 Temperature Range

The majority of commercial solid-state electrolytes consist of two essential components: $LiPF_6$ as salt and mixed organic solvent; at least binary mixing where the ethylene carbonate (EC) is an important component. It is proposed that, usually, one of them is responsible for lower temperature fluctuations (EC) and the other one for higher temperature fluctuations ($LiPF_6$). Attempts for minimisation of these discrepancies work with additives towards the development of "functional electrolytes" [142].

1.3.2.4 Thermal Runaway

Because of the fact that lithium cells are subjected to massive electrical, mechanical and thermal stress, the possibility of thermal runaway is increased, raising concerns over safety. This is a huge issue, as it can be a product recall factor when it comes to batteries manufactured for use in electric cars and/or aircrafts. A range of flame-retardant or non-flammable electrolytes have been extensively investigated, including the incorporation of additives **[142]** or ionic liquids [143]. Research in this area is ongoing.

1.3.2.5 Ion Transport

Ion transport through the bulk electrolyte is, also, one of the most important factors in battery design. Ion conductivity in non-aqueous solutions is much lower than in aqueous ones, most commonly less than half. Generally, it has been observed that, the higher the bulk ion conductivity of a solid-state electrolyte, the more conductive the SEI **[142]**.

1.3.3 Complex Hydrides and Halides as Solid-State Electrolytes

1.3.3.1 Lithium Complex Hydrides

Lithium complex hydrides have been studied recently as they present good Li^+ conductivity. Their low densities which, eventually, lead to light LIBs, is another advantage of them [145]. These compounds present satisfactory thermal stabilities, deriving from the strong covalency between hydrogen and metals (or/and non-metals) in the case of complex anions. Additionally, it is highly unlikely for them to demonstrate decomposition phenomena at RT **[146]**.

$LiBH_4$ was first synthesised in 1940 [147], but it was only in 2007 when it was finally studied as a potential candidate for use in solid-state battery systems (*See more in Chapter 3 – 3.1*). The combination of $LiBH_4$and LiI with $LiNH_2$ in 2009 led to the synthesis of three new electrolytes, $Li_2(BH_4)(NH_2)$, $Li_4(BH_4)(NH_2)_3$ **[148]** and

$Li_3(NH_2)_2I$ [149], demonstrating ionic conductivities above 10^{-4} $S{\cdot}cm^{-1}$, at RT. In 2010 studies were also focused on $LiAlH_4$ and Li_3AlH_6 [150-151]. However, these compounds were quickly set aside as they presented ionic conductivities of the order of 10^{-9} $S{\cdot}cm^{-1}$, at 393 K.

In 2012, lithium rare earth mixed borohydride-halides were shown to exhibit high ionic conductivities (1.03 x 10^{-4} $S{\cdot}cm^{-1}$), at 293 K [152-153]. The high values of ionic conductivity were attributed to disordered Li-sites creating continuous conducting paths for Li^+, following a similar behaviour to $Li_{10}GeP_2S_{12}$ [154] and $Na_2(BH_4)(NH_2)$ [155].

Metal dodeca-borates ($M_{2/n}B_{12}H_{12}$, where n is the valence of metal M), were first suggested as candidate solid-state electrolytes, in 2014, due to their high stability, thanks to the icosahedral $[B_{12}H_{12}]^{-2}$ ion at high temperatures [156]. In 2015, He *et al.* [157] suggested that the addition of a second metal in the above structures, leading to formation of bimetallic dodeca-borates, could improve their ionic conductivity. This hypothesis was based on the theory that the coexistence of bimetallic cations could lead to a synergistic effect on the mobility of each ion. Eventually, based on that, they managed to synthesise the bimetallic dodeca-borate $LiNaB_{12}H_{12}$ by sintering $LiBH_4$, $NaBH_4$ and $B_{10}H_{14}$. The obtained $LiNaB_{12}H_{12}$ demonstrated ionic conductivities between 10^{-5} $S{\cdot}cm^{-1}$ and 0.79 $S{\cdot}cm^{-1}$, at 550 K [157-158]. Lithium deca-borate, $Li_2B_{10}H_{10}$, was reported, the same year, as a solid-state electrolyte candidate [159], with its sodium analogue, $Na_2B_{10}H_{10}$, displaying one of the highest ionic conductivity ever observed in solid electrolytes (0.01 $S{\cdot}cm^{-1}$, at 383 K) [160].

$LiCB_{12}H_{12}$, was the latest example of borane-derived materials synthesised. It demonstrated a total ionic conductivity of 10^{-6} $S{\cdot}cm^{-1}$, at RT, undergoing a phase transition at 400 K, reaching conductivities of 0.1 $S{\cdot}cm^{-1}$.

Lithium ternary hydrides and halides are widely studied, nowadays, as potential candidates for use Li-ion batteries. Their high ionic conductivity, thermal stability and non-flammable properties render them to be some of the most promising material families. It is important to note that, among them, $LiBH_4$ and $LiAlH_4$ are the only thermally stable ones regarding Group XIII of the Periodic Table [161].

$LiInBr_4$ demonstrates the greater interest among the halo-complex lithium salts, $M^IM^{III}X_4$ (M^I = Li, M^{III} = Al, Ga and In, X = Cl, Br and I). It is the only halo-complex reported that shows a phase transition similar to $LiBH_4$. The compound demonstrates ionic conductivity of 10-3 $S{\cdot}cm^{-1}$, at 313 K [162].

1.4 Scope of the Work

This project had been focused on the stabilisation of the HP-phase of $LiBH_4$ at RT. Our efforts have been focused on the investigation of the most simple and efficient way to synthesise, stabilise and characterise this promising Li-ion conducting material, at room temperature. The synthesis approach consisted of conventional and energy-efficient synthetic methods, such as thermal treatment and ball milling. These particular methods used following their successful application for the stabilisation of the hexagonal, HT-phase of $LiBH_4$, at RT, by previous work in our group [155].

Our efforts were focused on stabilising the cubic, HP-phase of $LiBH_4$ at RT, by mixing $LiBH_4$ - $NaBH_4$ - LiI and, therefore, affecting the Li^+/Na^+ and BH_4^-/I^- ratio at each ion centre. Forcing the atoms/ions to share their positions changes the local bonding at each centre and determines the extended structure as a result.

The stabilisation of the high-pressure phase of $LiBH_4$ (HP-$LiBH_4$) with Na^+ at ambient conditions will be described. Two different synthesis approaches will be reported.

The first objective of this project was the development of an improved synthesis process, in terms of time and complexity, including mechanochemical milling and thermal treatment of the materials. Following the successful stabilisation of HP-

$LiBH_4$, at RT, the structural characterisation of the obtained compounds took place.

1.5 References

1. Th. Edison, in *The Electrical Journal*, University of Michigan, Michigan, 1883, vol. **10**, ch. “Storage batteries”.
2. Y. Masaki, R.J. Brodd and A. Kozawa, in *Lithium-Ion Batteries: Science and Technologies*, Springer Science & Business Media, New York, NY, 2009, ch.1, pp. 1-7.
3. Tesla Online, https://www.tesla.com/en_GB/blog/tesla-motors-surpasses-2007-model-year-sales-goals?redirect=no, (accessed 2010).
4. M. Duvall, in *Comparing the Benefits and Impacts of Hybrid Electric Vehicle Options for Compact Sedan and Sport Utility Vehicles*, Technical Report of EPRI, 2002.
5. X. Li, L.A.C. Lopes and S.S. Williamson, presented in part at the IEEE Power & Energy Society General Meeting, 2009.
6. L. Dickerman and J. Harrison, *IEEE Power and Energy Magazine*, 2010 **8**, 55-61.
7. R.C. Green II, L. Wang and A. Mansoor, *Renewable and Sustainable Energy Reviews*, 2011, **15**, 544-553.
8. R.M. Dell, D.A.J. Rand, *Journal of Power Sources*, 2001, **100**, 2–17.
9. P.J. Hall, E.J. Bain, *Energy Policy*, 2008, **36**, 4352–4355.
10. F. Faure, PhD thesis, Grenoble INP, 2003.
11. H. Ibrahim, A. Ilinca and J. Perron, *Renewable & Sustainable Energy Reviews*, 2008, **12**, 1221-1250.
12. B. Dunn, H. Kamath and J.-M. Tarascon, *Materials for Grid Energy*, 2011, **334**, 928.
13. C. Sun, J. Liu, Y. Gong, D.P. Wilkinson and J. Zhang, *Nano Energy*, 2017, **33**, 363– 386.
14. J.B. Goodenough and Y. Kim, *Chemistry of Materials*, 2010, **22**, 587-603.
15. J. Augustynski, F. Dalard, J.Y. Machat and J.C. Sohm, *US Patent 3*, 1975, **902**,921.
16. C.M. Julien and G.A. Nazri, *Solid State Batteries: Materials Design and Optimisation*, Kluwer, Boston, 1994.

17. C.M. Julien, A. Mauger, A. Vijh and K. Zaghib, *Lithium Batteries*, Springer International Publishing, Switzerland, 2016.

18. W. Weppner and R. Huggins, *Journal of the Electrochemical Society*, 1977, **124**, 1569–1578.

19. C.M. Julien, A. Mauger, K. Zaghib and A. Vijh, in *Lectures of the Workshop on Materials Science for Energy Storage*, Chennai, India, 18–22, 2010.

20. D. Linden and T.B. Reddy, *Handbook of Batteries*, 3rd edn., McGraw-Hill, New York, 2001.

21. H.J. Bergveld, W.S. Kruijt and P.H.L. Notten, *Battery management systems: Design by Modelling*, Kluwer Academic Publishers, Dordrecht, 2002.

22. T.G. Goonan, *Lithium Use in Batteries. US Geological Survey Circular 1371*, Reston, Virginia, 2012.

23. K. Ozawa, *Lithium-Ion Rechargeable Batteries*, Wiley, Weinheim, 2009.

24. M.S. Whittingham, *Progress in Solid State Chemistry*, 1978, **12**, 41–99.

25. H. Ota, *Journal of the Electrochemical Society*, 2004, **151**, 437–446.

26. U. Von Sacken, E. Nodwell, A. Sundher and J.R. Dahn, *Journal of Power Sources*, 1990, **54**, 240–245.

27. C. De Las Casas and W.Z. Li, *Journal of Power Sources*, 2012, **208**, 74–85.

28. M. Winter, K.-C. Moeller and J.O. Besenhard, in *Lithium batteries: Science and Technology*, ed. G. Pistoia and G.A. Nazri, Springer, New York, NY, 2003.

29. H. Fujimoto, K. Tokumitsu, A. Mabuchi, N. Chinnasamy and T. Kasuh, *Journal of Power Sources*, 2010, **195**, 7452–7456.

30. K. Zaghib, A. Mauger and C.M. Julien, in *Rechargeable lithium batteries: from fundamentals to* applications, ed. A.A. Franco, Woodhead Publications, Oxford, 2014.

31. K. Zaghib, A. Mauger and C.M. Julien, *Journal of Solid State Electrochemistry*, 2012, **16**, 835–845.

32. K. Zaghib, A. Guerfi, P. Hovington, A. Vijh, M. Trudeau, A. Mauger, J.B. Goodenough and C.M. Julien, *Journal of Power Sources*, 2013, **232**, 357–369.

33. C.M. Julien and A. Mauger, *Ionics*, 2013, **19**, 951–988.

34. C.M. Julien, A. Mauger , K. Zaghib and H. Groult, *Inorganics*, 2014, **2**, 132-154.

35. D. Liu, W. Zjhu, J. Trottier, C. Cagnon, F. Barray, A. Guerfi, A. Mauger, H. Groult, C.M. Julien and J.B. Goodenough, *RSC Advances*, 2014, **4**, 154–167.

36. A. Herold, *Bulletin de la Société Chimique de France*, 1955, **187**, 999.

37. R. Juza and V. Wehle, *Nature*, 1965, **52**, 560.

38. J.O. Besenhard and G. Eichinger, *Journal of Electroanalytical Chemistry*, 1976, **68**, 1–18.

39. G. Eichinger G and J.O. Besenhard, *Journal of Electroanalytical Chemistry*, 1976, **72**, 1–31.

40. U. Kasavajjula, C. Wang and A.J. Appleby, *Journal of Power Sources*, 2007, **163**, 1003–1039.

41. W.A. Van Schalkwijk and B. Scrosati, *Advances in Lithium-Ion Batteries*, Kluwer, New York, NY, 2002.

42. G.A. Nazri and G. Pistoia, *Lithium Batteries: Science and Technology*, Kluwer, New York, NY, 2003.

43. K.E. Alifantis, S.A. Hackney and R. Kumar, *High energy density lithium batteries: materials, engineering, applications*, Wiley VCH, Weinheim, 2010.

44. A.S. Arico, P. Bruce, B. Scrosati, J.M. Tarascon and W. Van Schalkwijk, *Nature Materials*, 2005, **4**, 366–377.

45. P. Verma, P. Maire P and P. Novak, *Electrochimicha Acta*, 2010, **55**, 6332-6341.

46. A.K. Shukla and T.P. Kumar, *Current Science*, 2008, **94**, 314–331.

47. M. Winter, J.O. Besenhard, M.E. Spahr and P. Novak, *Advanced Materials*, 1998, **10**, 725–763.

48. Sony Press News, http://www.Sony.net/SonyInfo/News/Press/200502/05-006E/index.html, (accessed 2005).

49. M.V. Reddy, G.V. Subba Rao and B.V.R. Chowdari, *Chemical Review*, 2013, **113**, 5364-5457.

50. B. Scrosati and J.J. Garche, *Journal of Power Sources*, 2010, **195**, 2419-2430.

51. M.G. Kim and J. Cho, *Advanced Functional Materials*, 2009, **19**, 1497–1514.

52. C.M. Park, J.H. Kim, H. Kim and H.J. Sohn, *Chemical Society Reviews*, 2010, **39**, 3115–3141.

53. A.D.W. Todd, P.P. Ferguson, M.D. Fleischauer and J.R. Dahn, *International Journal of Energy Research*, 2010, **34**, 535–555.

54. J. Cabana, L. Monconduit, D. Larcher and M.R. Palacin, *Advanced Materials*, 2010, **22**, 170–191.

55. W.-J. Zhang, *Journal of Power Sources*, 2011, **196**, 13–24.

56. T. Djenizian, I. Hanzu and P. Knauth, *Journal of Materials Chemistry*, 2011, **21**, 9925-9937.

57. G.N. Zhu, Y.G. Wang and Y.Y. Xia, *Energy & Environmental Science*, 2012, **5**, 6652–6667.

58. X. Su, Q.L. Wu, X. Zhan, J. Wu, S. Wei and Z. Guo, *Journal of Materials Science*, 2012, **47**, 2519–2534.

59. T. Berger, D. Monllor-Satoca, M. Jankulovska, T. Lana-Villarreal and R. Gomez, *ChemPhysChem*, 2012, **13**, 2824–2875.

60. T. Froschl, U. Hormann, P. Kubiak, G. Kucerova, M. Pfanzelt, C.K. Weiss, R.J. Behm, N. Husing, U. Kaiser, K. Landfester and M. Wohlfahrt-Mehrens, *Chemical Society Reviews*, 2012, **41**, 5313-5360.

61. Q. Li, N. Mahmood, J. Zhu, Y. Hou and S. Sun, *Nano Today*, 2014, **9**, 668–683.

62. X. Su, Q. Wu, J. Li, X. Xiao, A. Lott, W. Lu, B.W. Sheldon and J. Wu, *Advanced Energy Materials*, 2014, **4**, 1300882.

63. M.R. Zamfir, H.T. Nguyen, E. Moyen, Y.H. Lee and D. Pribat, *Journal of Materials Chemistry A*, 2013, **1**, 9566-9586.

64. C. Erk, T. Brezesinski, H. Sommer, R. Schneider and J. Janek, *ACS Applied Materials & Interfaces*, 2013, **5**, 7299–7307.

65. J. Chen, *Materials*, 2013, **6**, 156–183.

66. A.R. Kamali and D.J. Fray, *Journal of New Materials & Electrochemical Systems*, 2010, **13**, 147–160.

67. T.D. Bogart, A.M. Chockla and B.A. Korgel, *Current Opinion in Chemical Engineering*, 2013, **2**, 286–293.

68. H. Wu and Y. Cui, *Nano Today*, 2012, **7**, 414–429.

69. M. Ge, X. Fang, J. Rong and C. Zhou, *Nanotechnology*, 2013, **24**, 422001.

70. J. Cho, *Journal of Materials Chemistry*, 2010, **20**, 4009–4014.

71. J.R. Szczech and J.R. Jin, *Energy & Environmental Science*, 2011, **4**, 56-72.

72. M. Inagaki, Y. Yang and F. Kang, *Advanced Materials*, 2012, **24**, 2547–2566.

73. L. Yan, Y.B. Zheng, F. Zhao, S. Li, X. Gao, B. Xu, P.S. Weiss and Y. Zhao, *Chemical Society Reviews*, 2012, **41**, 97–114.

74. X.M. Liu, Z.D. Huang, S.Y. Oh, B. Zhang, P.C. Ma, M.M.F. Yuen and J.-K. Kim, *Composites Science and Technology*, 2012, **72**, 121–144.

75. J.N. Tiwari, R.N. Tiwari and K.S. Kim, *Progress in Materials Science*, 2012, **57**, 724–803.

76. L.M. Dai, D.W. Chang, J.B. Baek and W. Lu, *Small*, 2012, **8**, 1130–1166.

77. C. De Las Casas and W.Z. Li, *Journal of Power Sources*, 2012, **208**, 74–85.

78. G. Amatucci and J.M. Tarascon, *Journal of the Electrochemical Society*, 2002, **149**, 31.

79. A.K. Padhi, K.S. Nanjundaswamy and J.B. Goodenough, *Journal of the Electrochemical Society*, 1997, **144**, 1188–1194.

80. C. Delmas and I. Saadoune, *Solid State Ionics*, 1992, **370**, 53–56;

81. M. Morcrette, P. Rozier, L. Dupont, E. Mugnier, L. Sannier, J. Galy and J.M. Tarascon, *Natural Material*, 2003, **2**, 755–761.

82. P. Novak, J.-C. Panitz, F. Joho, M. Lanz, R. Imhof and M. Coluccia, *Journal of Power Sources*, 2000, **90**, 52–58.

83. M. Balasubramanian, X. Sun, X.Q. Yang and J. McBreen, *Journal of Power Sources*, 2001, **92**, 1–8.

84. Y. Teradaa, K. Yasakaa, F. Nishikawab, T. Konishic, M. Yoshiod and I. Nakaia, *Journal of Solid State Chemistry*, 2001, **156**, 286–291.

85. Y.S. Meng, G. Ceder, C.P. Grey, W.-S. Yoon and Y. Shao-Horn, *Electrochemical and Solid-State Letters*, 2004, **7**, 155–158.

86. C.P. Grey, N. Dupré, *Chemical Reviews*, 2004, **104**, 4493–4512.

87. D. Aurbach, B. Markovsky, M.D. Levi, E. Levi, A. Schechter, M. Moshkovich and Y. Cohen, *Journal of Power Sources*, 1999, **95**, 81–82.

88. D. Aurbach, *Journal of Power Sources*, 2000, **89**, 206.

89. E. Peled, D. Golodnitsky and J.Penciner, in *Handbook of Battery Materials*, ed. J.O. Besenhard, Wiley-VCH, Weinheim, NY, Toronto, 1999, ch. 6, pp. 419–453.

90. P.J. Gellings and H.J.M. Bouwmeester, in *CRC Handbook of Solid State Electrochemistry*, CRC Press, New York, 1997.

91. C.B. Choudary, H.S. Maiti, E.C. Subbaro and E.C. Subbarao, in *Solid Electrolytes and their Applications*, Plenum Press, New York, 1980.

92. J.B. Goodenough, *Materials Science Forum*, 1986, **7**, 1.

93. J.L. Souquet, *Annual Review of Materials Research*, 1981, **11**, 211–231.

94. R. Tärneberg and A. Lundn, *Solid State Ionics*, 1996, **90**, 209–220.

95. D.R. Lide and H.P.R. Frederikse, in *CRC Handbook of Chemistry and Physics*, CRC Press, 1994, ch. 5, pp. 93.

96. J.T. Kummer, *Progress in Solid State Chemistry*, 1972, **7**, 141–175.

97. J.E. Bauerle, *Journal of Physics and Chemistry of Solids*, 1969, **30**, 2657–2670.

98. T. van Dijk and A.J. Burggraaf, *Physica Status Solidi A*, 1981, **63**, 229–240.

99. P.G. Bruce and A.R. West, *Journal of the Electrochemical Society*, 1983, **130**, 662–669.

100. J. Fleig and J.A. Maier, *Journal of the Electrochemical Society,* 1998, **145**, 2081–2089.

101. J. Fleig and J. Maier, *Journal of the American Ceramic Society*, 1999, **82**, 3485– 3493.

102. X. Guo and J. Maier, Journal of the Electrochemical Society, 2001, **148**, 121–126.

103. H. Moriwake, X. Gao, A. Kuwabara, C.A.J. Fisher, T. Kimura, Y.H. Ikuhara, K. Kohama, T. Tojigamori and Y. Ikuhara, *Journal of Power Sources,* 2015, **276**, 203–207.

104. H. Chung and B. Kang, *Solid State Ionics*, 2014, **263**, 125–130.

105. S. Yubuchi, S. Teragawa, K. Aso, K. Tadanaga, A. Hayashi and M. Tatsumisago, *Journal of Power Sources*, 2015, **293**, 941–945.

106. S. Adams and J. Swenson, *Physical Review Letters*, 2000, **84**, 4144–4147.

107. J.C. Bachman, S. Muy, A. Grimaud, H.-H. Chang, N. Pour, S.F. Lux, O. Paschos, F. Maglia, S. Lupart, P. Lamp, L. Giordano and Y. Shao-Horn, *Chemical Reviews*, 2016, **116**, 140-162.

108. R. J. Cava and E. A. Rietman, *Physical Review B*, 1984, **30**(12), 6896–6902.

109. J. W. Fergus, *Solid State Ionics*, 2012, **227**, 102-112.

110. J.B. Goodenough, H.Y.P. Hong and J.A. Kafalas, *Materials Research Bulletin*, 1976, **11**, 203–220.

111. R.W. Bonne and J. Schoonman, *Journal of the Electrochemical Society*, 1977, **124**, 28–35.

112. J. Schoonman, G. Oversluizen and K.E.D. Wapenaar, *Solid State Ionics*, 1980, **1**, 211–221.

113. G.-Y. Adachi, N. Imanaka and S. Tamura, *Chemical Reviews*, 2002, **102**, 2405–2430.

114. A.R. West, in *Crystal Chemistry of Some Tetrahedral Oxides*, Zeitschrift für Kristallographie. 1975, **8**, 141, 422.

115. N. Kamaya, K. Homma, Y. Yamakawa, M. Hirayama, R. Kanno and M. Yonemura, *Nature Materials*, 2011, **10**, 682-686.

116. Y.A. Du and N.A.W. Holzwarth, *Physical Reviews B*, 2007, **76**, 174302.

117. R.D. Shannon and B.E. Taylor, *Electrochimica Acta*, 1977, **22**, 783–796.

118. Y.W. Hu, I.D. Raistrick and R.A. Huggins, *Journal of the Electrochemical Society*, 1977, **124**, 1240–1242.

119. H.Y.P. Hong, *Materials Research Bulletin*, 1978, **13**, 117–124.

120. H.-J. Deiseroth, S.-T. Kong, H. Eckert, J. Vannahme, C. Reiner, T. Zaiß and M. Schlosser, *Angewandte Chemie International Edition*, 2008, **47**, 755–758.

121. R.P. Rao and S. Adams, *Physica Status Solidi*, 2011, **208**, 1804–1807.

122. S. Boulineau, M. Courty, J.M. Tarascon and V. Viallet, *Solid State Ionics*, 2012, **221**, 1–5.

123. O. Pecher, S.-T. Kong, T. Goebel, V. Nickel, K. Weichert, C. Reiner, H.-J. Deiseroth, J. Maier, F. Haarmann and D. Zahn, *Chemistry – A European Journal*, 2010, **16**, 8347–8354.

124. H.-J. Deiseroth, J. Maier, K. Weichert, V. Nickel, S.-T. Kong and C. Reiner, *Zeitschrift für anorganische und allgemeine Chemie*, 2011, **637**, 1287–1294.

125. H.-J Deiseroth, Sh.-T. Kong, H. Eckert, J. Vannahme, C. Reiner, T. Zaiß and M. Schlosser, *Angewandte Chemie International Edition*, 2008, **47**, 755 –758.

126. R.P. Rao, N. Sharma, V.K. Peterson and S. Adams, *Solid State Ionics*, 2013, **230**, 72–76.

127. H. Aono, E. Sugimoto, Y. Sadaoka, N. Imanaka and G.-Y. Adachi, *Journal of the Electrochemical Society*, 1993, **140**, 1827–1833.

128. G.F. Ortiz, M.C. Lopéz, P. Lavela,C. Vidal-Abarca and J.L. Tirado, *Solid State Ionics*, 2014, **262**, 573–577.

129. X. Yao, B. Huang, J. Yin, G. Peng, Z. Huang, C. Gao, D. Liu and X. Xu, *Chinese Physics B*, 2016, **25**, 018802.

130. K. Arbi, M. Hoelzel, A. Kuhn, F. García-Alvarado and J. Sanz, *Inorganic Chemistry*, 2013, **52**, 9290–9296.

131. K. Arbi, M. Tabellout, M.G. Lazarraga, J.M. Rojo and J. Sanz, *Physical Reviews B*, 2005, **72**, 094302.

132. M. Cretin and P. Fabry, *Journal of the European Ceramic Society*, 1999, **19**, 2931–2940.

133. P. Knauth, *Solid State Ionics*, 2009, **180**, 911–916.

134. C. Cao, Z.-B. Li, X.-L. Wang, X.-B. Zhao and W.-Q. Han, *Frontiers in Energy Research*, 2014, **2**.

135. P. Hartmann, T. Leichtweiss, M.R. Busche, M. Schneider, M. Reich, J. Sann, P. Adelhelm and J. Janek, *The Journal of Physical Chemistry C*, 2013, **117**, 21064–21074.

136. Z. Xia and A. Meijerink, *Chemical Society Reviews*, 2017, **46**, 275-299.

137. V. Thangadurai, S. Narayanan and D. Pinzaru, *Chemical Society Reviews*, 2014, **43**, 4714–4727.

138. R. Murugan, V. Thangadurai and W. Weppner, *Angewandte Chemie International Edition*, 2007, **46**, 7778–7781.

139. O. Bohnke, C. Bohnke and J.L. Fourquet, *Solid State Ionics*, 1996, **91**, 21–31.

140. S. Stramare, V. Thangadurai and W. Weppner, *Chemistry of Materials*, 2003, **15**, 3974–3990.

141. D. Aurbach and Y.S. Cohen, in Identification of Surface Films on Electrodes in non-Aqueous Electrolyte Solutions: Spectroscopic, Electronic and Morphologic Studies. ed. P.B. Balbuena and Y. Wang, Imperial College Press, London, 2004, pp. 70-139.

142. K. Xu, *Chemical Reviews*, 2004, **104**, 4303-4417.

143. A. Guerfi, A. Vijh and K. Zaghib, in *Safe Lithium re-Chargeable Batteries based on Ionic Liquids*, ed. B. Scrosati, K.M. Abraham, W.V. Schalkwijk and J. Hassoun, Wiley, New York, 2013, pp. 291-326.

144. N.S. Choi, Z. Chen, S.A. Freunberger, X. Ji, Y. Sun, K. Amine, G. Yushin, L.F. Nazar, J. Cho and P.G. Bruce, *Angewandte Chemie International Edition*, 2012, **51**, 9994–10024.

145. A. Unemoto, M. Matsuo and S. Orimo, *Advanced Functional Materials*, 2014, **24**, 2267-2279.

146. S.I. Orimo, Y. Nakamori, J.R. Eliseo, A. Züttel and C.M. Jensen, *Chemical Reviews*, 2007, **107**, 4111- 4132.

147. H.J. Schlesinger and H.C. Brown, *Journal of the American Chemical Society*, 1940, **62**, 3429–3435.

148. M. Matsuo, A. Remhof, P. Martelli, R. Caputo, M. Ernst, Y. Miura, T. Sato, H. Oguchi, H. Maekawa, H. Takamura, A. Borgschulte, A. Züttel and S. Orimo, *Journal of the American Chemical Society*, 2009, **131**, 16389-16391.

149. M. Matsuo, T. Sato, Y. Miura, H. Oguchi, Y. Zhou, H. Maekawa, H. Takamura and S. Orimo, *Chemistry of Materials*, 2010, **22**, 2702-2704.

150. H. Oguchi, M. Matsuo, T. Sato, H. Takamura, H. Maekawa, H. Kuwano and S. Orimo, *Journal of Applied Physics*, 2010, **107**, 1-3.

151. T. Sato, K. Ikeda, H. W. Li, H. Yukawa, M. Morinaga and S. Orimo, *Materials Transactions*, 2009, **50**, 182-186.

152. M.B. Ley, D.B. Ravnsbaek, Y. Filinchuk, Y.S. Lee, R. Janot, Y.W. Cho, J. Skibsted and T.R. Jensen, *Chemistry of Materials*, 2012, **24**, 1654-1663.

153. M.B. Ley, S. Boulineau, R. Janot, Y. Filinchuk and T.R. Jensen, *The Journal of Physical Chemistry C*, 2012, **116**, 21267-21276.

154. N. Kamaya, K. Homma, Y. Yamakawa, M. Hirayama, R. Kanno, M. Yonemura, T. Kamiyama, Y. Kato, S. Hama, K. Kawamoto and A. Mitsui, *Nature Materials*, 2011, **10**, 682-686.

155. M. Matsuo, S. Kuromoto, T. Sato, H. Oguchi, H. Takamura and S. Orimo, *Applied Physics Letters*, 2012, **100**, 1-4.

156. T.J. Udovic, M. Matsuo, A. Unemoto, N. Verdal, V. Stavila, A.V. Skripov, J.J. Rush, H. Takamura and S. Orimo, *Chemical Communications*, 2014, **50**, 3750-3752.

157. L. He, H.-W. Li, H. Nakajima, N. Tumanov, Y. Filinchuk, S.-J. Hwang, M. Sharma, H. Hagemann and E. Akiba, *Chemistry of Materials*, 2015, **27**, 5483-5486.

158. N. Verdal, J.H. Her, V. Stavila, A.V. Soloninin, O.A. Babanova, A.V. Skripov, T.J. Udovic and J.J. Rush, *Journal of Solid State Chemistry*, 2014, **212**, 81-91.

159. H. Wu, W.S. Tang, V. Stavila, W. Zhou, J.J. Rush and T.J. Udovic, *Journal of Physical Chemistry C*, 2015, **119**, 6481-6487.

160. T.J. Udovic, M. Matsuo, W.S. Tang, H. Wu, V. Stavila, A.V. Soloninin, R.V. Skoryunov, O.A. Babanova, A.V. Skripov, J.J. Rush, A. Unemoto, H. Takamura and S. Orimo, *Advanced Materials*, 2014, **26**, 7622-7626.

161. I. Cascallana-Matias, PhD thesis, University of Glasgow, 2016.

162. K. Yamada, K. Kumano and T. Okuda, *Solid State Ionics.*, 2006, **177**, 1691-1695.

163. H. Maekawa, M. Matsuo, H. Takamura, M. Ando, Y. Noda, T. Karahashi and S. Orimo, *Journal of the American Chemical Society*, 2009, **131**, 894-895.99.

164. N. Bernstein, M. D. Johannes and K. Hoang, *Physical Review B*, 2013, **88**, 5.

165. J.S.G. Myrdal, D. Sveinbjornsson and T. Vegge, *ECS Meeting Abstracts*, MA2011-2002 Sec. B2019, abstract No. 2756.

166. M. Matsuo, A. Remhof, P. Martelli, R. Caputo, M. Ernst, Y. Miura, T. Sato, H. Oguchi, H.Maekawa, H. Takamura, A. Borgschulte, A. Züttel and S. Orimo, *Journal of the American Chemical Society*, 2009, **131**, 16389-16391.

167. M. Matsuo, H. Oguchi, T. Sato, H. Takamura, E. Tsuchida, T. Ikeshoji and S. Orimo, *Journal of Alloys and Compounds*, 2013, **580**, 98-101.

168. D.B. Ravnsbaek, M.B. Ley, Y.S. Lee, H. Hagemann, V. D'Anna, Y.W. Cho, Y. Filinchuk and T.R. Jensen, *International Journal of Hydrogen Energy*, 2012, **37**, 8428-8438.

169. M.B. Ley, D.B. Ravnsbaek, Y. Filinchuk, Y.S. Lee, R. Janot, Y.W. Cho, J. Skibsted and T.R. Jensen, *Chemistry of Materials*, 2012, **24**, 1654-1663.

170. M. Matsuo, Y. Nakamori, S. Orimo, H. Maekawa and H. Takamura, *Applied Physics Letters*, 2007, **91**, 1-3.

171. L.H. Rude, O. Zavorotynska, L.M. Arnbjerg, D.B. Ravnsbaek, R.A. Malmkjaer, H. Grove, B.C. Hauback, M. Baricco, Y. Filinchuk, F. Besenbacher and T.R. Jensen, *International Journal of Hydrogen Energy*, 2011, **36**, 15664-15672.

172. Y. Wang, W.D. Richards, S.P.Ong, L.J. Miara, J.C. Kim, Y. Mo and G. Ceder, *Nature Materials*, 2015, **14**, 1026-1031.

173. S.P. Ong, Y. Mo, W. Davidson Richards, L. Miara, H. Sug Lee and G. Ceder, *Energy & Environmental Science*, 2013, **6**, 148–156.

V. Thangadurai, S. Narayanan and D. Pinzaru, *Chemical Society Reviews*, 2014, **43**, 4714.

2. Methods & Techniques

In this chapter, the methods and techniques, used for the preparation, synthesis and characterisation of the samples discussed in this thesis, are presented in detail.

For the synthesis of the investigated compounds, mechanochemical processing and thermal treatments were used. For structural and determination and phase analysis Powder X-ray Diffraction (PXD) was used as the main technique, while Raman spectroscopy was applied for further structural analysis. Simultaneous Thermal Analysis was used to determine the phase transitions and chemical reactions occurring during the synthesis process and to confirm the thermal stability of the produced compounds. Evolved gas analysis by Mass Spectrometry was also performed as a function of temperature. Finally, Electrochemical Impedance Spectroscopy (EIS) was applied for the electrochemical characterisation of the materials in order to determine ionic conductivity and activation energies for Li^+ ion diffusion.

2.1 Sample Preparation

2.1.1 Air-sensitive handling techniques

Both the raw materials used, and the final compounds synthesised during the reported experiments were air- and moisture-sensitive. For this reason, all the manipulations were carried out under an inert (argon) atmosphere, inside a glove box.

Inert-atmosphere glove boxes provide researchers with the ability to directly handle air- and moisture-sensitive solids and liquids. A basic setup consists of a gas tight box fitted with a viewing window, a pair of gloves and a gas tight transfer port. The working area in the box is filled and flushed with inert gas [1] and the items were transferred in and out through the transfer port; first, the air is removed from the port and the items transferred inside under vacuum and then the port is again filled with argon/nitrogen in order to be safely opened from the inside working area.

For this project, an MBraun LABstar glove box was used. This model consists of a stand, two antechambers, a rotary vane vacuum pump and an atmosphere sensor, monitoring the oxygen and moisture levels. A single-column, inert gas purification system, automated and regenerable, is in operation. The system works continuously to keep the oxygen and moisture levels below 1 ppm, each.

2.2 Synthesis

The synthesis process of the target materials consists of two steps:
1. mechanochemical processing of the solid reactants,
2. thermal treatment of the milled materials.

2.2.1 Mechanochemical Processing – High Energy Ball milling [2]

Mechanochemical processing (MCP) can be defined as “a powder processing technique involving deformation, fracturing and cold welding of the particles during repeated collisions with a ball during high-energy milling” [2]. Typically, milling is used to reduce powder size and can also induce structural changes. In some cases, during mechanochemical processes, mechanical energy can also activate chemical reactions. In such cases, after the breaking of chemical bonds, MCP engages the particles into an out-of-equilibrium state, under the action of cyclic loading.

Particle’s relaxation time is the time required for a particle to adjust or "relax" its velocity to a new condition of forces. It's an indication of the particle's ability to quickly adjust to a new environment or condition and depends on the mass and mechanical mobility of the particle without being affected by the external forces acting on the particle. Particles’ relaxation time during high energy ball milling, suggests a faster departure from equilibrium when compared to other far-from-equilibrium processes, such as rapid solidification [3].

The relaxation time, τ, can be obtained using the following equation:

$$\boldsymbol{\tau = \frac{\rho_p d_p^2 C_c}{18n}} \qquad [2.1]$$

where ρ_p is the particle mass density (g·cm^{-2}), d_p is the particle diameter (μm), C_c is the Cunningham slip correction faction (dimensionless) and n is the molecular density (molecules/cm^{-3})

Because relaxation time is proportional to the square of particle diameter, it increases rapidly with the increase of particle size. Usually, small particles "relax" to new environments (i.e. following the flow well) in a very short time, while larger particles are more "stubborn" and tend to stick to their original path.

The mechanism of particle failure -the way the particles are de-formed before reaching a new state- depends on the particle size and the structure of the particles undergoing milling. A change in the energy relaxation results in a dramatic increase in the strain and an extreme dislocation flow follows. In the case where several components undergo ball/powder particle collisions, the relaxation occurs by mechanical alloying, decomposition or synthesis of a new chemical compound. The materials' properties (crystal structure, particle surface properties etc.) and the stress conditions in the milling device (e.g. magnitude and direction of acting forces) directly affect and determine the changes and deformations of the solids, thus could lead to crystallisation and stabilisation of new compounds [2].

A mechanochemically-activated mixture of powders -like the ones milled during this project- could form numerous reaction couples, which would increase with decreasing particle size and regenerate through repeated particle fracture and welding events. The reaction product phase would not separate the reactants as continuous product phase removal does not take place during ball/powder particles collisions. A lack of a diffusion barrier in the reacting couples as well as the formation of various defects provides fast diffusion paths can overcome the problem of diffusion acting as the rate-controlling process. Consequently, the reaction can proceed with acceptable kinetics, with no raise of the reaction temperature. Therefore, several chemical or alloying reactions, normally not possible at ambient temperature, could occur at ambient temperature during MCP or they could be easily completed following further thermal treatment if necessary [2].

Ball milling (BM) is one of the most commonly used mechanochemical methods. The working principle of the method is that grinding of materials can be achieved by developing high energies via centrifugal and/or planetary action (*Figure 2.1-a*). There are different types of grinding media (tungsten carbide, zirconium oxide, polyamide plastic, etc.) which are selected according to the type of materials being milled, with the main concern having to do with a *non-reaction relation* between the materials being milled and the material of the grinding media.

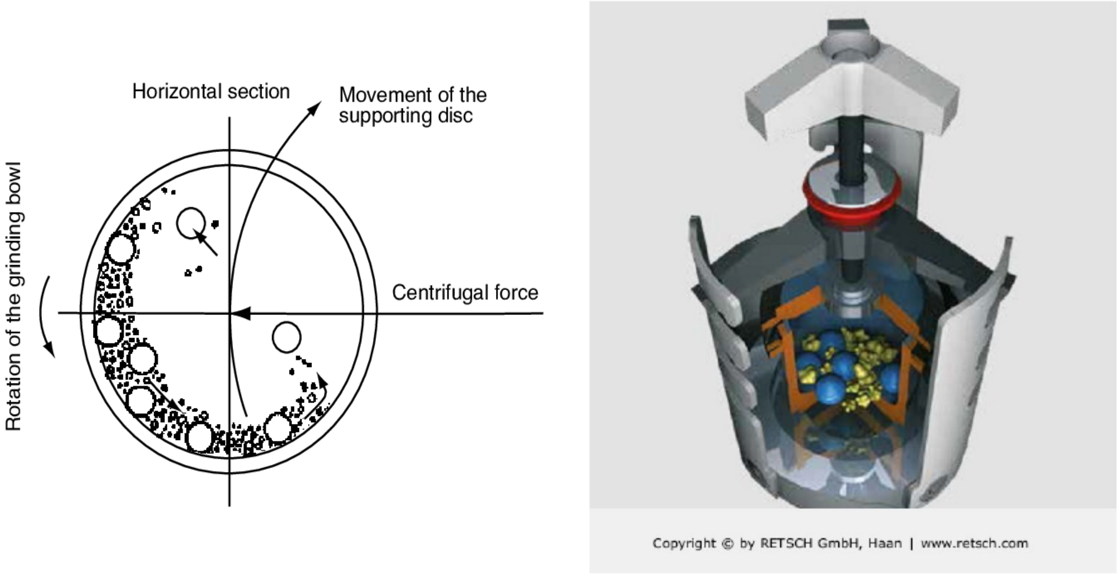

Copyright © by RETSCH GmbH, Haan | www.retsch.com

Figure 2. 1: **(a)** Schematic representation of the working principle of ball milling method, **(b)** Schematic representation of the Retsch PM100 ball mill used in current work's experiments.

For this project, the Retsch PM100 ball mill (*Figure 2.1-b*) was used for the mechanochemical processing of the materials. Details for the grinding media and experimental parameters are presented in Chapter 3.

2.2.2 Thermal treatment

Thermal treatment is proposed to be beneficial for the stabilization of the high-pressure phase of LiBH4 at room temperature [4]. Conventional thermal treatment was employed either to complete the unfinished reaction from ball milling or to improve the crystallinity of the final compounds. For that reason, all the mechanosynthesis's products presented in this work were heated after being milled. The thermal treatment of the samples took place in a vertical, pot-oven, under argon atmosphere. The heating temperatures varied in the range between 100 – 200 °*C* while, the heating experiments ran for 1 – 4 *h*.

2.3 Structural determination and characterisation techniques

2.3.1 Powder X-ray diffraction

The discovery of X-rays by W.C. Röntgen in 1895 led to the development of three new scientific fields: X-ray radiography, X-ray crystallography and X-ray spectrometry [5]. X-ray diffractometry, from the very beginning, has been used as a tool for many different purposes; from complex chemical analysis to the study of phase equilibria [6]. One of its most common uses is in the investigation of crystal structure. X-rays are short-wavelength and high-energy beams of electromagnetic radiation [5]. They arise when matter is irradiated with a beam of high-energy charged particles or photons. Continuous radiation is produced from the rearrangement of the electrons of the target element where each rearrangement corresponds to a different type of emitted radiation.

In powder diffractometry, the most commonly used radiation is the K_α radiation emission from copper, arising when an electron is transferred from the *L* shell to *K* ($K^+ \longrightarrow L^+$) and the excess energy is emitted as *K* X-rays (*Figure* 2.2). The copper *K* spectrum consists of two pairs of lines; the K_{α_1}, K_{α_2} doublet occurring from 2p ⟶ 1s transitions (K_α emission characteristic, weighted, average wavelength of 1.5418 *Å*); and the K_{β_1}, K_{β_2} doublet occurring from 3p ⟶ 1s transitions. Usually, the ß doublet is reduced or removed using a filter (usually a nickel foil for Cu radiation) and the α_1 (or α_2) lines are then selected using a crystal monochromator.

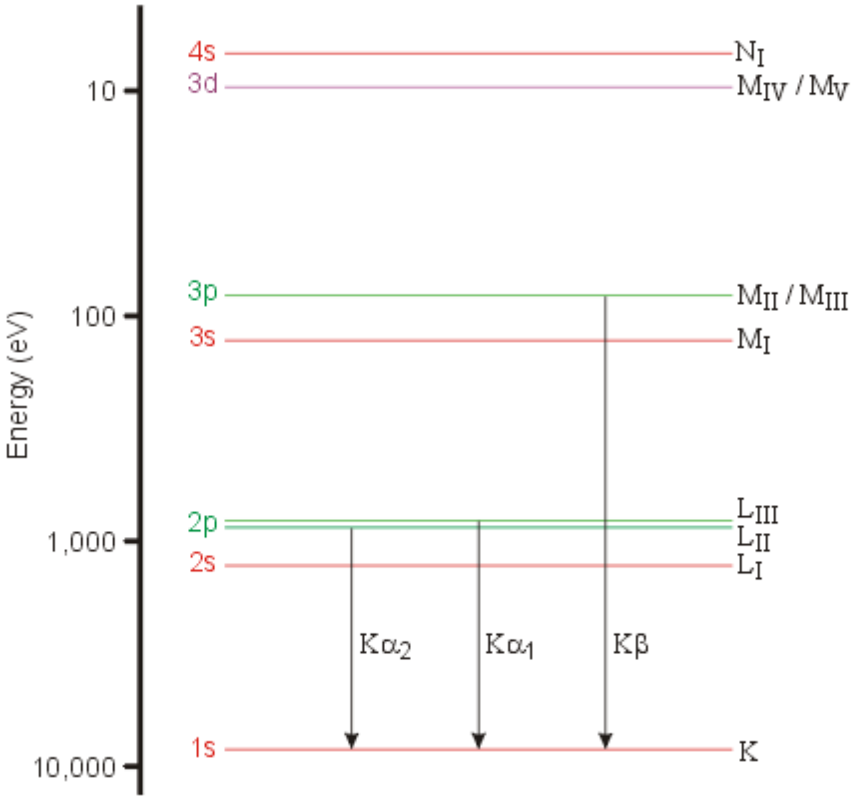

Figure 2. 2: Diagram of the electronic energy levels for a copper atom: The characteristic lines in this type of spectrum are called K, L, M etc., and they correspond to transitions to orbitals with principal quantum numbers 1, 2, 3 etc.

A crystal can diffract a monochromatic wave in various directions in space. In 1913, W. L. Bragg stated that diffraction is a scattering phenomenon and explained that it is only possible when the rays scattered from certain planes of atoms in a crystal, exhibit constructive interference. Assuming that crystals are built up of layers or planes, some of the X-rays are diffracted off a plane with the angle of reflection equal to the angle of incidence, but the rest are transmitted to be subsequently reflected by succeeding planes. In case the number of wavelength of two random incident beams is integral, nλ, the Bragg's condition is satisfied, and the diffracted beams are in phase, interfering constructively.

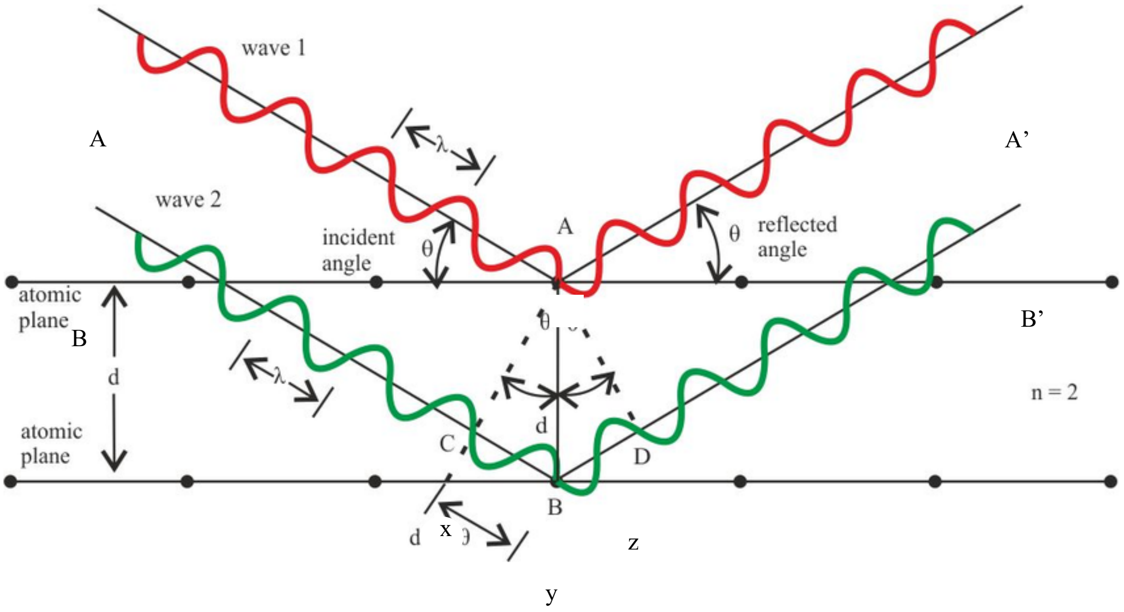

Figure 2. 3: "Bragg Diffraction"; A and B indicate the incident X-ray beams with a striking angle θ. Scattered X-rays are indicated by A' and B'. The lattice spacing is denoted by d.

The derivation of Bragg's law is depicted in Figure 2.3.

"Two incident X-ray beams strike in different planes of regular arrays of atoms, atomic planes, which are described with Miller indices, hkl. Beam BB' has to travel an extra distance xyz as compared to beam AA', and for A' and B' to be in phase, distance xyz must be equal to a whole number of wavelengths, nλ. The perpendicular distance, the d-spacing and the angle of incidence, or Bragg angle, θ, are related to the distance xy by [7]

$$\mathbf{xy} = \mathbf{yz} = \boldsymbol{d}_{\mathbf{hkl}}\mathbf{sin}\boldsymbol{\theta} \qquad [2.1]$$

$$\mathbf{xyz} = \mathbf{2}\boldsymbol{d}_{\mathbf{hkl}}\mathbf{sin}\boldsymbol{\theta} \qquad [2.2]$$

$$\mathbf{xyz} = \mathbf{n}\boldsymbol{\lambda} \qquad [2.3]$$

The Bragg's condition is mathematically expressed by Equation 2.4, known as the *"Bragg's law"*, which involves combining Equations 2.2 and 2.3.

$$\mathbf{2}\boldsymbol{d}_{\mathbf{hkl}}\mathbf{sin}\boldsymbol{\theta} = \mathbf{n}\boldsymbol{\lambda} \qquad [2.4]$$

where θ is the scattering angle, n is a positive integer and λ is the wavelength of the incident beam. The measurement of the intensity of the scattered waves as a function of the scattering angle provides characteristic patterns for crystalline materials.

Atoms arranged in three dimensions form crystals. Each crystal is defined by the smallest atom formation repeating itself by translation to form the final structure, known as the crystal's *unit cell*. As shown in Figure 2.4, three distances (a, b, c) and three angles (α, β, γ) define each unit cell.

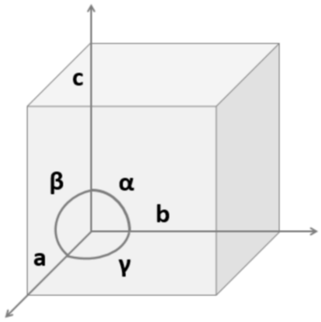

Figure 2. 4: 3D representation of a cubic unit cell

Seven independent unit cell shapes are possible to form in three- dimensional crystals structures. Each one of these unit cell formations has a unique volume formula dictated by its geometry. Depending on the crystal system, a different relation between the lattice spacing and the cell parameters can be calculated. Tables 2.1 – 2.3 sum up all this information for each one of the *seven crystal systems*.

In each type of unit cell, different permitted positions are available for the atoms or ions to occupy. These positions are also known as *lattice points*. Each lattice point represents an equivalent environment. Such points in a crystal, make up an array which can represent the way the atoms, ions or molecules are repeated in the structure. this array is called *lattice*. Based on the allowed lattice point positions, each 3D unit cell can be characterised by one or more of the following four structural types: the *primitive* unit cell (P), with lattice points allowed only at the corners; the *body-centred* unit cell (I), with lattice points at the corners and one at the centre of the cell; the *face- centred* unit cell (F), with lattice points at the corners and one in the centre of each face. The face-centred unit cell (A, B, or C) has a lattice point at each corner, and one in the centres of one pair of opposite faces (*e.g.* an A-centred cell has lattice points in the centred of the *bc* faces) **[8]**.

The combination of a crystal systems and a lattice types gives the *Bravais lattice* of the structure. That way, 14 different Bravais lattices are possible. As presented in the International Tables for Crystallography **[9]**, 32 point-groups can describe all the possible non-translational symmetries (reflection, rotation etc.) and 230 3D space groups can be derived from the combination of the above 32 point groups with the 14 Bravais lattices. These 230 groups are calculated after taking into consideration translational symmetries alongside the non-translational ones.

The specific unit cell volumes for each crystal system derives from the formulae presented in Table 2.2 **[10]**. The relationships between lattice spacings and cell parameters for each crystal system are shown in Table 2.3.

Crystal System	Unit cell Parameters	Symmetry	Possible Lattices
Cubic	$a = b = c$ $\alpha = \beta = \gamma = 90^{o}$	Four three-fold axes	P, F, I
Tetragonal	$a = b \neq c$ $\alpha = \beta = \gamma = 90^{o}$	One four-fold axis	P, I
Orthorhombic	$a \neq b \neq c$ $\alpha = \beta = 90^{o}, \gamma = 120^{o}$	Three two-fold axes or mirror planes	P, F, I, A, (B or C)
Hexagonal	$a = b \neq c$ $\alpha = \beta = 90^{o}, \gamma = 120^{o}$	One six-fold axis	P
Trigonal	$a = b \neq c$ $\alpha = \beta = 90^{o}, \gamma = 120^{o}$	One three-fold axis	P
	$a = b = c$ $\alpha = \beta = \gamma \neq 90^{o}$	One three-fold axis	R
Monoclinic	$a \neq b \neq c$ $\alpha = \gamma = 90^{o}, \beta \neq 90^{o}$	One two-fold axis or mirror plane	P, C
Triclinic	$a \neq b \neq c$ $\alpha \neq \beta \neq \gamma \neq 90^{o}$	None	P

Table 2. 1: The seven crystal systems.

[P: Primitive, F: Face centred, C (or A, B): Side centred, I: Body centred].

Unit Cell	Volume Calculation Formula
Cubic	$V = a^3$
Tetragonal	$V = a^2c$
Orthorhombic	$V = abc$
Hexagonal	$V = \frac{\sqrt{3}a^2c}{2} = 0.866a^2c$
Monoclinic	$V = abc \cdot sin\beta$
z	$V = abc(1 - cos^2a - cos^2\beta - cos^2\gamma + 2 \cdot cosa \cdot cos\beta \cdot cos\gamma)^{1/2}$

Table 2. 2: Formula for the calculation of unit cell volume.

Unit Cell	Lattice Spacing Calculation Formula
Cubic	$\frac{1}{{d_{hkl}}^2} = \frac{h^2 + k^2 + l^2}{a^2}$
Tetragonal	$\frac{1}{{d_{hkl}}^2} = \frac{h^2 + k^2 + l^2}{a^2} + \frac{l^2}{c^2}$
Orthorhombic	$\frac{1}{{d_{hkl}}^2} = \frac{h^2}{a^2} + \frac{k^2}{b^2} + \frac{l^2}{c^2}$
Hexagonal	$\frac{1}{{d_{hkl}}^2} = \frac{4}{3}\left(\frac{h^2 + hk + k^2}{a^2}\right) + \frac{l^2}{c^2}$
Monoclinic	$\frac{1}{{d_{hkl}}^2} = \frac{1}{sin^2\beta}\left(\frac{h^2}{a^2} + \frac{k^2 + sin^2\beta}{b^2} + \frac{l^2}{c^2} - \frac{2hlcos\beta}{ac}\right)$
Triclinic	$\frac{1}{{d_{hkl}}^2} = \frac{1}{V^2}\left[\begin{matrix} h^2b^2c^2sin^2a + k^2a^2c^2sin^2\beta + l^2a^2b^2sin^2\gamma \\ + 2hkabc^2\,(cosa \cdot cos\beta - cos\gamma) \\ + 2kla^2bc\,(cos\beta \cdot cos\gamma - cos\alpha) \\ + 2hlab^2c\,(cosa \cdot cos\gamma - cos\beta) \end{matrix}\right]$

Table 2. 3: Formula relating lattice spacings to cell parameters for each crystal system.

Powder X-ray diffraction experiments provide information varying from phase purity to crystal structures. For example, assigning crystal phases to observed reflections leads to the successful indexing of the structures under investigation and determination of a unit cell, while information for the position and intensity of peaks can allow a structural model to be deduced.

In this work, powder X-ray diffraction experiments were mainly conducted with a *Bruker D8 Advance* powder diffractometer, in transmission geometry, with spinning sealed sample capillaries, operating with Cu K_a radiation (Debye-Scherrer geometry). X- rays were generated as a beam of high-energy electrons (provided by a tungsten filament) is accelerated towards an anode by a potential difference of 40 k*V*, with a current of 40 m*A*. A filter (Si(111)) removes the K_B radiation of ~1.39222 Å, letting through only the desired K_a radiation of ~1.54184 Å as the most intense characteristic line. The resulting monochromatic beam of X-rays interacts with the sample and the diffracted rays are collected by a VANTEC PSD 1 detector. Data are usually collected in a range of $15° \leq 2\theta \leq 70°$, with a = 0.017 step size and scan times of 15 *h* for good-quality patterns.

A *PANalytical X'Pert Pro* diffractometer was also used for the characterisation of some of the samples in this work. While most of the technical characteristics of this machine are similar to the Bruker D8, there is no primary optic and a nickel (Ni) foil is used to remove the Cu K_B radiation (0.02 m*m*; K_B = 1.392250 Å). Also, the X'Celerator detector system of the X'Pert machine allows data collection times significantly shorter than the Bruker D8. Therefore, 20 *min* scans were run to retrieve high quality patterns. The scan parameters reported above for the D8 scans were also applied with this machine.

Sample preparation for X-ray analysis using both machines was performed inside the glove box because of the air and moisture sensitive nature of the materials. For D8 experiments, the samples were loaded into capillaries (0.5 m*m* thick and 30 m*m* long), which were initially sealed with wax to prevent oxygen or moisture contamination for transfer outside the glove box. They were subsequently flame-sealed. In the cases where the X'Pert machine was used, the samples were mounted on flat plates/holders inside a glove box and transferred to the machine inside an airtight sample holder.

2.3.2 Raman Spectroscopy

Raman spectroscopy is one of the three most important vibrational spectroscopy techniques, close to mid-infrared (IR) and near-IR spectroscopies. Vibrational spectroscopy can be used for both qualitative and quantitative analysis of a wide range of substances. Raman spectroscopy is focused on the elucidation of molecular structure, by the measurement of molecular vibrational modes. The technique is based on the interaction of electromagnetic radiation with the molecular vibrations of the sample, thus, providing information on the vibrational state of molecules [11].

To better understand the vibrations under investigation, it would be useful to consider the classical mechanics' model of a diatomic molecule consisting of two masses (m_1 and m_2) connected by a massless spring. If the displacement of each mass is X_1 and X_2, for a harmonic oscillator, it varies periodically as a sine (or cosine) function (*Figure 2.5*)

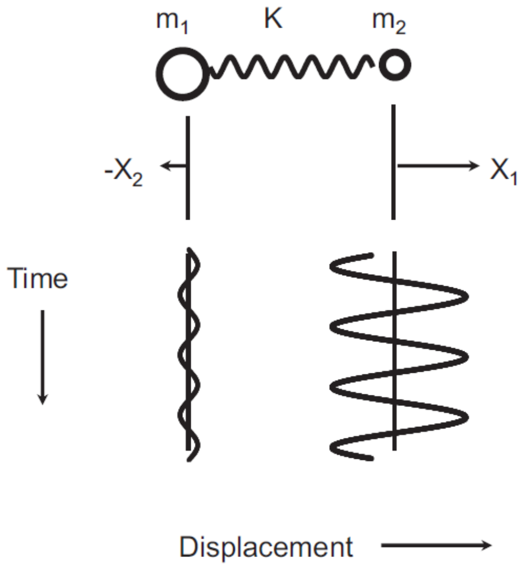

Figure 2. 5: Classical harmonic oscillator description of a simple diatomic molecule. The spring constant is K, the masses are m1 and m2, and X1 and X2 are the displacement vectors of each mass from equilibrium [11].

Such oscillating dipoles, urged by an incident waves, produce electromagnetic radiation leading to scattering phenomena. Most typically, in a Raman experiment, the sample is irradiated with monochromatic radiation induced from a laser, leading to elastically scattered Rayleigh light and Raman-scattered photons [11].

As the incident electromagnetic field perturbs the charged particles of the sample's molecules leads to an induced "dipole moment", described by Equation 2.5:

$$\boldsymbol{\mu} = \boldsymbol{\alpha E} \qquad [2.5]$$

where, α is the polarisability, E is the incident electric field and, μ is the induced dipole moment. The result of the dipole's moment, μ, oscillation at a frequency ν_0 (*Figure 2.6-a*), and the polarisability's, α, slightly varying magnitude at the much slower molecular vibrational frequency ν_m (*Figure 2.6-b*), is presented in Figure 2.6-c, which presents an amplitude modulation of the dipole moment oscillation of the molecule. This type of modulated wave can be resolved mathematically into three steady amplitude components with frequencies $\nu_0 + \nu_m$, and $\nu_0 - \nu_m$, as shown in Figure 2.6-d.

In general, the wavenumber ($\tilde{\nu}_R$) is proportional to the incident frequency (ν) and inversely proportional to the wavelength (λ) (*Equation 2.6*):

$$\boldsymbol{\tilde{\nu}_R} = {}^{(\boldsymbol{\nu})}/_{\boldsymbol{c}} = {}^{\boldsymbol{1}}/_{\boldsymbol{\lambda}} \qquad [2.6]$$

where, c is the speed of light in vacuum.

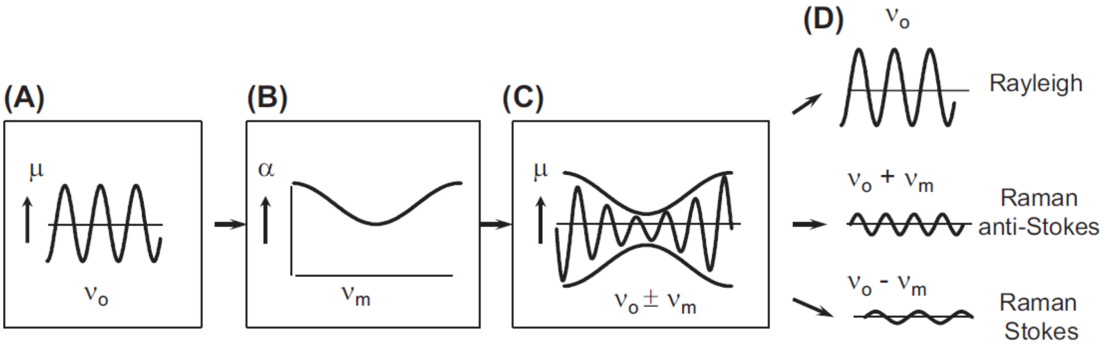

Figure 2. 6: Schematic representing Rayleigh and Raman scattering. (A) the incident radiation makes the induced dipole moment of the molecule oscillate at the photon frequency, (B) the molecular vibration can change the polarizability, a, which changes the amplitude of the dipole moment oscillation, (C) the resulted amplitude modulated dipole moment oscillation, (D) the components with steady amplitudes, which can emit electromagnetic radiation [11].

The Raman lines will appear at a certain wavenumber ($\tilde{\nu}_R$), which is the result of the difference between the frequency of the active vibration mode (ν) and the laser used (ν_0), normalised with respect to c (*Equation 2.7*).

$$\tilde{\boldsymbol{\nu}}_{\boldsymbol{R}} = {}^{(\boldsymbol{\nu} - \boldsymbol{\nu}_0)}/_{\boldsymbol{c}} \qquad [2.7]$$

According to the Maxwell-Boltzman distribution, at room temperature most atoms will reside in the lowest vibrational state; thus, the possibility that Stokes scattering occurs is greater than that for anti-Stokes scattering. Stokes Raman scattering is due to the fact that the material absorbs energy and the emitted photon has a lower energy than the incident photon. In the case of anti-Stokes scattering, on the other hand, the material loses energy and the emitted photon has a higher energy than the absorbed photon. The difference in intensity of the Stokes and anti-Stokes components is due to the different number of molecules in each state initially. For the less widely spaced rotational levels, the Stokes and anti-Stokes scattering are of similar magnitude. For the vibrational levels, which are spaced further apart, the anti-Stokes signal is significantly weaker than the Stokes signal. The disparity is also reduced with increased temperature, and the difference can be used as a measure of temperature.

In order to better understand the vibrational modes of molecules we should consider the degrees of freedom which describe each mode. Vibrational spectroscopy probes the degrees of vibrational freedom (*Equation 2.8 – 2.9*). Cartesian axes considered, a molecule has *3N* degrees of freedom, each one corresponding to the translational, vibrational and rotational motion of each molecule. In general, non-linear molecules with N atoms have 3*N* – 6 normal modes of vibration (*Equation 2.8*), whereas a linear molecule has 3*N* – 5 normal modes of vibration (*Equation* 2.9), with the rotation around its molecular axis not observed.

$$\textit{non linear molecule} = 3N - 6 \qquad [2.8]$$

$$\textit{linear molecule} = 3N - 5 \qquad [2.9]$$

Considering a “free” borohydride anion, as a tetrahedral molecule, presents a total of 9 (*3N* – 6) vibrational modes. These are the; $\boldsymbol{\nu_1}$, symmetric stretch (singly-degenerate symmetry mode, *A*), $\boldsymbol{\nu_2}$, symmetric bend (doubly-degenerate symmetry mode, *E*), $\boldsymbol{\nu_3}$, asymmetric stretch (triply-degenerate symmetry mode, T_2) and $\boldsymbol{\nu_4}$, asymmetric bend (triply-degenerate symmetry mode, T_2) (*Figure 2.6*). In a crystal structure, the symmetry of each borohydride ion will also depend on the site symmetry, which, in turn, will determine the symmetry of the bond vibrations [12][13].

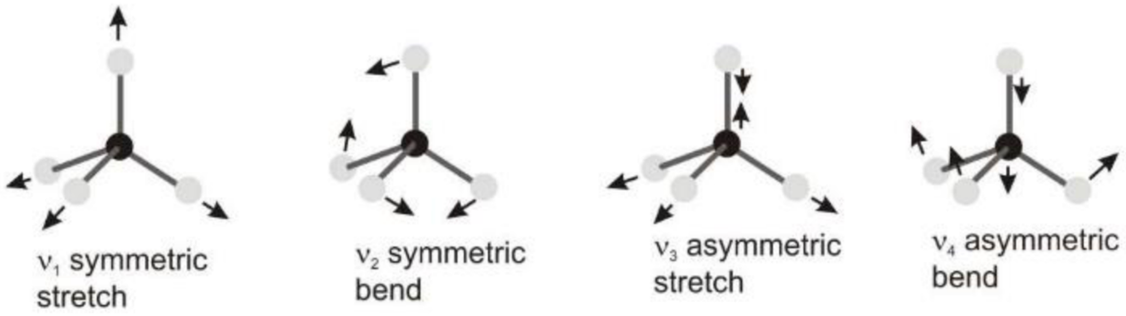

Figure 2. 7: Vibrational modes of a tetrahedral molecule [12].

In low temperature (LT–) $LiBH_4$, the borohydride ions have point group symmetry C_s, as they are located at a mirror plane. The total representation of the ion’s translational, rotational and vibrational modes, also known as *reducible representation* (Γ_{3N}), can, then, be recognised as $\Gamma_{3N} = 15E + 3\sigma_h$ and is calculated to be $\Gamma_{3N} = 9A' + 6A''$ (based on the character table). Therefore, for a borohydride with C_s lattice points' group, the symmetries of the vibrational modes become; $\nu_1 = A'$, $\nu_2 = A' + A''$, $\nu_3 = 2A' + A''$, $\nu_4 = 2A' + A''$.[13] In this case, the modes will be "Raman active", when quadratic terms (x^2, y^2, z^2,xy, yz, xz) can be assigned according to the point group.

All Raman experiments were conducted using a *Horiba-Jobin-Yvon LabRam HR* confocal microscope using a 532 n*m* laser, equipped with a 50x objective lens and a *Synapse CCD* detector. Hole apertures were of 200 μ*m* and 25% laser intensity was used. The samples were placed in capillaries due to their air-sensitive nature.

2.3.3 Thermal analysis

Thermal analysis, in the field of solid-state chemistry, is commonly performed for the investigation of solid-state reactions, thermal decomposition and phase transitions. It comprises a group of analytical techniques which are used for the measurement of a sample's physical properties as a function of temperature, while the material under investigation is exposed to a controlled temperature programme.

Differential thermal analysis (DTA) is a thermal analysis technique during which, both a sample and an inert reference material are subjected to the same heat treatments and, the temperature difference between the two of them is measured. The temperature difference is, afterwards, plotted against time or temperature allowing heat absorption or evolution to be deducted relatively to the inert reference.

DTA systems are often used in combination with thermogravimetric analysis (TGA) systems, because of their ability to provide both mass loss and enthalpy-related information. The technique is used for the investigation of the changes in the physical and chemical properties of materials. Measurements are usually performed either as a function of temperature at constant heating rate, and/or as a function of time by considering the mass loss. Physical phenomena, such as second-order phase transitions, vaporization or desorption and chemical phenomena such as decomposition can thus be investigated [14].

In this work experiments were conducted using a *NETZSCH STA 409 PC* analyser, coupled with a *HIDEN HPR-20* mass spectrometer. Following the ionisation of the evolved gases under high vacuum, the mass spectrometer accelerates the ionised species towards a quadrupole analyser. The analyser's function is to conduct these ions with a particular mass to charge ratio (m/z) to the detector, via alterations to the electro-magnetic field. The spectrometer can both scan within a range of 0 – 300 amu and monitor individual ions, with ${}^{m}/_{z}$ values of interest. The technique was used to study the thermal stability of materials produced to monitor solid-state reactions in situ. Weight loss is observed during the evolution of a certain gas or mixtures of gases.

In a typical experiment, between 5 and 10 mg of sample was loaded in an alumina pan and heated from room temperature to 450 $°C$, at a rate of 5 $°C\cdot min^{-1}$. The analyser was located inside a glove box, under a controlled atmosphere (MBraun, UNILAB, levels of O_2 and $H_2O < 0.1$ ppm). All gas releases during the reaction were monitored in real time (typically N_2, NH_3, H_2, B_2H_6, $B_3H_6N_3$) [15][16].

2.4 References

1. D.F. Shriver and M.A. Drezdzon, in *The manipulation of air-sensitive compounds*, John Wiley & Sons, New Jersey, 2nd edn, 1986, ch. 2, pp. 45-47.
2. M. Sopicka-Lizer, in *High-Energy Ball Milling: Mechanochemical Processing of Nanopowders*, ed. L.C. Yang, Q.T. Qu, Y. Shi and Y.P. Wu, Woodhead Publishing Limited, Cambridge, 1st edn, 2010, ch. 15, pp. 361–408.
3. K. Meyer and W. Meier, *Kristal und Technik*, 1968, **3**, 399.
4. I. Cascallana-Matias, PhD thesis, University of Glasgow, 2016.
5. R. Jenkins and R.L. Snyder, in *Introduction to X-ray Powder Diffractometry*, Wiley-Interscience, New Jersey, 1st edn, 1996, ch. 1, pp. 1-22.
6. B.D. Cullity, in *Elements of X-ray Diffraction*, ed. M. Cohen, Addison-Wesley Publishing Company Inc., Massachusetts, 2nd edn, 1978, ch. 1, pp. 3-29.
7. C. Hammond, in *The basics of crystallography and diffraction*, Oxford University Press Inc, Oxford, 1997.
8. A.R. West, in *Solid State Chemistry and its Applications*, John Wiley & Sons Ltd., Chichester, 2nd edn, 2014, ch. 1, pp. 11-14.
9. T. Hahn, in *International Tables for Crystallography: Volume A Space group symmetry*, Springer Netherlands, 2nd edn, 2006.
10. M.T. Weller, in *Inorganic Materials Chemistry*, Oxford University Press Inc., Oxford, 2004.
11. P.J Larkin, in *Infrared and Raman Spectroscopy: Principles and Spectral Interpretation*, Elsevier Inc., New York, 2nd edn, 2018, ch. 2, pp. 7-28.
12. S. Gomes, H. Hagemann and K. Yvon, *J. Alloy. Compd.*, 2002, **346**, 206-210.
13. E.A. Nickel, PhD thesis, University of Oxford, 2010.
14. S. Vyazovkin, N. Koga and C. Schick, in *Handbook of Thermal Analysis and Calorimetry*, ed. R. Parameshwaran, A. Sari, N. Jalaiah and R. Karunakaran, Elsevier B.V., New York, 1st edn, 2018, ch. 13, pp. 519-572.
15. E.L. Charsley and S.B. Warrington, in *Thermal Analysis: Techniques & Applications*, The Royal Society of Chemistry, Cambridge, 1992, pp. 17-31 & 84-108.

16. F.W. Fifield and D. Kealey, in *Principles and Practice of Analytical Chemistry*, Blackwell Science Ltd., 2000, pp. 428-429.

3. Towards the stabilisation of the fast-ionic and high-pressure phase of $LiBH_4$

3.1 A brief review of $LiBH_4$ studies

Researchers' interest into the properties of lithium borohydride ($LiBH_4$) first arose due to indications that it could function as a promising hydrogen storage material [1][2].

Complex hydrides can release significant amounts of H_2 when in contact with water, that is why they are characterised as "one-pass" hydrogen-storage systems. Sodium, lithium and beryllium are the lightest elements that can form such solid-state compounds with hydrogen, and $LiBH_4$ is one example. It has been shown that $LiBH_4$ presents a significant gravimetric hydrogen density of 18 wt%, however, there are many challenges in synthesising and stabilising it due to the kinetic and thermodynamic limitations that govern the hydrogen storage mechanisms of complex hydrides [3].

The first successful synthesis of pure lithium-borohydride is attributed to Schlesinger and Brown, back in 1940, by the reaction of ethyl-lithium (C_2H_5Li) with diborane (B_2H_6) [4]. After thorough thermal studies, three major endothermic effects were observed, each of them accompanied by decomposition and gas evolution. It was established that the main hydrogen evolution takes place at 653 *K* and liberates 80% of the hydrogen in $LiBH_4$. However, decomposition and thus hydrogen release, is not complete until 765 *K* and proceeds over several different steps [5].

According to *Züttel et al.* [1] the decomposition reaction of $LiBH_4$ can be schematically described in steps as follows (*Equations 3.1 -3.3*):

1. Structural transition at $T = 381.8\,K$:

$$\boldsymbol{LiBH_4 \rightarrow LiBH_{4-\varepsilon} + \frac{1}{2}(\varepsilon)H_2} \qquad [3.1]$$

2. first hydrogen peak starting at $T = 473\,K$:

$$\boldsymbol{LiBH_{4-\varepsilon}} \rightarrow \mathrm{LiBH_2} + \boldsymbol{\frac{1}{2}(1-\varepsilon)H_2} \qquad [3.2]$$

3. Second hydrogen peak starting at $T = 726\,K$:

$$\boldsymbol{LiBH_2 \rightarrow LiH + B + \frac{1}{2}H_2} \qquad [3.3]$$

Following its extensive study as a hydrogen storage material, $LiBH_4$ has drawn interest as a potential electrolyte for solid-state batteries. This was proposed following the discovery that $LiBH_4$ undergoes a structural transition from its orthorhombic, low temperature (LT-) phase to a hexagonal, high temperature (HT-) phase at 380 *K*. Permittivity measurements suggested that the structural transition was, also, accompanied by a transition in conductivity status, as the LT-phase transited into a conductive HT-phase **[6]**. Recently, the stabilisation of the HT-phase of $LiBH_4$ by halide (iodide) substitution at RT was reported by *Orimo et al.* **[6]** for the first time. According to further studies conducted by our group later on, the stabilised via similar process compound presented fast, ionic conductivity values of ca. 10^{-6} $S{\cdot}cm^{-1}$ at 313 *K*, approximately two orders of magnitude higher than the conductivity values demonstrated by the orthorhombic, LT-phase of $LiBH_4$ **[7]**.

Some of the most recent studies, however, are focused on the synthesis and stabilisation, at RT, of the high pressure (HP-) phases of $LiBH_4$. Due to limitations in experimental processes, the discussion and progress upon the existence of highly conductive, HP-phases was leaded by questionable and -what proved to be-incorrect assumptions and conclusions **[8]-[11]**. It was only in 2002, that synchrotron radiation studies confirmed the existence of the different high-pressure structures of $LiBH_4$ for the first time.

In total, lithium-borohydride presents four different phases and structures. At room temperature, $LiBH_4$ forms the LT-phase and crystallises with an orthorhombic structure [*Pnma*, a = 7.190(0) Å, b = 4.444(7) Å, c = 6.813(2) Å, *V* = 217.73 Å^3], exhibiting an ionic conductivity of ~10^{-8} *S*·cm^{-1} (*Figure 3.1-a*)
A phase transition to the hexagonal structure and HT-phase occurs at 382 *K* [*P63mc*, a = 4.268(3) Å, *c* = 6.931(8) Å, *V* = 109.37 Å^3], exhibiting an increased conductivity of 10^{-3} - 10^{-2} *S*·cm^{-1} around this temperature (*Figure 3.1-b*). This fast, ion conducting phase can be stabilised at RT, by partial substitution of $BH_4{}^-$ by I^- or Br^-, as mentioned previously [7][12][13].

According to *Soulie et al.* [17], in the LT-, orthorhombic structure each $BH_4{}^-$ ion is surrounded by four Li^+ and each Li^+ by four $BH_4{}^-$, both in tetrahedral configurations (*Figure 3.2-a*). During the transition from the RT, orthorhombic to the HT-, hexagonal phase, the structure contracts along the orthorhombic *a* (hexagonal *c*) axis and expands in the orthorhombic *b x c* plane (hexagonal basal plane).

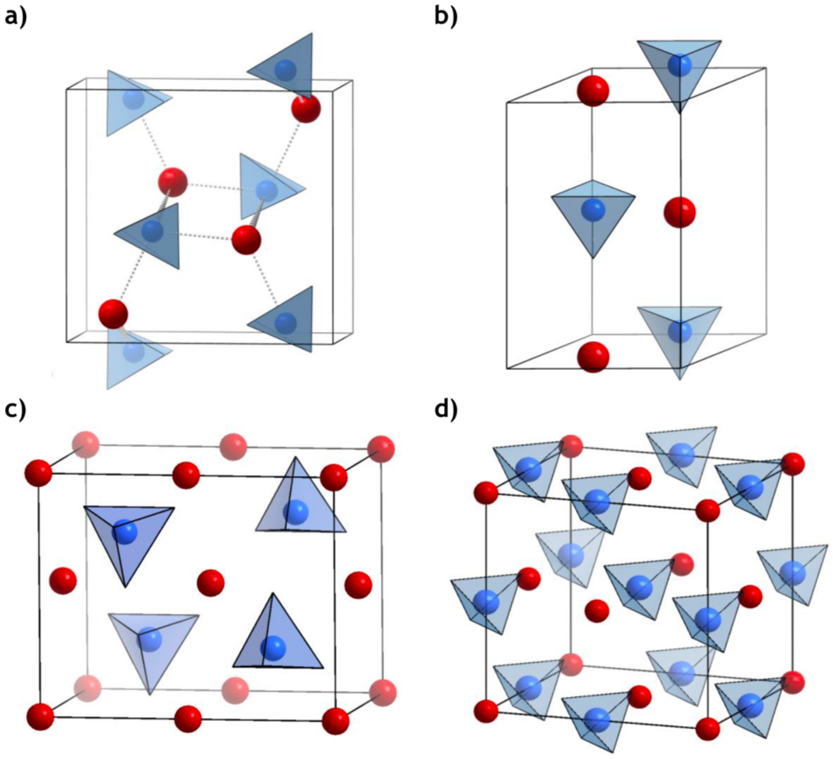

Figure 3. 1: Known phases of $LiBH_4$. Orthorhombic [Pnma], (b) Hexagonal [P*6*3mc], (c) Tetragonal [Ama2] and (d) Cubic [Fm$\bar{3}$m]. (Li^+ ions are shown in red and $BH_4{}^-$ in blue tetrahedra) [7].

At ambient temperature (AT) and "low pressure" (LP) (~1.2 G*Pa*), $LiBH_4$ undergoes another phase transition to a pseudo-tetragonal phase [*Ama*2, a = 6.449(4) Å, b = 5.307(0) Å, c = 5.291(9) Å, *V* = 181.13 Å^3] (*Figure 3.1-c*) **[14][15][16][20]**. This phase can be considered as an orthorhombically distorted antistructure of PtS, where Li^+ ions are tetrahedrally coordinated by BH_4^- anions while the BH_4^- anions adopt a totally new, nearly square-planar coordination to four Li^+ ions (*Figure 3.1-c*).

The last known phase transition of $LiBH_4$ starts above 10 G*Pa*. Under these conditions, $LiBH_4$ forms the cubic, HP- phase (*Figure 3.1-d*), intensely under investigation, nowadays, due to the indications that this phase exhibits high, ionic conductivity. This structure presents a distorted arrangement of BH_4 anions **[18][19]** [$Fm\bar{3}m$, a = 5.109(0) Å, *V* = 133.35 Å^3], at 18.1 G*Pa* [20].

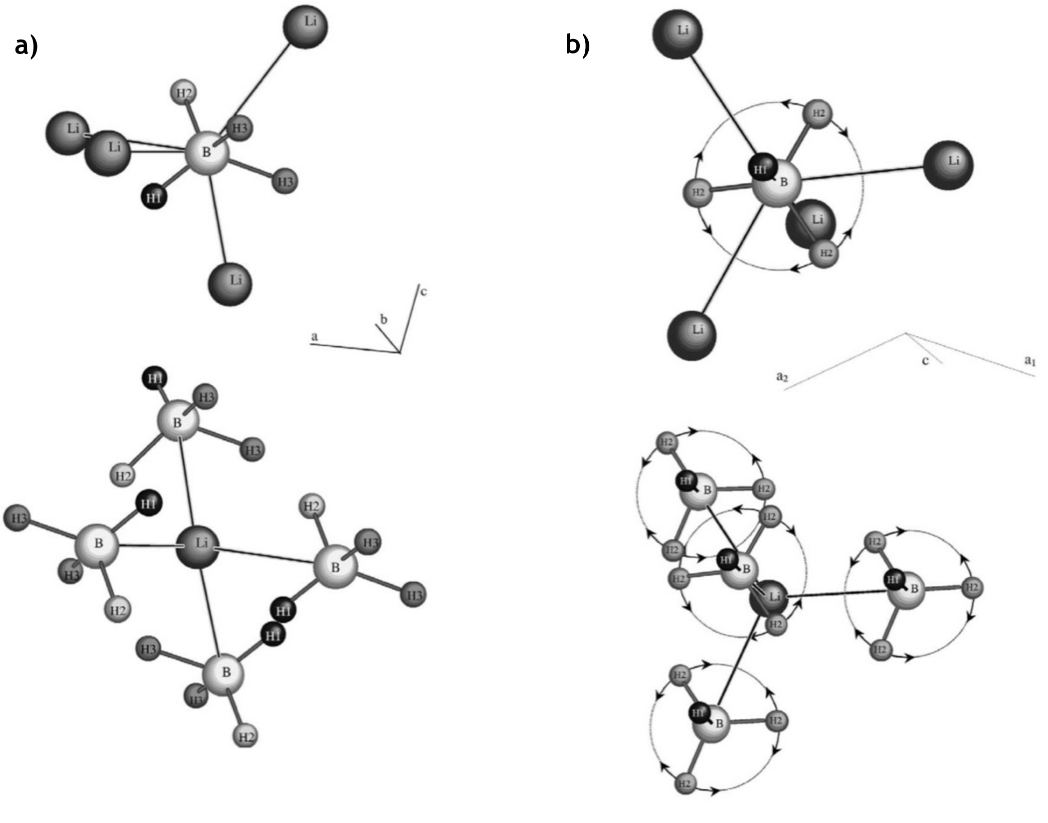

Figure 3. 2: Boron (top) and lithium (bottom) coordination in (a) RT, orthorhombic $LiBH_4$ and, (b) HT-, hexagonal $LiBH_4$ (arrows indicate rotational displacements of the BH_4^- tetrahedra about their trigonal axis) [17].

The AT-/LP- and HP- phases coexist up to at least 18 G*Pa*. In order for the transition to HP-$LiBH_4$ to be completed the AT-/LP- phase needs to be heated to 500 *K*, at approximately 10 G*Pa* [20][21].

Takamura *et al*. measured the ionic conductivity of the last two phases. Based on the fact that HP-$LiBH_4$ forms a rock-salt crystal structure similar to that of *α*-LiI, it was predicted to be similarly ionically conducting. Conductivity measurements confirmed that the AT-/LP- and HP-$LiBH_4$ had a total ionic conductivity of $1.3 \cdot 10^{-4}$ $S \cdot cm^{-1}$ and $7.6 \cdot 10^{-4}$ $S \cdot cm^{-1}$, under ca. 4 G*Pa*, at 453 *K* and 493 *K*, respectively [22].

The phase diagram of $LiBH_4$ is presented in Figure 3.3.

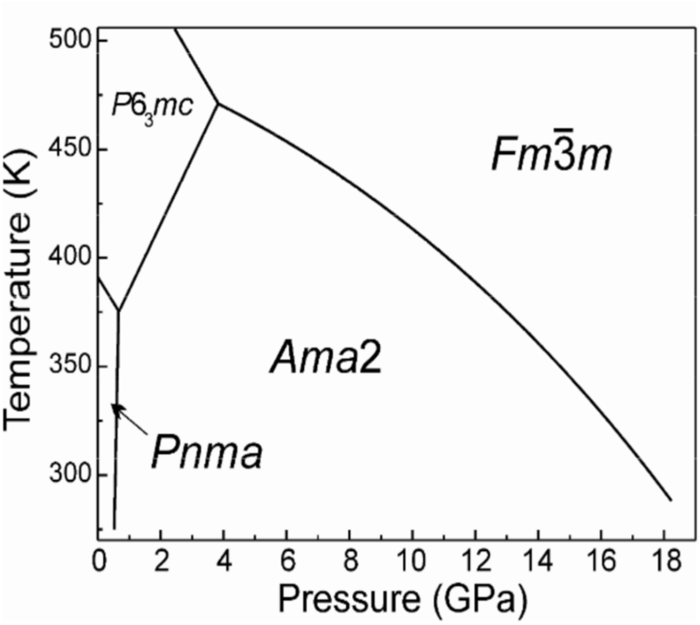

Figure 3. 3: Pressure-Temperature phase diagram of LiBH4 [20].

The conductivity measurements presented above were promising; however, high temperatures and pressures must be applied in order to obtain the desired compound. Normalising the conditions required in order to obtain the HP-phase of

$LiBH_4$ is, today, one of the biggest challenges. Therefore, researchers aspire to develop processes through which the HP-$LiBH_4$ structure will be stabilised at RT, while demonstrating enhanced conductivity.

3.2 Project Aim

Elaborating on previous reported efforts, this project focused on the stabilisation of the HP-phase of $LiBH_4$ at RT. Our efforts were directed to the investigation of the most simple and efficient way to synthesise, stabilise and characterise the fast ion-conducting, HP-phase of $LiBH_4$.

As mentioned earlier in this chapter, anion substitution in LT-$LiBH_4$ can lead to an enhancement in conductivity of up to three order of magnitude. Replacing $[BH_4]^-$ with the larger iodide anion, $[I]^-$, has proved to be the most beneficial for the conductive properties of the compound **[12]**. It has been proposed that cations larger than Li^+ could improve the conductivity by forming complex borohydrides, with a general formula of $Li_{1-x}A_xBH_4$, where A = Na^+ or K^+ **[23]-[28]**.

The first case of anion substitution in $LiBH_4$ complex was reported in 2006 for a mixture of $LiBH_4$-$LiCl$ **[38]**. At 120 ^0C the diffracted intensity of $LiCl$ decreased with an increase in the diffracted intensity of $LiBH_4$. This observation suggested that solid $LiCl$ could be successfully incorporated in the structure of hexagonal, HT-phase of $LiBH_4$. This behaviour was not normally expected to take place due to the significant structural differences of the two compounds. Rietveld refinement was used for an in-depth investigation of this system. The results suggested that the unit cell volume of the orthorhombic, LT-phase of $LiBH_4$ increases due to thermal expansion until the phase transition to the hexagonal, HT-phase is completed **[39]**.

As a result of their studies of the $LiBH_4$-LiX ($X = I, Cl$) system, *Orimo et al.* **[12][40]-[41]** they confirmed the RT stabilisation of the HT-phase of $LiBH_4$ via LiI doping. The expansion of the crystal structure's lattice volume with LiI addition from

$LiBH_4$ (Z = 2, V = 110 $Å^3$) and LiI (Z = 4, V = 218.79 $Å^3$) was reported, suggesting formation of a $LiBH_4$-LiI solid compound. In these samples, the conductivity presented a jump (compared to the one of pure $LiBH_4$) at 115 ^0C, accompanied with a crystal structure transition from orthorhombic to hexagonal, reaching a conductivity value of 10^{-2} $S{\cdot}cm^{-1}$, above 170 ^0C.

In 2011 *Rude et al.* [42] conducted studies of anion substitution facilitated by thermal treatment. Ball-milled samples of $LiBH_4$-LiI were annealed at 280 ^0C for 96 *h*. The PXD data collected at RT revealed a single-phase compound of $Li(BH_4)_{0.73}I_{0.27}$ (iodide content of 27 %). This study showed that this anion substitution product remained stable at RT for a year while, it was suggested that substitution of iodide anions in lithium borohydride provides a more solid stabilisation of its HT-phase.

Up to that point, the HT-phase of $LiBH_4$ has never been isolated at RT as a single-phase compound obtained as a result of Br^- incorporation. This was achieved by our group's previous work [7] which reported that $Li(BH_4)_{1-x}Br_x$ compounds can be obtained by either extensive mechanically milling of $LiBH_4$ and $LiBr$ or by a short ball milling period followed by thermal treatment. The obtained mixed borohydrides presented conductivities of ca. 10^{-6} $S{\cdot}cm^{-1}$ at 313 *K* (two orders of magnitude higher compared to the orthorhombic, LT-phase of $LiBH_4$).

After Orimo's [12] and our group's [7] reported results, Bernstein *et al.* proposed that stabilisation of the HT-polymorph of $LiBH_4$ could be achieved with $NaBH_4$ or KBH_4 [23]. The idea was based on the fact that, during the halide/anion substitution in $LiBH_4$ improved ionic conductivity via the expansion of the crystal structure, due to the successful incorporation of the bigger halide (iodide) ions. Drawing inspiration from this explanation, Bernstein *et al.* showed that the crystal structure could be similarly expanded via the incorporation of larger cations (eg. Na^+ or K^+).

Based on Bernstein's *et al.* [23] suggestion and our group's earlier studies [7], our hypothesis was that stabilising the cubic, HP-phase of $LiBH_4$ at RT, would be possible by forming a solid solution with isostructural, cubic $NaBH_4$, by substituting Na for Li in LT-$LiBH_4$. That way, the tetrahedrally coordinated Li-sites could be stabilised in a bigger-volume cell, potentially creating more wide bottlenecks and, thus, migration/conduction paths. However, this time, the transition to a bigger, cubic cell would be achieved by cation-, rather than anion, substitution.

3.3 Results & Discussion

Following the stabilisation of the HT-phase at RT, attempts have been made to synthesise sodium-substituted lithium borohydride but, previous work has suggested that a direct reaction between $LiBH_4$ and $NaBH_4$ is not possible.[32] However, as evidenced by both the work in our group presented earlier [7] and our results, by mechanochemical synthesis, combined cation- and anion-doping provides a promising path to the stabilisation of the HP-phase of $LiBH_4$ at RT.

The proposed method includes the mechanochemical processing and annealing of $LiBH_4$ – LiI- $NaBH_4$ mixtures. Structure determination from PXD results indicates the formation of a single-phase material with the general formula $Li_{(1-y)}Na_y(BH_4)_{(1-z-zy)}X'_{z(1-y)}$, with rock salt structure analogous to HP-$LiBH_4$.

For the synthesis, all the precursor materials were used as purchased, with no further processing. They are presented in the list that follows.

- Lithium Borohydride ($LiBH_4$): powder, ≥95%, Sigma-Aldrich, MW = 21.78, air- sensitive, reacts violently with water
- Sodium Borohydride ($NaBH_4$): powder, ≥98%, Sigma-Aldrich, MW = 37.83, air- sensitive, reacts violently with water
- Lithium Iodide (LiI): beads, 99.9%, Sigma-Aldrich, MW = 133.85

The target materials were synthesised by mechanochemical processing of the precursor materials, followed by thermal treatment. Two different synthesis approaches were followed; a “three-steps” and a “two-step” synthesis process. The experimental parameters and conditions applied during each of these experiments will be discussed below.

For each experiment, the precursor materials were loaded into stainless-steel ball milling jars, sealed inside an argon glove box and transferred to a Retsch PM100 ball mill. After ball milling, the samples were transferred to silica tubes, inside the glove box, and sealed with a rubber septum to maintain an argon atmosphere during the annealing process. After transferring to the furnace, syringes connected to plastic pipes were used as gas inlet and outlet to each one of the silica tubes in order to minimise the risk of moisture or/and air exposure of the samples.

The results of three different experiment types are presented; two experiments following the first synthesis approach (EA001 & EA002) and one following the second synthesis approach (EA003). Experiments EA001 and EA002 were designed on the basis of the group's previous work [32], in order to confirm the successful synthesis of HP-$LiBH_4$ materials and to propose any modifications to the experimental design. Experiment EA003 adopted a different and simpler "one-step synthesis" approach and its experimental parameters and conditions are described in Section 3.3.2.

3.3.1 Approach 1: "Two-step synthesis"

The first approach consisted of two steps.

The first step was the development of halide-doped borohydride precursors. Based on our group's previous work [32] and in order to overcome the challenge of the non-direct reaction between $LiBH_4$ and $NaBH_4$, we re-produced the synthesis of hexagonal, HT-phase precursors, via ball milling of $LiBH_4$ and LiI.

Moving on, once the halide was successfully incorporated in $LiBH_4$ to form $Li(BH_4)_{(1-y)}X_y$, the obtained halide-doped precursors were reacted with $NaBH_4$ to partially form the desired, cubic complex hydride by ball milling.

In order for the reaction to be completed, the ball milled mixture underwent a thermal treatment to form the polycrystalline, HP-hydride product with the general chemical formula $Li_{(1-y)}Na_y(BH_4)_{(1-z-zy)}X'_{z(1-y)}$.

The “two-step” synthesis process can be described by equations 3.1 and 3.2.

Step 1: $$(1-z)LiBH_4 + zLiX \rightarrow Li(BH_4)_{(1-z)}X_z$$ ***[Eq. 3.1]***

Step 2: $$(1-y)Li(BH_4)_{(1-z)}X_z + yNaBH_4 \rightarrow$$

$$\rightarrow Li_{(1-y)}Na_y(BH_4)_{(1-z+yz)}X_{z(1-y)}$$ ***[Eq. 3.2]***

To simplify the experimental design and decrease the number of the dependent variables, the molar amount of the reactants in Equation 3.2 and the ratio of the cations were fixed throughout the experiments. Thus, the only compositional variable was the molar quantity of the reactants in Equation 3.1 and, as a result, the molar ratio of the anions $(BH_4)^-$ and X^-.

3.3.1.1 Experiment - EA001

For experiment EA001 and its first step, ~0.4 *g* of the precursor mixture LiBH4 - LiI were mechanically milled by applying a milling speed of 500 *rpm*, for 4 *h*, following a pattern of 2 *min* milling / 2 *min* breaks to avoid over-heating of the materials. The previously milled precursor sample was further milled after the addition of a stoichiometric amount of $NaBH_4$, for 24 *h*, by applying a milling speed of 500 *rpm* and following the same pattern of 2 *min* milling / 2 *min* breaks to avoid over-heating of the materials.

Detailed information on the experimental ratios, quantities and chemical systems, for experiment EA001, are shown in Table 3.1. The stainless-steel jar was loaded with 6 stainless-steel balls (*d* = 10 m*m*), for each experimental step. Due to the air-sensitive nature of the materials, all the manipulations were performed under an argon atmosphere inside a glove box.

Following the mechanochemical treatment the sample was heated to 200 ^0C, for 2 *h*, according to the procedure described in Section 3.3.

Experiment - EA001					
Samples	**Reactants**	**Molar Ratio**	**Moles**	**Mass (*g*)**	**Duration (*h*)**
	Step 1: $2LiBH_4 + LiX \rightarrow 3Li(BH_4)_{0.67}I_{0.33}$				
a	$LiBH_4$	2	$4.59 \cdot 10^{-3}$	0.1	4
	LiI	1	$2.30 \cdot 10^{-3}$	0.308	
	Step 2: $Li(BH_4)_{0.67}I_{0.33} + NaBH_4 \rightarrow 2Li_{0.5}Na_{0.5}(BH_4)_{0.81}I_{0.19}$				
b	$Li(BH_4)_{0.67}I_{0.33}$	1	$6.09 \cdot 10^{-3}$	0.358	24
	$NaBH_4$	1	$6.09 \cdot 10^{-3}$	0.23	
	Step 3: Annealing of $Li_{0.5}Na_{0.5}(BH_4)_{0.81}I_{0.19}$				
c	$Li_{0.5}Na_{0.5}(BH_4)_{0.81}I_{0.19}$	-	-	~ 0.2	2
d	$Li_{0.5}Na_{0.5}(BH_4)_{0.81}I_{0.19}$	-	-	~ 0.2	4

Table 3. 1: Experimental parameters and conditions of experiment type EA001.

The powder X-ray diffraction (PXD) data taken after each of the above stages of the synthesis are shown in Figures 3.4-3.6.

The X-ray pattern from the $Li(BH_4)_{0.67}I_{0.33}$ precursor formed during the first step of the experimental process (EA001-a) is shown in Figure 3.4. All peaks could be assigned to the hexagonal, HT-structure of $LiBH_4$ (V = 102.96(6) Å^3), in good agreement with the group's previously reported data (V = 103.17(1) Å^3) **[32]**.

After milling, PXD shows that the sample EA001-b contains a rock-salt phase that could be identified as partially formed $Li_{0.5}Na_{0.5}(BH_4)_{0.81}I_{0.19}$ (*Figure 3.5*). The strongest peaks in the pattern can be matched to the HP-type phase (a = 5.109(2), V = 133.35 Å^3) whereas weaker reflections could be identified as a phase with the LT-$LiBH_4$ structure (a = 7.130(2), b = 4.3978(12), c = 6.806(2), V = 213.41 Å^3).

The formation of a single phase was observed after thermal treatment at 200 ^0C, for 2 *h* (EA001-c). The X-ray pattern of the synthesised compound is shown in Figure 3.6 and the reflections can be assigned to the "rock-salt" HP-$LiBH_4$

structure of normal composition 50% Li^+ / 50% Na^+, 81% BH_4^- / 19% I. The $Li_{0.5}Na_{0.5}(BH_4)_{0.81}I_{0.19}$ compound was indexed as a cubic structure (Figure 3.6).

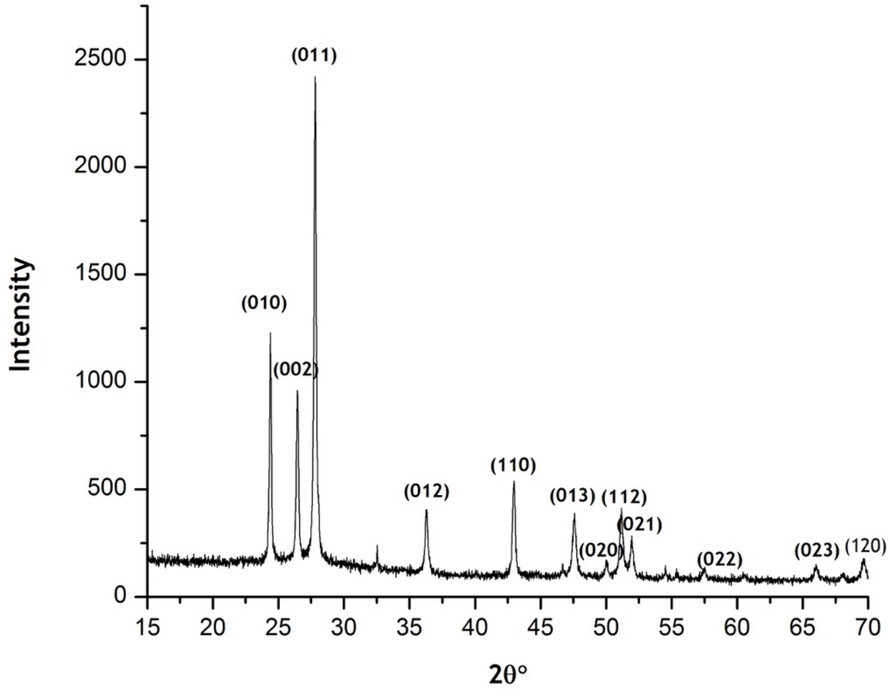

Figure 3. 4: PXD pattern of sample EA001-a. Synthesis of the precursor $Li(BH_4)_{0.67}I_{0.33}$ by mechanochemical processing, for 4 *h*, at 500 *rpm*. All peaks can be assigned to the hexagonal, HT- polymorph of $LiBH_4$.

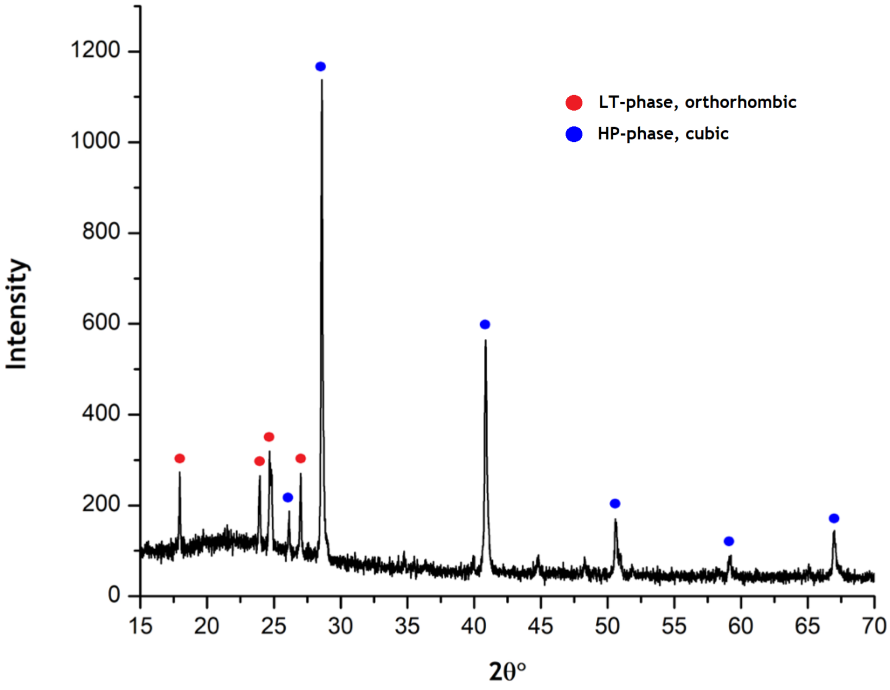

Figure 3. 5: PXD pattern of sample EA001-b. Partial synthesis of the $Li_{0.5}Na_{0.5}(BH_4)_{0.81}I_{0.19}$ compound by mechanochemical processing, for 24 *h*, at 500 *rpm*. The peaks were allocated to two different phases, proposing a mixture of the HP-$LiBH_4$ (blue dots) and the LT- $LiBH_4$ (red dots).

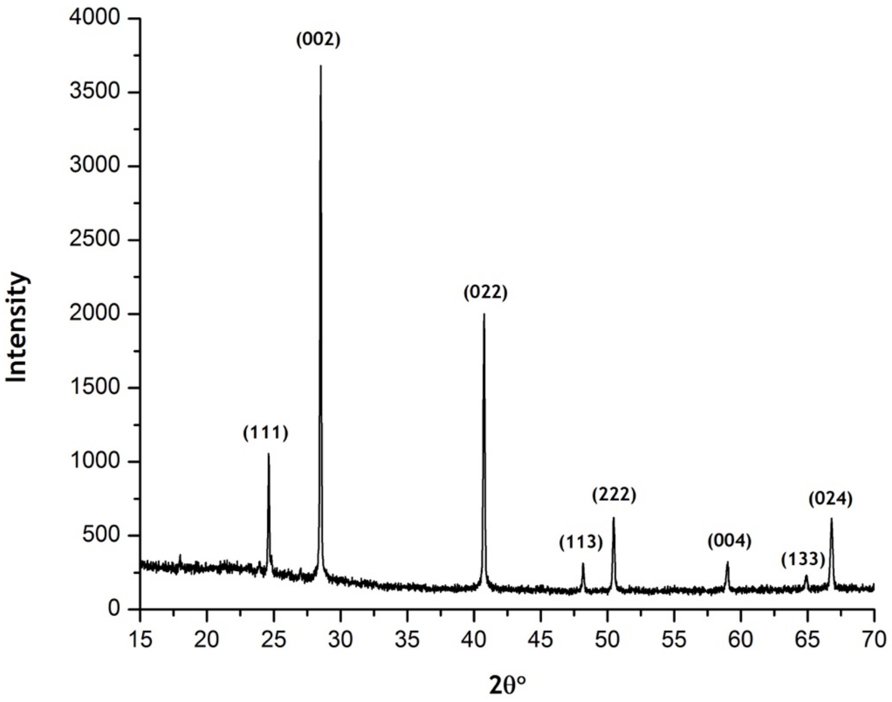

Figure 3. 6: PXD pattern of sample EA001-c. Completed synthesis of the nominal $Li_{0.5}Na_{0.5}(BH_4)_{0.81}I_{0.19}$ compound after thermal treatment of sample EA001-b at 200 ^0C, for 2 *h*. The peaks were fitted with the cubic, HP- polymorph of $LiBH_4$.

Rietveld structural refinement was performed for the above sample. X-ray diffraction data were refined by the GSAS crystallography data analysis software. During the analysis, the interdependent and simultaneous refined of the Li+/Na+ and B-/I- was used as the only constraint. The linear interpolation function was applied for background refinement. 100 cycles were run for each refinement. The same refinements details were used for all data refined throughout this work.

X-ray powder diffraction data collected indicated the formation of a single, cubic phase [$Fm\overline{3}m$, a = 6.260(9) Å, *V* = 245.42 Å^3]. The plot produced from the refinement is shown in Figure 3.7.

Diffraction evidence thus suggested that the HP-$LiBH_4$ phase could indeed be stabilised in a mixed metal borohydride, at RT, via iodide substitution at a level of 17%.

The background was successfully modelled using linear interpolation. The peak shape was modelled using a pseudo-Voigt function. The site occupancies were refined with the constraint that both the anion and cation sites remain fully occupied. The rock-salt structure contains both cations and anions which are statically disordered; the octahedral (4*a*), sodium sites are equally occupied by Na^+ and Li^+ (50% - 50%), while the 4*b* sites are occupied by both BH_4^- and I^- (*Figure 3.8*).

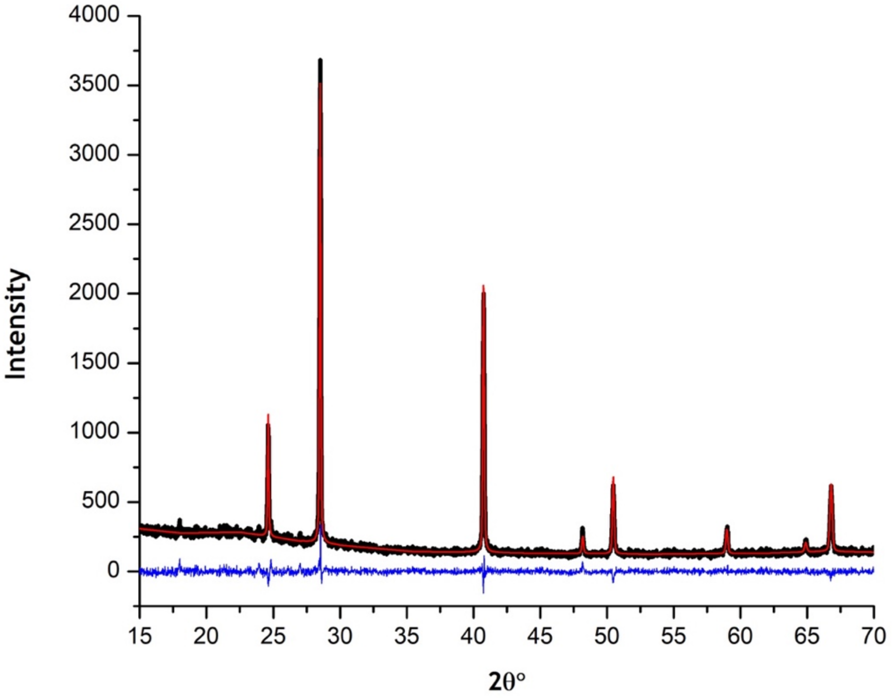

Figure 3. 7: Profile plot from the Rietveld refinement of the PXD pattern of sample EA001-c. (black line: observed data plot, red line: calculated data plot, blue line: difference profile).

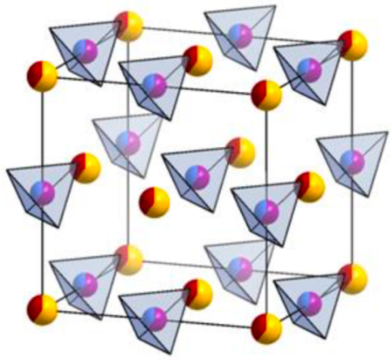

Figure 3. 8: Crystal structure of cubic $Li_{(1-y)}Na_y(BH_4)_{(1-x+yx)}X_{x(1-y)}$ (HP - $LiBH_4$ - type). Borohydride anions are shown as blue B-centred polyhedra and halides are represented by purple spheres (super-impeded on the $(BH_4)^-$ anions. Red/yellow spheres represent Li^+/Na^+ [32].

Refined Geometry Data / EA001-c (x^2 = 1.193 / R_{wp} = 0.0749)					
Atoms	**Occupancy**	**Atomic positions**			**Thermal Displacement Parameters (Å^2)**
		x	**y**	**z**	
Li	0.5	0	0	0	0.03
B	0.808(4)	0.5	0.5	0.5	0.022(6)
H	0.5	0.3779	0.3779	0.3779	0.03
Na	0.5	0	0	0	0.03
I	0.192(4)	0.5	0.5	0.5	0.022(6)

Table 3. 2: Refined geometry data for experiment EA001-c.

At this point, it is important to consider the limitations of the structural model given the dominant X-ray scattering of the relatively heavier sodium and iodide ions. In order to overcome this limitation, a model that considers the BH_4^- to be a single, spherical scatterer can be used effectively for refining approximate compositions from PXD data. However, because of the existence of several light atoms (Li, B, H), in the presence of heavier Na and I, a meaningful and definitive crystal structure of this material is only likely to be obtained using powder neutron scattering (PND). In fact, the X-ray scattering from statistical of Na^+/Li^+ and BH_4^- /I^- is almost identical and hence the scattering contrast is almost negligible between the cation and anion positions. PND experiments would require synthesis of an isotopically-enriched variant of the compound with D, ^7Li and ^{11}B, to minimise incoherent scattering and absorption.

After the full structural characterisation of $Li_{0.5}Na_{0.5}(BH_4)_{0.81}I_{0.19}$, different periods of both ball milling and thermal treatment were studied for the [$LiBH_4$-LiI-$NaBH_4$] system.

The fixed compositions and ratios of raw materials varying the duration of milling from 5-24 *h*. A 24 *h* milling period was required (EA001-b) in the milling stage to enable a complete reaction to the cubic product. Shorter periods of milling would not guarantee a complete crystallisation of the final structures, even after thermal treatment.

On the other hand, it was observed that the duration of thermal treatment did not affect product formation or crystallisation. In *Figure 3.9*, the observed X-ray diffraction pattern of the $Li_{0.5}Na_{0.5}(BH_4)_{0.81}I_{0.19}$ compound, after 4 *h* of thermal treatment (EA001d) is presented. A comparison between EA001-c and EA001-d samples is also shown here.

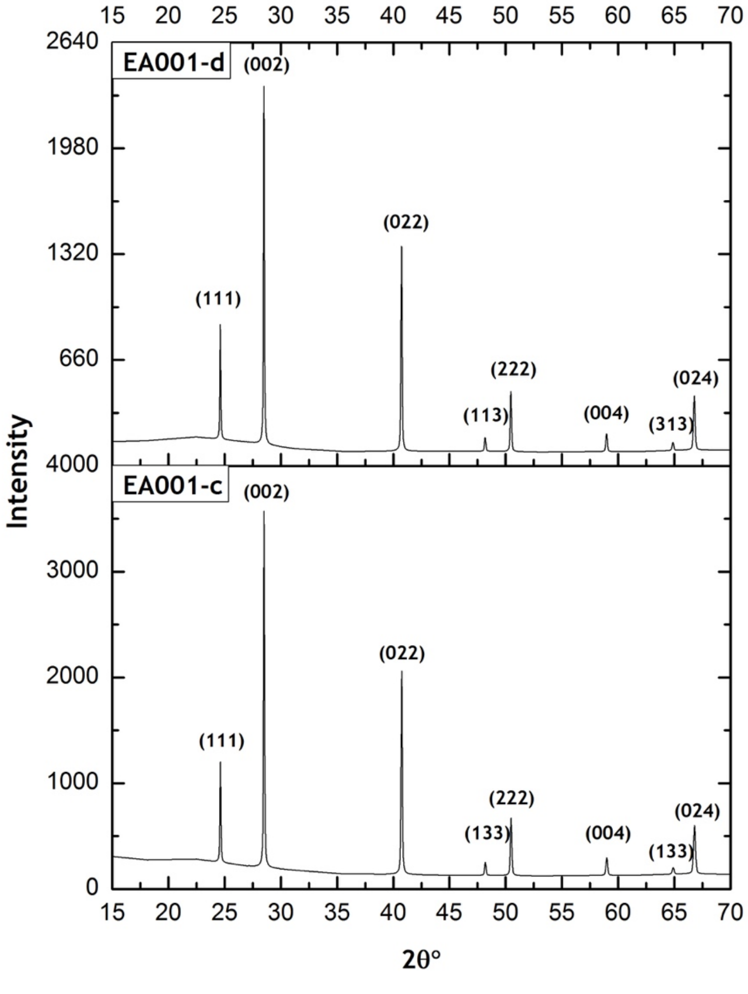

Figure 3. 9: Comparative presentation of samples EA001-c & Ea001-d, after 2 *h* and 4 *h* of thermal treatment, respectively.

In this case, the only difference observed is related to the peaks' intensity, as the peaks of the longer, thermally treated sample present lower intensities. One explanation of this observation could be potential changes in the geometrical disorder of the structure due to longer exposure in 200 °*C*. However, such a supposition could only be either confirmed or withdrawn after further structural characterisation of the samples by PND experiments.

3.3.1.2 Experiment - EA002

The second group of experiments was designed for the study of a different composition in the same [$LiBH_4$-LiI-$NaBH_4$] system, following the same synthesis process as that for experiment EA001 as presented before.

For the first step of experiment EA002, ~0.7 *g* of the precursor mixture $LiBH_4$ - LiI were mechanically milled by applying a milling speed of 500 *rpm*, for 4 *h*, following a pattern of 2 *min* milling / 2 *min* breaks to avoid over-heating of the materials. The previously milled $Li(BH_4)_{1-y}I_y$ precursor sample was further milled after the addition of a stoichiometric amount (1:1) of $NaBH_4$, for 24 *h*, by applying a milling speed of 500 *rpm* and following the same pattern of 2 *min* milling / 2 *min* breaks to avoid over-heating of the materials.
Detailed information on the experimental ratios, quantities and chemical systems, for experiment EA002, are shown in Table 3.3. The stainless-steel jar was loaded with 6 stainless-steel balls (*d* = 10 m*m*), for each experimental step. Due to the air-sensitive nature of the materials, all the manipulations were held under argon atmosphere, inside the glove box.

Experiment - EA002					
Samples	**Reactants**	**Molar Ratio**	**Moles**	**Mass (*g*)**	**Duration (*h*)**
	Step 1: $LiBH_4 + LiX \rightarrow 2Li(BH_4)_{0.5}I_{0.5}$				
a	$LiBH_4$	1	$4.59\cdot10^{-3}$	0.1	4
	LiI	1	$4.59\cdot10^{-3}$	0.614	
	Step 2: $Li(BH_4)_{0.5}I_{0.5} + NaBH_4 \rightarrow 2Li_{0.5}Na_{0.5}(BH_4)_{0.69}I_{0.31}$				
b	$Li(BH_4)_{0.5}I_{0.5}$	1	$7.89\cdot10^{-3}$	0.614	24
	$NaBH_4$	1	$7.89\cdot10^{-3}$	0.298	
	Step 3: Annealing of $Li_{0.5}Na_{0.5}(BH_4)_{0.69}I_{0.31}$				
c	$Li_{0.5}Na_{0.5}(BH_4)_{0.69}I_{0.31}$	-	-	~ 0.2	2
d	$Li_{0.5}Na_{0.5}(BH_4)_{0.69}I_{0.31}$	-	-	~ 0.2	4

Table 3. 3: Experimental parameters and conditions of experiment type EA002.

Following the mechanochemical treatment, the sample was heated to 200 ^0C, for 2 h, according to the procedure described in Section 3.3.

Figure 3.10-a shows the X-ray diffraction pattern of the final product (EA002-c), which can be assigned to a “rock-salt” type structure of nominal stoichiometry $Li_{0.5}Na_{0.5}(BH_4)_{0.69}I_{0.31}$.

Rietveld structural refinement was performed for the above sample. X-ray powder diffraction data collected indicated the formation of a single, cubic phase [$Fm\bar{3}m$, a = 6.3102(5) Å, V = 251.27(0) $Å^3$]. The plot produced from the refinement is shown in Figure 3.10-a.

Diffraction evidence thus suggested that the HP-$LiBH_4$ phase could indeed be stabilised in a mixed metal borohydride, at RT, via iodide substitution at a level of ca. 31%.

The background was successfully modelled using linear interpolation. The peak shape was modelled using a pseudo-Voigt function. The site occupancies were refined with the constraint that both the anion and cation sites remain fully occupied (*Table 3.4*).

As the amount of the halide increases in the precursor, the cell volume increases as well. Therefore, a displacement of the EA002-c peaks, to lower 2θ values, is observed if compared to the EA001-c observed PXD pattern (*Figure 3.10-b*).

Refined Geometry Data / EA002-c (x^2 = 1.409 / R_{wp} = 0.1207)					
Atoms	**Occupancy**	**Atomic positions**			**Thermal Displacement Parameters ($Å^2$)**
		x	y	z	
Li	0.5	0	0	0	0.03
B	0.690(1)	0.5	0.5	0.5	0.021(9)
H	0.5	0.3779	0.3779	0.3779	0.03
Na	0.5	0	0	0	0.03
I	0.310(1)	0.5	0.5	0.5	0.021(9)

Table 3. 4: Refined geometry data for experiment EA002-c.

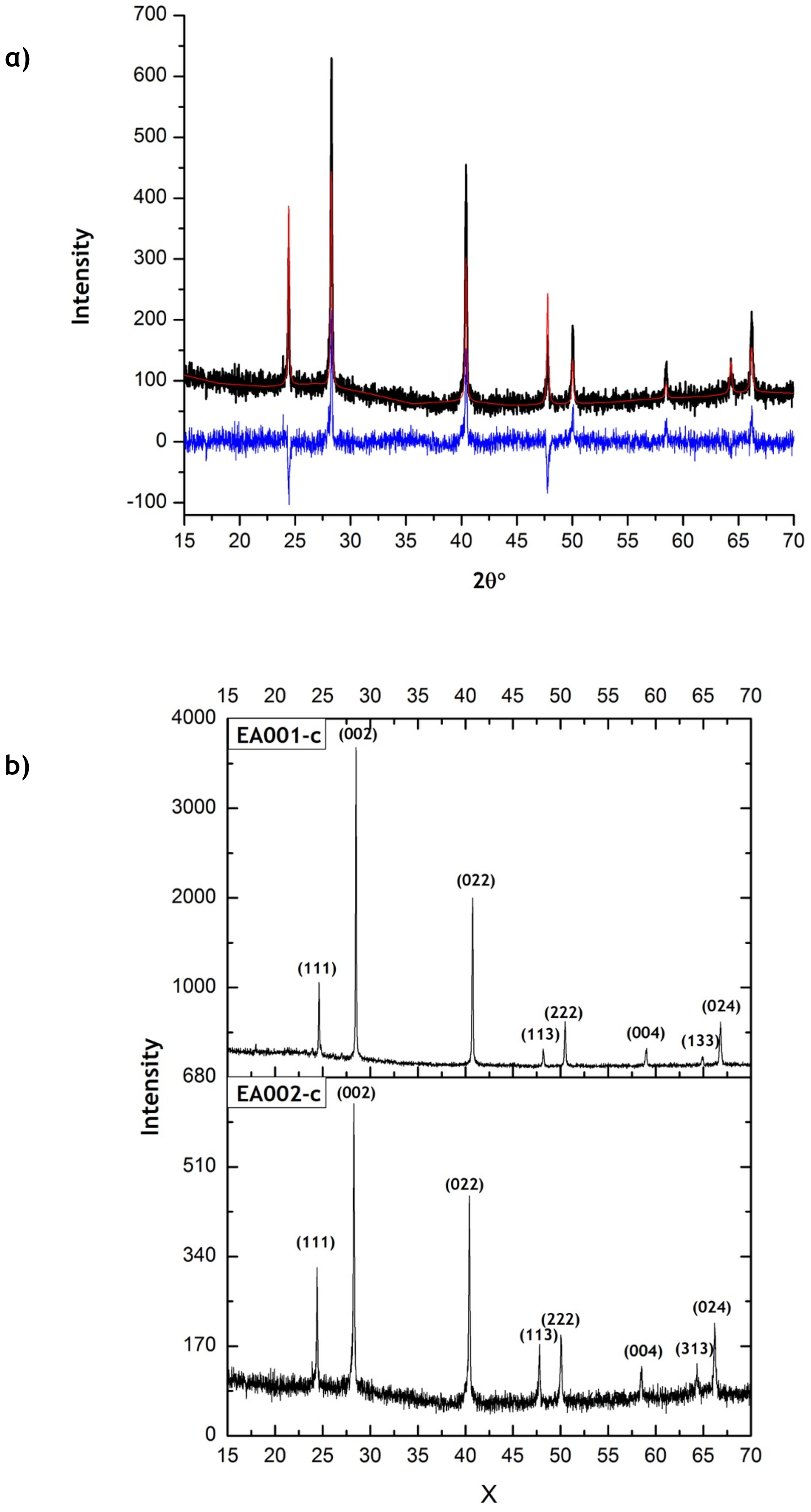

Figure 3. 10: **(a)** PXD pattern of sample EA002-c. Completed synthesis of the $Li_{0.5}Na_{0.5}(BH_4)_{0.69}I_{0.31}$ compound after thermal treatment of sample EA002-b at 473 *K*, for 2 *h*. The peaks were assigned to the cubic, HP-polymorph of $LiBH_4$, **(b)** Comparative presentation of samples EA002-c & Ea001-c, after 2 *h* of thermal treatment, each.

3.3.1.3 Further characterisation of EA001 & EA002

Thermogravimetric experiments confirm that no loss of mass takes place as the temperature rises, a fact indicating that all of the LiI is incorporated into the $LiBH_4$: LiI precursor and, thus, into the final structure. In Figure 3.11 the thermal study of the $Li_{0.5}Na_{0.5}(BH_4)_{0.81}I_{0.19}$ compound before thermal treatment (EA001b) is presented during heating from RT to 420 °*C*, at 5 °*C*·*min*$^{-1}$.

The thermogravimetric experiments were conducted for confirmation that no mass loss takes place after heating the samples in a wide range of temperatures. The two endothermic peaks appearing at 115.425 °*C* and 331.125 °*C*, risking a first assumption, correspond to phase transitions. The first endothermic peak can be assigned to the transition from the orthorhombic, LT-phase of $LiBH_4$ to the hexagonal, HT-phase, especially as EA001-b contains a LT-$LiBH_4$ phase (Figure 3.5). The second peak cannot yet be fully explained from the evidence available. However, based on the indication of a tiny mass loss (~ 0.2 %) following the second endothermic event around 330 ^{0}*C* the second peak could represent the melting of the final compound above 300 ^{0}*C*.

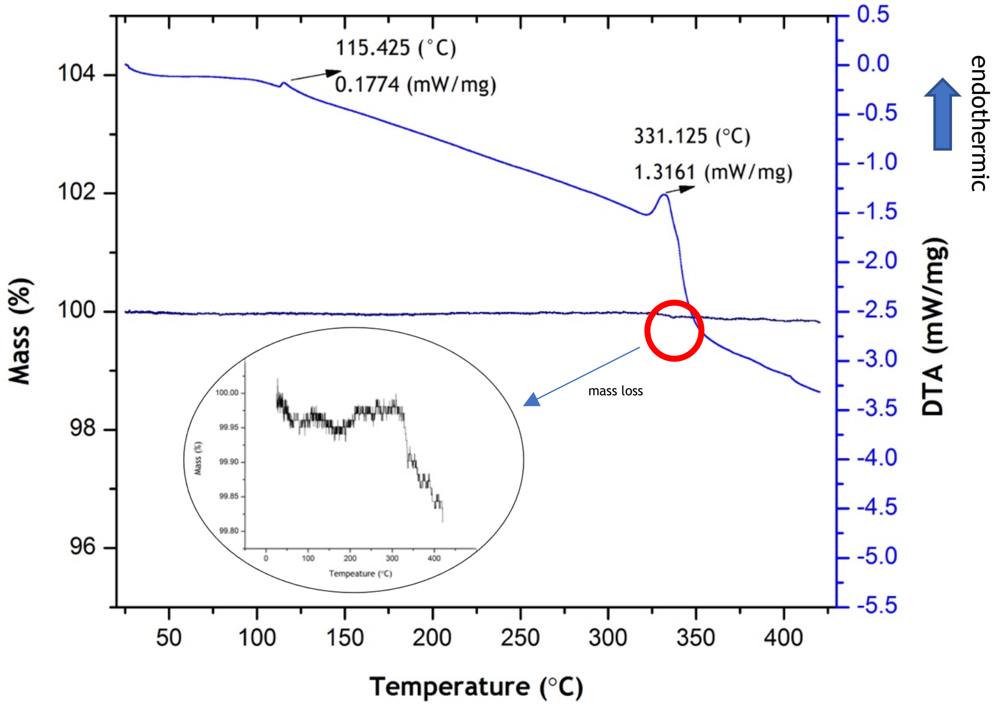

Figure 3. 11: Thermogravimetric analysis of the $Li_{0.5}Na_{0.5}(BH_4)_{0.81}I_{0.19}$ compound (EA001b) during heating, from RT to 420 ^{0}*C*.

The samples synthesised using the process described above, were, also, studied by **Raman spectroscopy**. It is known that the LT-$LiBH_4$ structure presents a splitting of the bending modes (v_2 and v_2'), due to the anisotropy of the B-H atomistic vibrations in this orthorhombic structure [33]. This splitting, however, is no longer present when the structure is heated and the higher-symmetry, hexagonal phase is formed [17][34]. The same behaviour is, also, displayed when the hexagonal, HT-phase of $LiBH_4$ is stabilised at room temperature by anion-substitution with halides [32]. The Raman spectra of samples EA001c, EA001d, EA002c, EA002d, commercial LT-$LiBH_4$ and $NaBH_4$ are shown in Figure 3.12. One comparative graph of the two HP-, $Li_{0.5}Na_{0.5}(BH_4)_{0.83}I_{0.17}$ and $Li_{0.5}Na_{0.5}(BH_4)_{0.75}I_{0.25}$ compounds after 2 *h* of thermal treatment (EA001c & EA002c) as well as the same compounds after 4 *h* of thermal treatment (EA001d & EA002d) are presented here.

Ionic solids of monoatomic ions, such as LiI, do not present molecular vibrations, but rather, produce lattice modes through the vibrations of the individual ions in the crystalline lattice. These vibrations result in bands generally occurring below 200 cm^{-1} [35] . Thus, the peaks appearing in the 1000-4000 cm^{-1} region can be assigned only to B-H vibrations within the complex anion of the $LiBH_4$ and $NaBH_4$ structures. Results indicate that, in the case of HP-$LiBH_4$ structures, the bending modes' splitting is being reduced but not totally diminished. This observation indicates an intermittent behaviour of the obtained structures when these are compared with the raw, commercial powders of $LiBH_4$ and $NaBH_4$ used. This indication could propose that the structural profile of the above compounds still presents part of the B-H atomistic vibrations due to bond anisotropy.

In general, the samples produced spectra with bands at similar Raman shifts to isostructural $NaBH_4$. A matter that needs further investigation is the fact that, despite evidence to the contrary from previous work in our group [32], the Raman shift of the B–H stretching mode is slightly lower for the samples presented here than for $NaBH_4$, while the Raman shift of B–H bending modes is slightly higher (*Table 3.5*).

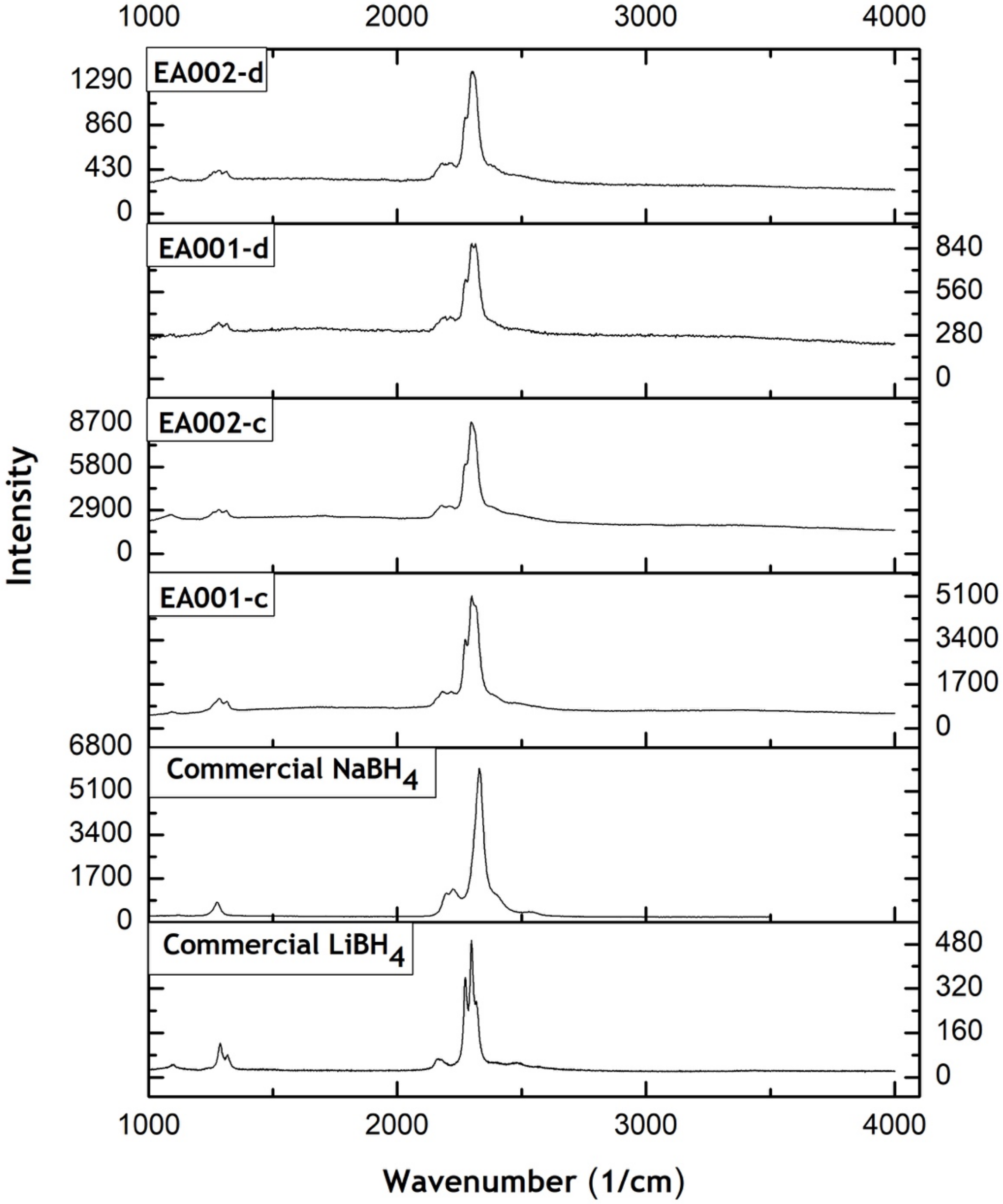

Figure 3. 12: Raman spectra of samples EA001-c, EA001-d ($Li_{0.5}Na_{0.5}(BH_4)_{0.81}I_{0.19}$), EA002-c, EA002-d ($Li_{0.5}Na_{0.5}(BH_4)_{0.69}I_{0.31}$) and comparison with commercial, as received samples of LT-LiBH$_4$ and NaBH$_4$.

Further investigation towards an explanation was not possible due to time limitations.

Sample	B-H stretching Raman Shift (cm^{-1})	B-H bending Raman Shift (cm^{-1})
Commercial $NaBH_4$	2325	1269
EA001c / EA002c	2302	1292
EA001d / EA002d	2304	1290

Table 3. 5: Comparative presentation of Raman shifts of the B-H stretching mode and the B-H bending modes of commercial $NaBH_4$ and various prepared samples.

3.3.1.4 Li^+ ion migration in HP-$LiBH_4$ - like structures

In order to understand the behaviour of the activation energy for migration in the samples presented above (Table 3.1 & Table 3.3), one should consider the possible paths followed by Li^+ ions while jumping from a lattice site into an adjacent vacancy. Studies have suggested different possible Li-ion diffusion pathways in LiX phases (X = F, Cl, Br or I) via "direct" and "indirect" jumps, similar to the diffusion pathways in NaCl [36].

As no conductivity measurements have been carried out in the context of this work and solely based on the observation that the compounds presented above present significant similarities to the structures reported by *Cascallana et al.* [32], a similar diffusion mechanism could be possible for the synthesised materials in this work.

In Figure 3.13, a "sub-cube" with the cations and anions at alternate corners can be considered, which corresponds to one-eighth of the unit cell of (substituted) $NaBH_4$.

The direct jump of Li^+ across the sub-cube face is not favourable as the BH_4^- / I^- (blue anions 1 and 2) are very close and, thus, it could be physically unfavourable for a Li^+ to occupy the space between them. As an alternative, Li^+ follows an indirect route through the centre of the sub-cube. At the cube centre there is an interstitial site that is equidistant from the eight corners.

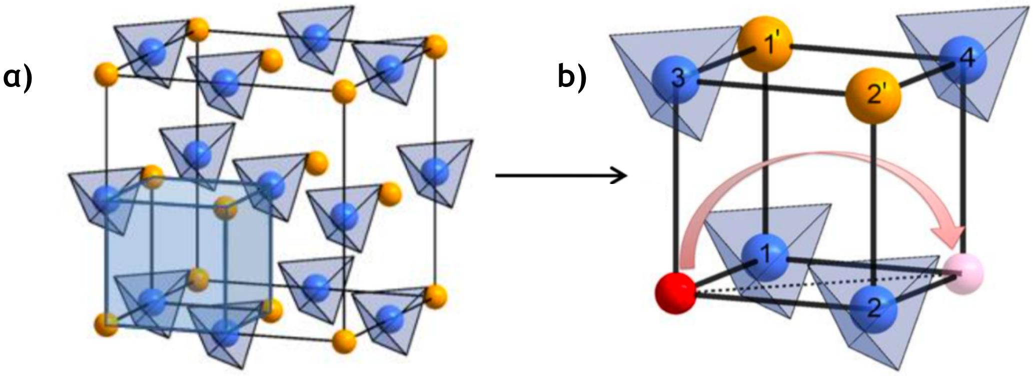

Figure 3. 13: Proposed pathway for Li⁺ migration in $Li_{(1-y)}Na_y(BH_4)_{(1-x+yx)}X_{x(1-y)}$.
(a) Borohydride/halide anions are shown as blue B(X')-centred polyhedra, while Li⁺ are represented as red spheres and Na⁺ as yellow spheres.
(b) One corner Li⁺ site in the "sub-cube" (1/8 of the entire NaCl unit cell) acts as an "empty" site and a lithium ion from an opposite corner moves to occupy it. The direct and indirect jump are represented by the dotted line and curved arrow, respectively [32].

Four of the corners are occupied by BH_4^- / X^-, which are arranged tetrahedrally around the site. Prior to Li^+ ion's arrival at the central interstitial site, it passes through a triangular window formed by anions 1, 2 and 3. The time that the cation (Li^+) spends in this site must be short because of the proximity of the other cations (Li^+ / Na^+) (yellow spheres, 1' and 2').

Calculations of migration energies of Li^+ in LiX (X = F, Cl, Br or I) show a tendency for the migration energy to decrease as the atomic number of the halide increases [37]. This observation id attributed to the fact that larger anions in a "rock-salt" structure allow Li+ ions to jump through the middle of the cell because of their larger open channels.

3.3.2 Approach 2: "One-step synthesis"

3.3.2.1 Experiment - EA003

The second approach consisted of one step and was applied as an alternative to the synthesis of the $Li_{0.5}Na_{0.5}(BH_4)_{0.83}I_{0.17}$ compound described in Section 3.3.1.1.

In contrast to first approach, for this second synthesis process the compounds of the $LiBH_4$-LiI-$NaBH_4$ system were ball milled in one step, omitting the preliminary synthesis of the $LiBH_4$-LiI precursor, thus reducing time and complexity. Importantly, the one-step milling would further minimise the possible exposure of the materials to air and moisture, removing multiple transfers between the glove box and the ball mill.

The underpinning question was whether the anion- and cation-substitution could take place "at the same time" (i.e. in one synthesis step). Additionally, the subsequent contribution of an annealing step could be assessed, in terms of whether this was necessary to complete the reaction or simply to improve crystallinity.

Once again, in order to simplify the experimental design and decrease the number of the dependent variables, the quantity and molar ratio of the cations were kept constant throughout the experiments.

For the first step of experiment EA003, ~1.3 *g* of the [$LiBH_4$ - LiI - $NaBH_4$] mixture was mechanically milled (500 *rpm*, for 24 *h*, ball : powder ratio of 80 : 1), following a pattern of 2 *min* milling / 2 *min* breaks to avoid over-heating of the materials (*Table 3.6*). The stainless-steel jar was loaded with 6 stainless-steel balls (*d* = 10 *mm*). Due to the air-sensitive nature of the materials, all the manipulations were performed in an argon filled glove box.

Experiment - EA003					
Samples	**Reactants**	**Molar Ratio**	**Moles**	**Mass (*g*)**	**Temperature (^0C)**
	Step 1: $2LiBH_4 + LiX + 3NaBH_4 \rightarrow 6Li_{0.58}Na_{0.42}(BH_4)_{0.88}I_{0.12}$				
a	$LiBH_4$	2	$9.18\cdot10^{-3}$	0.2	-
	LiI	1	$4.59\cdot10^{-3}$	0.614	
	$NaBH_4$	3	$13.77\cdot10^{-3}$	0.521	
	Step 2: Annealing of $Li_{0.58}Na_{0.42}(BH_4)_{0.88}I_{0.12}$				
b	$Li_{0.58}Na_{0.42}(BH_4)_{0.88}I_{0.12}$	-	-	~ 0.2	100
c	$Li_{0.58}Na_{0.42}(BH_4)_{0.88}I_{0.12}$	-	-	~ 0.2	200
d	$Li_{0.58}Na_{0.42}(BH_4)_{0.88}I_{0.12}$	-	-	~ 0.2	300
e	$Li_{0.58}Na_{0.42}(BH_4)_{0.88}I_{0.12}$	-	-	~ 0.2	400

Table 3. 6: Quantitative data of experiment EA003.

Following the mechanochemical treatment, the sample was split into four parts and each heated, for 2 *h* at the temperatures in Table 3.6. The powder X-ray diffraction (PXD) data are presented below (*Figures 3.14-3.15*).

Figure 3.14 shows the X-ray pattern of the $Li_{0.5}Na_{0.5}(BH_4)_{0.88}I_{0.12}$ compound immediately after milling (EA003-a). PXD data indicate the formation of a "rock-salt" type structure, which is presumably composed of both cations and both anions (50% Li^+ / 50% Na^+, 88% BH_4^- / 12% I). The nominal $Li_{0.5}Na_{0.5}(BH_4)_{0.88}I_{0.12}$ compound can be indexed as a cubic structure.

Structural characterisation, based on the retrieved PXD data, indicate the formation of a cubic phase [*Fm*$\overline{3}$*m*, a = 6.267(9) Å, *V* = 246.24(4) Å^3]. Secondary peaks indicate the existence of a tiny amount of what (most probably) seems to be the LT-phase of $LiBH_4$. Therefore, the stabilisation of the complex, mixed-ion borohydride, at RT, can be confirmed, achieved via an iodide substitution level of 17%. Unlike the previous syntheses using a $Li(BH_4)_{1-y}X_y$ precursor (EA001 & EA002), the HP-phase can be formed in this case prior to thermal treatment.

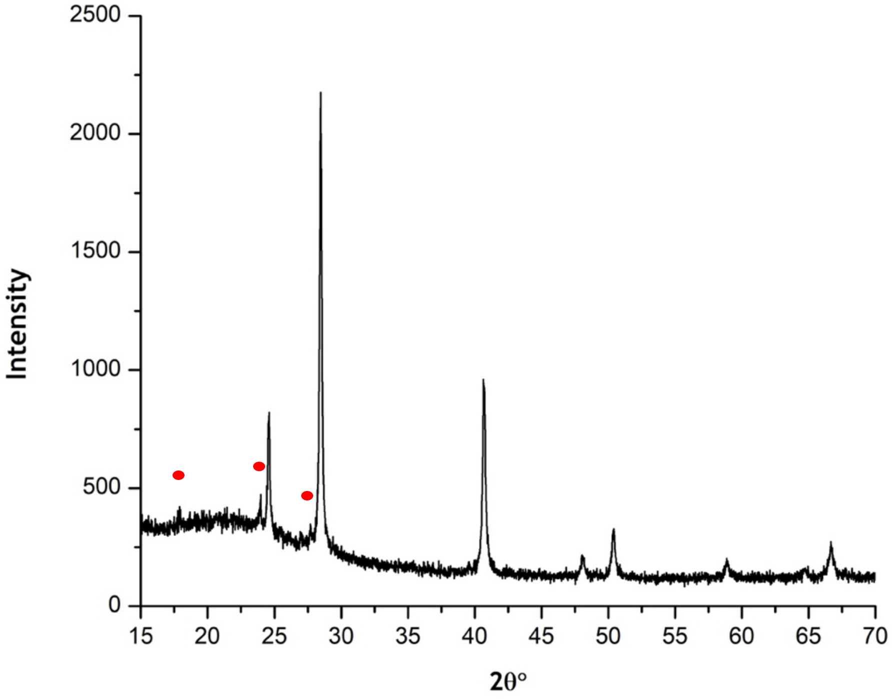

Figure 3. 14: PXD pattern of sample EA003-a. Retrieval of the $Li_{0.58}Na_{0.42}(BH_4)_{0.88}I_{0.12}$ compound after 24 *h* of ball milling, at 500 *rpm*. The peaks were fitted with the cubic, HP-polymorph of $LiBH_4$. Secondary peaks, indicated with red dots, possibly indicate the existence of a tiny amount of LT-phase of $LiBH_4$.

These results confirmed that simultaneous cation- and anion-substitution could proceed in one mechanochemical reaction. This implies that the $Li(BH_4)_{(1-y)}X_y$ precursor is not essential in the formation of the cubic HP-phase and indeed, once formed, heating is necessary to convert the HT-phase to the HP-phase.

Following this observation, the effect of heating the milled sample (EA003-a) at various temperatures was investigated (experiments EA003-b, EA003-c, EA003-d and EA003-e; *Table 3.5*).

Figure 3.15 shows the PXD patterns retrieved for experiments EA001-a, EA001-b, EA001-c and EA001-d. Four of the seven main peaks of each plot are indicated on each pattern for reference. Results from experiment EA003-e are not reported as, after heating for 2 h, at 400 ^0C, the product was a hard, solid mass, which rendered its removal from the silica tube impossible. Here it is interesting to note that after heating for 2 h, at 300 ^0C, the powdered sample became grey and significantly harder.

A preliminary observation of the obtained data suggests that there is no significant difference, either between the -solely- ball milled sample (EA003-a) and each of the annealed ones (EA003-b, EA003-c, EA003-d). It would appear that ball milling of the [$LiBH_4$ – LiI – $NaBH_4$] mixture for 24 h, is enough to form the cubic, HP-$LiBH_4$-type phase. It is important to note at this point that, the peak at about 17°, for the 100 $°C$ and 300 $°C$ samples, has no significance for the results. Due to a malfunction of the Bruker D8 Advance powder diffractometer, the PANalytical X'Pert Pro diffractometer was used for the collection of the EA003-b and EA003-d data. The latter presents much better clarity and precision in measurement than the Bruker D8 thus, the the peak at about 17° is attributed to the Bruker diffractometer's lower ability to smooth out noise signals.

Detailed structural characterisation was performed for all the four experiments mentioned in this section (Section 3.3.2). Here the full structural characterisation of the sample EA003-c is presented, to enable a direct comparison with sample EA001-c sample, obtained by the first synthesis approach and analysed in Section 3.3.1.1. As mentioned earlier, X-ray powder diffraction data indicate the formation of a single, cubic phase [$Fm\bar{3}m$, a = 6.259(7) Å, V = 245.28 Å^3]. The phase can be assigned to a "rock-salt" type structure, which is composed of mixed cation - anion borohydrides (58% Li$^+$ / 42% Na$^+$, 88% BH_4^- / 12% I). Therefore, the stabilisation of the complex, mixed-ion borohydride, at RT, can be confirmed, via iodide substitution by 12% following this synthesis approach as well.

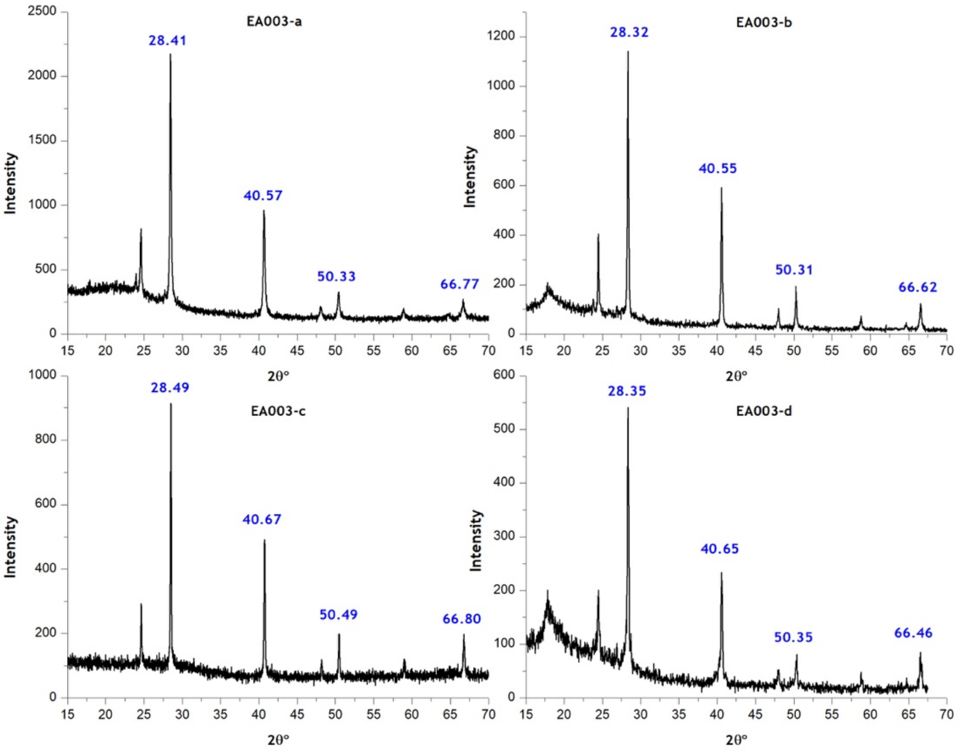

Figure 3. 15: Comparative depiction of the PXD data obtained for samples EA003-a (BM for 24 *h*), EA003-b (100 ^0C), EA003-c (200 ^0C) & EA003-d (300 ^0C). The 2θ° diffraction angles for four of the main peaks are indicated on each plot for an easier comparison.

The results for the $Li_{0.5}Na_{0.5}(BH_4)_{0.81}I_{0.19}$ compound synthesised by the "two-step synthesis" are identical to the corresponding structure developed by the "three-step synthesis" as reported previously (EA001-c). As a reminder, the "rock-salt" type structure was indexed as a single, cubic phase [$Fm\bar{3}m$, a = 6.260(9) Å, V = 245.42 Å^3].

The profile plot from the structural refinement of EA003-c is shown in Figure 3.16.

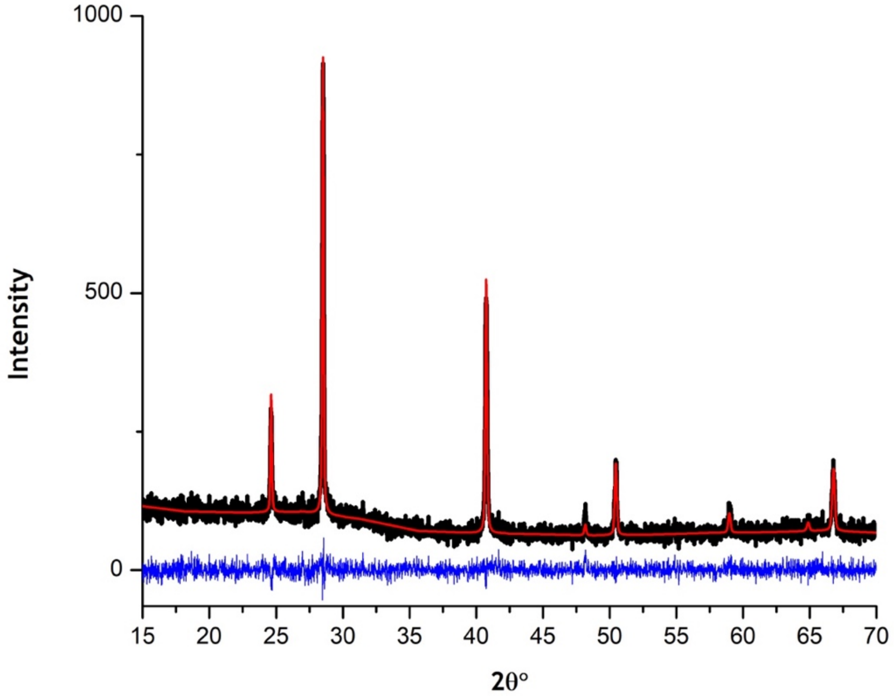

Figure 3. 16: Profile plot from the Rietveld refinement of sample EA003-c against PXD data. (black line: observed data plot, red line: refined data plot, blue line: difference profile).

The structures of each of the four samples prepared by the "one-step" synthesis, were refined against PXD data using the cubic $Fm\bar{3}m$ phase as an initial model. In all cases, the background was successfully modelled using linear interpolation and the peak shape using a pseudo-Voigt function. The site occupancies were refined with the constraint that both the anion and cation sites remain fully occupied, exactly as done for the refinements in Section 3.3.1. The "rock-salt" structures contain cations and anions which are statically disordered; the octahedral (*4a*), sodium sites are equally occupied by Na^+ and Li^+ (58% - 42%), while the *4b* sites are occupied by both $(BH_4)^-$ and I^- (88% - 12%).

The atomic positions and isotropic temperature factors (U_{iso}), obtained from Rietveld refinement of the EA003-c PXD data, are presented in Table 3.7. The higher value of R_{wp} could indicate a higher complexity of the final product compared to the slower, "two-steps" synthesis' products. The higher complexity could be attributed to a lightly higher trace of the first two phases, the orthorhombic and hexagonal ones, in the “one-step” synthesis’ product. However, no significant difference in the final products’ characteristics and properties could be assumed.

Refined Geometry Data / EA003-c (x^2 = 1.126 / R_{wp} = 0.1856)					
Atoms	**Occupancy**	**Atomic positions**			**Thermal Displacement Parameters (Å^2)**
		x	**y**	**z**	
Li	0.584(9)	0	0	0	0.0383(4)
B	0.884(2)	0.5	0.5	0.5	0.0251(8)
H	0.5	0.3779	0.3779	0.3779	0.0008(9)
Na	0.416(9)	0	0	0	0.0383(4)
I	0.115(2)	0.5	0.5	0.5	0.0251(8)

Table 3. 7: Refined geometry data for sample EA003-c.

Table 3.8 shows the crystallographic parameters of the corresponding experiments, as derived from Rietveld refinement of the observed PXD data.

Samples	Space Group	Lattice Parameters (Å)			Volume (Å^3)
		a	b	c	
EA003-a	$Fm\bar{3}m$	6.267(9)	6.267(9)	6.267(9)	246.24
EA003-b	$Fm\bar{3}m$	6.271(6)	6.271(6)	6.271(6)	246.69
EA003-c	$Fm\bar{3}m$	6.259(7)	6.259(7)	6.259(7)	245.28
EA003-d	$Fm\bar{3}m$	6.268(9)	6.268(9)	6.268(9)	246.36

Table 3. 8: Crystallographic parameters for sample EA003-c.

Based on the results presented above, it would appear that annealing at temperatures from 100-300 ^{0}C had little effect on the crystal structure of the HP-type phase. The lattice parameters and cell volumes remain almost identical within ESDS between the four studied samples. There is, however, an indication that at ca. 400 ^{0}C, the sample becomes a hard, solid mass, with no evidence that the volume of the sample is reduced. This was one motivation for performing thermogravimetric analysis and the results are presented in Section 3.3.2.2.

3.3.2.2 Further study of experiment EA003 (Approach 2)

Thermogravimetric experiments confirm that no loss of mass takes place as the temperature rises, a fact indicating that all of the LiI is incorporated into the final structure. In Figure 3.18 the thermal study of the $Li_{0.58}Na_{0.42}(BH_4)_{0.88}I_{0.12}$ compound before thermal treatment (EA003-a) is presented during heating from RT to 420 $°C$, at 5 $°C \cdot min^{-1}$.

Similarly, to EA001-b thermal treatment results, the first endothermic peak at 103.948 $°C$, most probably, refers to phase transition from the LT-$LiBH_4$, orthorhombic phase to the HT-$LiBH_4$, hexagonal phase. The second peak at 237.948 $°C$ is, in this case as well, followed by a tiny mass loss (~ 0.6 %) as indicated in Figure 3.18 by the red circle. Considering both this observation and the fact that after heating for 2 h, at 300 ^0C, the powdered sample became grey and significantly harder, leading to its transformation into a hard, solid mass -with no visual evident of mass loss- after heating for 2 h, at 400 ^0C, our initial explanation that the second peak could represent the melting of the final compound above 300 ^0C is significantly strengthened. The two peaks are shifted towards lower temperatures in comparison with the sample EA001-b obtained by the first synthesis approach (see Section 3.3.1.3). This observation could probably be explained by different reaction kinetics (i.e. difference in particle size of the initial system's compounds, different surface areas) that govern the second synthesis process, due to the different starting chemical system ($Li(BH_4)_{(1-x)}X_x$: $NaBH_4$ for the first approach vs. $LiBH_4$ – LiI -$NaBH_4$ for the second approach). Finally, no evidence of any evolved gases was observed. Further investigation for the determination of the reaction mechanism would provide useful information on the matter, however, it was not possible in this project due to time limitations.

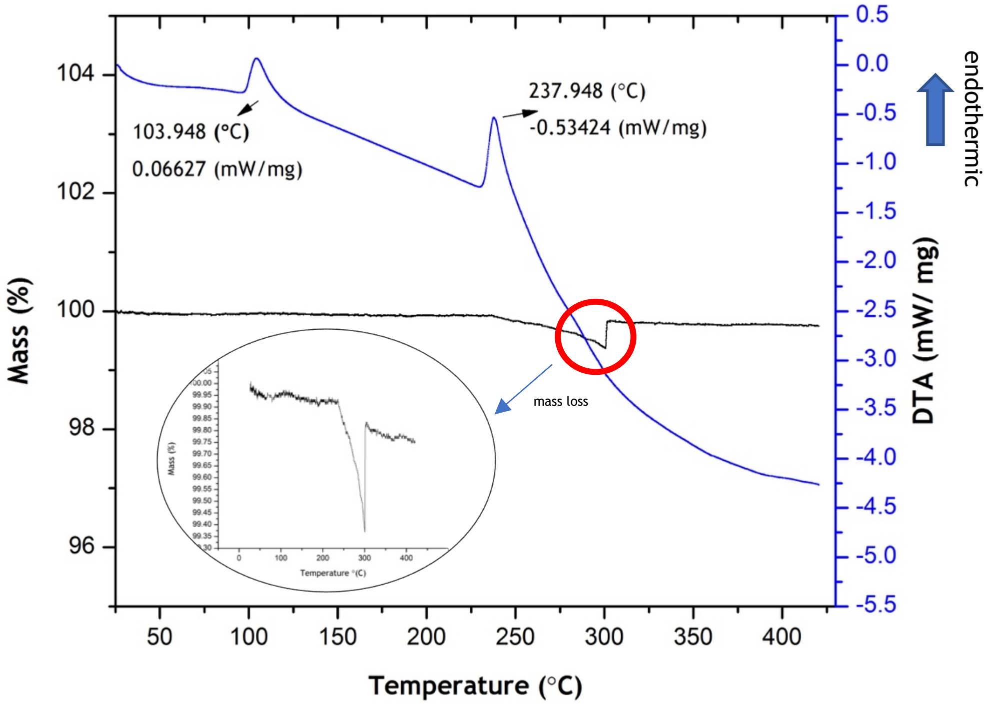

Figure 3. 17: Thermogravimetric analysis of the $\mathrm{Li_{0.58}Na_{0.42}(BH_4)_{0.88}I_{0.12}}$ compound (EA003-a) during heating, from RT to 420 ^0C.

The, samples, synthesised using the processing described above, were, also, studied by **Raman spectroscopy**. It is known that the LT-$LiBH_4$ structure presents a splitting of the bending modes (v_2 and v_2'), due to the anisotropy of the B-H atomistic vibrations in this orthorhombic structure [33]. This splitting, however, diminishes when the structure is heated [17][34]. The same behaviour is, also, displayed when the hexagonal, HT-phase of $LiBH_4$ is stabilised at room temperature by anion-substitution with halides [32]. The Raman spectra of samples EA003-b and EA003-d are shown in Figure 3.19.

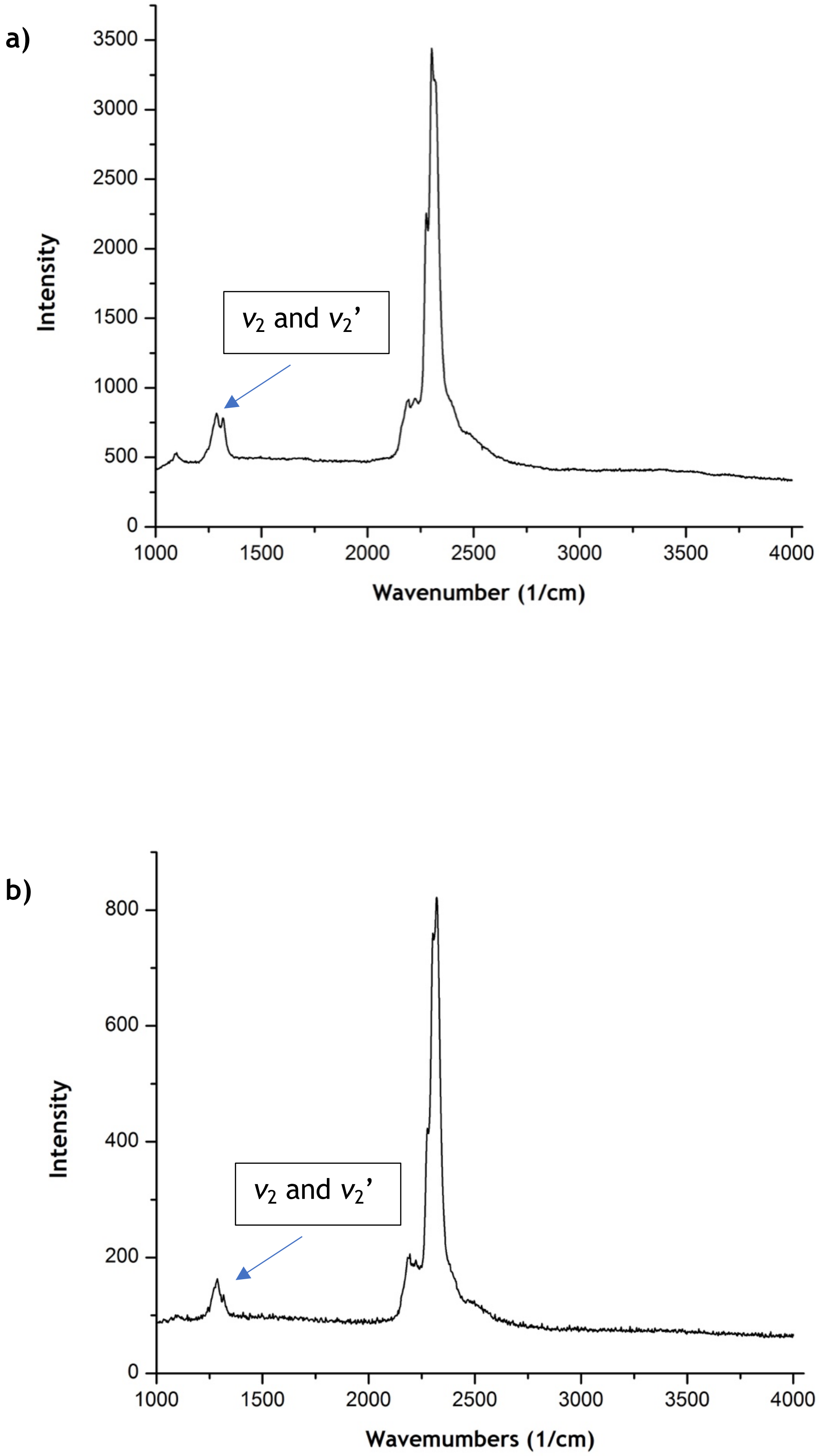

Figure 3. 18: **(a)** Raman spectra for sample EA003-b and **(b)** Raman spectra for sample EA003-d.

The samples selected consist of ca. 12% halide (I^-) and ca. 50% of each cation (Li^+ & Na^+). Ionic solids of monoatomic ions, such as LiI, do not present molecular vibrations, but only, produce lattice vibrations through the vibrations of the individual ions in the crystalline lattice. These vibrations can result in bands occurring below 200 cm^{-1} [35]. Thus, the peaks appearing in the 1000-4000 cm^{-1} region can be assigned only to light interaction with $LiBH_4$ and $NaBH_4$ structures. Results indicate that, in the case of HP-$LiBH_4$ structures, the bending modes' splitting is being reduced but not totally diminished. This observation indicates an intermittent behaviour of the obtained structures when these are compared with the raw, commercial powders of $LiBH_4$ and $NaBH_4$ used. This indication could propose that the structural profile of the above compounds still presents part of the B-H atomistic vibrations due to bond anisotropy.

In general, the structures showed similar Raman shifts to samples synthesised via the first. “two-step synthesis” approach. In that case as well, the Raman shift of the B-H stretching mode is slightly lower for the samples presented here than for $NaBH_4$, while the B-H bending modes is slightly higher; once again opposite to what was reported in previous work by our group [32]. This observation is presented in numbers below (*Table 3.9*) but, in the extend of this work, further investigation towards an explanation was not possible due to time limitations.

Sample	B-H stretching Raman Shift (cm^{-1})	B-H bending Raman Shift (cm^{-1})
Commercial $NaBH_4$	2325	1269
EA003-b	2301	1307
EA003-d	2319	1287

Table 3. 9: Comparative presentation of Raman shifts of the B-H stretching mode and the B-H bending modes of commercial $NaBH_4$ and EA003-b & EA003-d samples.

3.4 References

1. A. Züttel, P. Wenger, S. Rentsch, P. Sudan, Ph. Mauron and Ch. Emmenegger, *Journal of Power Sources*, 2003, **118**, 1–7.
2. A. Züttel, S. Rentsch, P. Fischer, P. Wenger, P. Sudan, Ph. Mauron and Ch. Emmenegger, *Journal of Alloys and Compounds*, 2003, **356–357**, 515–520.
3. B. Sakintuna, F. Lamari-Darkrim and M. Hirscher, *International Journal of Hydrogen Energy*, 2007, **32**, 1121–1140.
4. H.J. Schlesinger and H.C. Brown, *Journal of the American Chemical Society*, 1940, **62**, 3429–3435.
5. E.M. Fedneva, V.L. Alpatova and V.I. Mikheeva, *Russian Journal of Inorganic Chemistry*, 1964, **9**, 826–827.
6. M. Matsuo, Y. Nakamori, S. Orimo, H. Maekawa and H. Takamura, *Applied Physics Letters*, 2007, **91**, 1-3.
7. I. Cascallana-Matias, D.A. Keen, E.J. Cussen and D.H. Gregory, *Chemistry of Materials*, 2015, **27**, 7780.
8. P. C. W., *Z. Phys. Chem. Neue Folge*, 1974, **88**, 253-263.
9. P. Vajeeston, P. Ravindran, A. Kjekshus and H. Fjellvag, *Journal of Alloys and Compounds*, 2005, **387**, 97-104.
10. T. J. Frankcombe, G. J. Kroes and A. Züttel, *Chemical Physics Letters*, 2005, **405**, 73-78.
11. Z. Lodziana and T. Vegge, *Physical Review Letters*, 2004, **93**, 4.
12. H. Maekawa, M. Matsuo, H. Takamura, M. Ando, Y. Noda, T. Karahashi and S. Orimo, *Journal of the American Chemical Society*, 2009, **131**, 894-895.
13. H. Takamura, Y. Kuronuma, H. Maekawa, M. Matsuo and S. Orimo, *Solid State Ionics*, 2011, **192**, 118.
14. V. Dmitriev, Y. Filinchuk, D. Chernyshov, A.V. Talyzin, A. Dzwilewski, O. Andersson and B. Sundqvist, *Physical Review B*, 2008, **77**, 1-11.
15. M. Matsuo and S. Orimo, *Advanced Energy Materials*, 2011, **1**, 161–172.
16. H. Yamawaki, H. Fujihisa, Y. Gotoh and S. Nakano, *Journal of Physics and Chemistry of Solids*, 2015, **76**, 40-44.
17. J.-Ph. Soulié, G. Renaudin, R. Cerný and K. Yvon, *Journal of Alloys and Compounds*, 2002, **346**, 200-205.

18. S.C. Abrahams and J. Kalnajs, *The Journal of Chemical Physics*, 1954, **22**, 434-436.

19. P. Fischer and A. Züttel, presented in part at the EPDIC-8: European Powder Diffraction Conference, Uppsala, Sweden, May, 2002.

20. Y. Filinchuk, D. Chernyshov, A. Nevidomskyy and V. Dmitriev, *Angewandte Chemie International Edition*, 2008, **47**, 529-532.

21. A. V. Talyzin, O. Andersson, B. Sundqvist, A. Kurnosov and L. Dubrovinsky, *Journal of Solid State Chemistry*, 2007, **180**, 510-517.

22. H. Takamura, Y. Kuronuma, H. Maekawa, M. Matsuo and S. Orimo, *Solid State Ionics*, 2011, **192**, 118–121.

23. N. Bernstein, M. D. Johannes and K. Hoang, *Physical Review B*, 2013, **88**, 5.

24. J.S.G. Myrdal, D. Sveinbjornsson and T. Vegge, ECS Meeting Abstracts, MA2011-2002 Sec. B2019, abstract No. 2756.

25. M. Matsuo, A. Remhof, P. Martelli, R. Caputo, M. Ernst, Y. Miura, T. Sato, H. Oguchi, H.Maekawa, H. Takamura, A. Borgschulte, A. Züttel and S. Orimo, *Journal of the American Chemical Society*, 2009, **131**, 16389-16391.

26. M. Matsuo, H. Oguchi, T. Sato, H. Takamura, E. Tsuchida, T. Ikeshoji and S. Orimo, *Journal of Alloys and Compounds*, 2013, **580**, 98-101.

27. D.B. Ravnsbaek, M.B. Ley, Y.S. Lee, H. Hagemann, V. D'Anna, Y.W. Cho, Y. Filinchuk and T.R. Jensen, *International Journal of Hydrogen Energy*, 2012, **37**, 8428-8438.

28. M.B. Ley, D.B. Ravnsbaek, Y. Filinchuk, Y.S. Lee, R. Janot, Y.W. Cho, J. Skibsted and T.R. Jensen, *Chemistry of Materials*, 2012, **24**, 1654-1663.

29. L.H. Rude, O. Zavorotynska, L.M. Arnbjerg, D.B. Ravnsbaek, R.A. Malmkjaer, H. Grove, B.C. Hauback, M. Baricco, Y. Filinchuk, F. Besenbacher and T.R. Jensen, *International Journal of Hydrogen Energy*, 2011, **36**, 15664-15672.

30. Y. Wang, W.D. Richards, S.P.Ong, L.J. Miara, J.C. Kim, Y. Mo and G. Ceder, *Nature Materials*, 2015, **14**, 1026-1031.

31. S.P. Ong, Y. Mo, W. Davidson Richards, L. Miara, H. Sug Lee and G.Ceder, *Energy & Environmental Science*, 2013, **6**, 148–156.

32. I. Cascallana-Matias, PhD thesis, University of Glasgow, 2016.

33. S. Orimo, Y. Nakamori and A. Züttel, *Materials Science and Engineering: B - Journal*, 2004, **108**, 51-53.

34. S. Gomes, H. Hagemann and K. Yvon, *Journal of Alloys and Compounds*, 2002, **346**, 206-210.

35. P.J Larkin, in *Infrared and Raman Spectroscopy: Principles and Spectral Interpretation*, Elsevier Inc., New York, 2nd edn., 2018, ch. 2, pp. 7-28.

36. A.R. West, in *Basic Solid State Chemistry*, John Wiley & Sons Ltd., 2nd edn., 1988.

37. Y. Koyama, Y. Yamada, I. Tanaka, S.R. Nishitani, H. Adachi, M. Murayama and R. Kanno, *Materials Transactions*, 2002, **43**, 1460-1463.

38. L. Mosegaard, B. Møller, J. Jørgensen, Y. Filinchuk, Y. Cerenius, J.C. Hanson, E. Dimasi, F. Besenbacher and T.R. Jensen, *Journal of Physical Chemistry C*, 2008, **112**, 1299–1303.

39. M. Matsuo, H. Takamura, H. Maekawa, H.-W. Li *and* S. Orimo, *Applied Physics Letters*, 2009, **94**, 084103.

40. H. Oguchi, M. Matsuo, J.S. Hummelshøj, T. Vegge, J.K. Nørskov, T. Sato, Y. Miura, H. Takamura, H. Maekawa *and* S. Orimo, *Applied Physics Letters*, 2009, **94**, 141912.

41. A. Borgschulte, R. Gremaud, S. Kato, N.P. Stadie, A. Remhof, A. Züttel, M. Matsuo *and* S.Orimo, *Applied Physics Letters*, 2010, **97**, 031916.

42. L.H. Rude, T.K. Nielsen, D.B. Ravnsbæk, U. Bösenberg, M.B. Ley, B. Richter, L.M. Arnbjerg, M. Dornheim, Y. Filinchuk, F. Besenbacher and T.R. Jensen, *Physica Status Solidi A*, 2011, **8**, 1754–1773.

43.

4. Conclusions

This project focused on stabilising the HP-phase of $LiBH_4$ at RT. Efforts focused on the investigation of the most simple and efficient way to synthesise, stabilise and characterise such Li-ion conducting materials, at room temperature. Specifically, the project focused on stabilising the cubic, HP-phase of $LiBH_4$ at RT, by mixing $LiBH_4$, $NaBH_4$ and LiI and on varying the Li^+/Na^+ and BH_4^-/I^- ratio at each respective crystallographic site.

Two synthesis approaches were applied. The first approach consisted of two steps and resulted in the synthesis of a cubic, "rock-salt" structure with the general formula $Li_{(1-y)}Na_y(BH_4)_{(1-z+yz)}X_{z(1-y)}$ by mixing $Li(BH_4)_{(1-z)}X_z$ (HT-$LiBH_4$) precursors with $NaBH_4$. That way $NaBH_4$ was used as a "host" for the lithium cations while, the halide to be substituted is already incorporated in the precursor. This approach recreated a "chemical pressure", whereby substitution of smaller ions mimics the action of high pressure by condensing a phase further[4]. The materials were studied with iodide used as the doping halide to stabilise and crystallise the ball milled samples. Thermal treatment was applied for each one of the samples. Different heating periods were applied, but no crystal structure differences were observed as a result. $Li_{0.5}Na_{0.5}(BH_4)_{0.81}I_{0.19}$ and $Li_{0.5}Na_{0.5}(BH_4)_{0.69}I_{0.31}$ were synthesised this way; both with the HP-$LiBH_4$ structure.

The second approach consisted of only one step; one ball milling process. In contrast to the first approach, all three initial compounds, $LiBH_4$, LiI, $NaBH_4$, were ball milled in one step, omitting the preliminary synthesis of the $LiBH_4$-LiI precursor, and reduced time and complexity. The one-step milling also minimises the exposure of the materials to air and moisture during multiple transfers between the glove box and the ball mill. As a result, a simpler, faster and more reliable process was successfully established. This process was successfully

---

[4] .I. Cascallana-Matias, PhD thesis, University of Glasgow, 2016

applied for the synthesis of the $Li_{0.58}Na_{0.42}(BH_4)_{0.88}I_{0.12}$ compound with the HP-$LiBH_4$ structure.

Different heating temperatures were investigated for the annealing of the ball milled samples, but the products were not significantly affected by annealing up to 400 ^0C. After heating for 2 h, at 400 ^0C, samples became a hard, solid mass, which rendered their removal from the silica tube impossible. Considering both the above observations and a tiny mass loss at 331.125 ^0C for the sample EA001-b and 237.948 ^0C for sample EA003-a, the second endothermic peak observed for both samples, could be assigned to a melting phenomenon of the final compound around or above 300 ^0C. Comparing the DTA data for the two samples, the two peaks each one presented are shifted towards lower temperatures in the case of the EA003-a sample. This result could probably be explained by different reaction kinetics (i.e. difference in particle size of the initial system's compounds, different surface areas) that govern the second synthesis process, due to the different starting chemical system ($Li(BH_4)_{(1-x)}X_x$: $NaBH_4$ for the first approach vs. $LiBH_4$ – LiI -$NaBH_4$ for the second approach). Finally, no evidence of any evolved gases was observed for either sample.

Following the development of the simplified synthesis process above, further investigation towards the explanation of the substitution mechanism and investigation of the samples' conducting properties and behaviour would be the next steps for a future project. Last but not least, in order to enhance the satisfactorily up to this point structural characterisation of the obtained samples, PND data would provide important information by shedding some more light on issues arose due to the dominant scattering of the, relatively, heavier sodium and iodide ions in the synthesised compounds.